



TESIS DOCTORAL

**UNIVERSALIDAD Y PROPIEDADES DE LA RUGOSIDAD
CINÉTICA EN FRENTE FUERA DEL EQUILIBRIO**

BEATRIZ GARCÍA BARREALES

**PROGRAMA DE DOCTORADO EN MODELIZACIÓN Y EX-
PERIMENTACIÓN EN CIENCIA Y TECNOLOGÍA**

2024



TESIS DOCTORAL

**UNIVERSALIDAD Y PROPIEDADES DE LA RUGOSIDAD
CINÉTICA EN FRENTE FUERA DEL EQUILIBRIO**

BEATRIZ GARCÍA BARREALES

**PROGRAMA DE DOCTORADO EN MODELIZACIÓN Y EX-
PERIMENTACIÓN EN CIENCIA Y TECNOLOGÍA**

Con la conformidad del director y los codirectores

Juan Jesús Ruiz
Lorenzo

Juan José Meléndez
Martínez

Rodolfo Cuerno
Rejado

Esta tesis cuenta con la autorización del director y codirectores de la misma y de la Comisión Académica del programa. Dichas autorizaciones constan en el Servicio de la Escuela Internacional de Doctorado de la Universidad de Extremadura.

2024

Resumen

Los fenómenos que ocurren fuera del equilibrio son altamente complejos y, en muchas ocasiones, resultan desafiantes de comprender, pero se manifiestan en numerosas áreas del conocimiento, abarcando disciplinas como la biología, la ingeniería y la economía. En el campo de la física, encontramos sistemas fuera del equilibrio en una amplia gama de contextos, que incluyen la dinámica de fluidos, la cinética química y los semiconductores, entre otros. La criticalidad está relacionada con leyes de escala y clases de universalidad, que se refieren a grupos de sistemas cuyas magnitudes escalan de manera similar, a pesar de que desde una perspectiva microscópica pueden ser muy diferentes. La rugosidad cinética de superficies es un ejemplo de sistemas críticos fuera de equilibrio. De manera simplificada, la rugosidad cinética ocurre en sistemas donde una superficie plana se torna cada vez más rugosa con el tiempo debido, por ejemplo, a la deposición aleatoria de partículas. Este fenómeno se manifiesta en diversos contextos, como el crecimiento de películas delgadas, la formación de copos de nieve o la corrosión de metales, y a su vez influye en una variedad de aplicaciones científicas y tecnológicas, como la proliferación celular o el desarrollo de nuevos materiales. En esta tesis, mediante exhaustivas simulaciones numéricas, investigamos las fluctuaciones críticas y caracterizamos las propiedades universales de diferentes frentes rugosos. Además, determinamos los exponentes críticos que gobiernan las fluctuaciones espaciotemporales del frente y analizamos sus propiedades estadísticas, como las funciones de correlación, con el objetivo de identificar comportamientos universales.

UNIVERSITY OF EXTREMADURA

DOCTORAL THESIS

**Universality and kinetic roughening
properties in non-equilibrium fronts**

Author:

Beatriz GARCÍA
BARREALES

Supervisors:

Juan Jesús RUIZ
LORENZO
Juan José MELÉNDEZ
MARTÍNEZ
Rodolfo CUERNO
REJADO

*A thesis submitted in fulfilment of the requirements
for the degree of Doctor of Philosophy*

in the

Department of Physics

2024

Abstract

Non-equilibrium phenomena are complex and often challenging to understand, but they are prevalent in many fields, including biology, engineering, and economics. In physics, non-equilibrium phenomena occur in fluid dynamics, chemical kinetics, and semiconductors, among others. Frequently, criticality is associated with the concepts of scaling and universality classes, which refer to groups of systems that exhibit similar scaling behavior. Surface kinetic roughening is an example of non-equilibrium criticality that is interesting because of its multidisciplinary nature. In a simplified manner, it occurs in systems where a flat surface becomes increasingly rough over time due to, for example, the random motion of particles onto the surface. This phenomenon can be observed in a variety of contexts, such as the growth of thin films, the formation of snowflakes, or in the corrosion of metals, all of which in turn influence a variety of scientific and technological applications such as cell proliferation or the development of new materials. In this thesis, we are interested in surface kinetic roughening from a theoretical point of view. We study the critical fluctuations and characterize the universal properties of different rough fronts through extensive numerical simulations. We determine the critical exponents that govern the spatio-temporal fluctuations of the front. Additionally, we analyze the statistical properties of the front fluctuations, such as their correlation functions, with the aim of identifying universal behaviors.

A mi familia

Agradecimientos

Quería comenzar este apartado tan personal de la tesis con un poema que me gusta desde mi adolescencia, pero que nunca se ha puesto tanto de manifiesto en mi vida como ahora.

*Cuando emprendas tu viaje a Ítaca
pide que el camino sea largo,
lleno de aventuras, lleno de experiencias.
No temas a los lestrigones ni a los cíclopes
ni al colérico Poseidón,
seres tales jamás hallarás en tu camino,
si tu pensar es elevado, si selecta
es la emoción que toca tu espíritu y tu cuerpo.
Ni a los lestrigones ni a los cíclopes
ni al salvaje Poseidón encontrarás,
si no los llevas dentro de tu alma,
si no los yergue tu alma ante ti.*

*Pide que el camino sea largo.
Que muchas sean las mañanas de verano
en que llegues -¡con qué placer y alegría!-
a puertos nunca vistos antes.
Detente en los emporios de Fenicia
y hazte con hermosas mercancías,
nácar y coral, ámbar y ébano
y toda suerte de perfumes sensuales,
cuantos más abundantes perfumes sensuales puedas.
Ve a muchas ciudades egipcias
a aprender, a aprender de sus sabios.*

*Ten siempre a Ítaca en tu mente.
Llegar allí es tu destino.
Mas no apresures nunca el viaje.
Mejor que dure muchos años
y atracar, viejo ya, en la isla,
enriquecido de cuanto ganaste en el camino
sin aguantar a que Ítaca te enriquezca.*

*Ítaca te brindó tan hermoso viaje.
Sin ella no habrías emprendido el camino.
Pero no tiene ya nada que darte.*

*Aunque la halles pobre, Ítaca no te ha engañado.
Así, sabio como te has vuelto, con tanta experiencia,
entenderás ya qué significan las Ítacas.*

Ítaca, Konstantino Kavafis

Puede sonar un poco soberbio compararme con Ulises, pero el doctorado ha sido todo un viaje, sobre todo desde el punto de vista personal. Han sido años de cambios, hacia una vida más adulta: mi primer trabajo, mi independencia; y en la sociedad: la pandemia, el auge de la extrema derecha, la guerra de Ucrania.

Como dice el poema, no me he encontrado a ningún Poseidón, nadie me ha tratado mal o menospreciado, nunca he recibido un grito o una regaña. Sin embargo, los mayores obstáculos me los he puesto yo misma, con una forma de ser un tanto insegura y ansiosa, que he podido ir amoldando al trabajo de la investigación poco a poco, y con ayuda de mi psicóloga, por supuesto.

He aprendido de los mayores sabios que conozco, mis antiguos profesores, que para mí son un referente tanto en lo personal como en lo profesional. Empiezo por Juanjo, el que inició todo esto cuando me pilló desprevenida acabando mi TFG allá por el verano de 2017. Me ha dado tantos consejos, y que poco caso le he hecho a la mayoría. Sigo sin saber hacer tortilla de patatas. Gracias por haberme hecho el doctorado más fácil. Continúo por Juan Jesús, el más sabio de los sabios, al que recurre todo el mundo porque sabe de todo la verdad. Largas han sido nuestras charlas, muchas de ellas

no de Ciencia. Qué felicidad vivir el premio Nobel contigo. Por último, mi tercer director de tesis, Rodolfo, al que he acudido normalmente un poco desesperada porque no hay experto mayor que él en frentes de crecimiento. Su manera de explicar, calmada y sosegada, siempre han dado consuelo a mis dudas. Ha sido una pena tenerlo tan lejos (y tan enfermo ocularmente hablando).

Estos han sido los sabios que han guiado mi camino, pero he conocido a muchos otros. Es más, he compartido café con ellos en el seminario de Física. He podido impartir clases con Andrés Santos y me encantaba ir a su despacho y escuchar sus batallitas. He podido debatir junto a Vicente, el más revolucionario del grupo. He compartido largas charlas con Enrique y he disfrutado de la voz grave de Santos. Son muchos los miembros del grupo SPhinX, pero a todos ellos gracias por haberme hecho sentir unA más.

Volviendo al poema, han sido muchos los puertos visitados: los congresos, las escuelas de verano, la estancia en Lisboa, los viajes que he hecho sola... Pero las hermosas mercancías con las que me voy cargada es la gente a la que he conocido en el camino.

Quiero empezar por Felipe, mi primer compañero de despacho en mi primer trabajo. Si hay alguien más distinto que yo, es él, sin embargo hacíamos buen tándem. Luego vino Rubén, y Alberto se empezaba a asomar. Son con los que más he compartido este camino, y ambos tienen un hueco para siempre en mi corazón. No puedo destacar más que cosas buenas de ambos, y espero que la investigación les acoja porque sería un derroche de talento que la academia los perdiera. ¡Pobre Alberto que hasta el último momento me ha estado ayudando con cosas matemáticas! Además de ellos, muchas más personitas han pasado por la planta de Física Teórica y ha sido un placer compartir estos años con todos ellos.

Paralelo a Física, entré en ADUEX, y formé parte de la Junta Directiva. Lo confieso, me gusta la representación y disfruto participando en los órganos como Junta de Facultad o el Claustro Universitario. De esta asociación surgió un grupo de amigos, que continuará para siempre. Y a pesar de que empezamos todos siendo predocs, ya rebosan los doctores. Con ellos hice un viaje inolvidable a Grecia, el país de Kavafis. Gracias por vuestra amistad Dani, María, Guada, Verónica, Alberto... y todo el grupo de telegram. Cabe destacar Javi Vaquero, que es uno de los que más me ha

aguantado. Él es una de esas personas que sólo sabe ayudar a los demás. Con él comencé mis comidas en la camilla del grupo Aire (qué tiempos). Luego evolucionamos y acabamos en económicas, casi todos los días comía allí por 5€ con Noelia (gracias a la cual las sobremesas se hacían más interesantes, cultas y francófonas) y con José Luis (un cachito de pan con el que he compartido mucho). Organizamos hasta un viaje a París, y que pedazo de viaje. La cafetería de económicas cerró, nadie sabe por qué, y tuve que acabar comiendo de tupperes sola en mi despacho.

Además de mi trabajo en Física Teórica, he tenido una especie de segundo trabajo parcial en Física del Aire, con Fis&Kids. Marisa y Maricruz, gracias por tratarme tan bien y por enseñarme otros aspectos que han contribuido igualmente en mi doctorado.

Solo me he encontrado con gente amable en este viaje, da igual al sitio que fuese, desde Lisboa a Santander, pasando por InvestigaEx o por el G9. Y esta universidad ha sido una segunda casa. Gracias a todos los que me habéis ayudado, los que habéis estado ahí siempre para escucharme, los que creáis en mí. Gracias a mi familia, que siempre está ahí, y a mis amigxs. Y gracias, en especial, a mi pareja Ignacio, que me ha dado la mano todo el viaje.

El camino ha sido largo, ¡pero la riqueza ha sido tanta! Llego a Ítaca cansada, y no miento si digo que la hallo pobre. No se si tendrá más cosas que darme o será el final, pero solo puedo decir que ha valido la pena.

Badajoz, 2023

Beatriz García Barreales

Contents

Nomenclature	xxi
Introduction	1
1 Surface kinetic roughening	5
1.1 Critical phenomena	6
1.2 Scaling properties	8
1.3 Deposition models and growth equations	10
1.3.1 Discrete deposition models	11
1.3.2 Continuum growth equations	14
1.3.3 KPZ universality class	17
1.4 Models with a depinning transition	22
1.4.1 Depinning transition	23
1.4.2 Quenched noise in stochastic growth equations	25
1.4.3 Some properties of the quenched KPZ equation	26
1.5 Rough interfaces in nature	27
2 Directed Percolation	33
2.1 Lattice model and scaling behavior	33
2.2 DP conjecture	37
2.3 Mean-field approximation	37
2.4 Phenomenological Langevin equation	39

2.5	Contact process	39
2.6	Directed Percolation Depinning	41
2.7	DP in nature	44
3	Methodology	49
3.1	Observables	49
3.2	Calculation of uncertainty	54
4	Reaction-diffusion fronts	57
4.1	Introduction	57
4.2	Model and simulation details	61
4.3	Results	64
4.3.1	Front velocity	64
4.3.2	Front roughness: exponent β	66
4.3.3	Front correlation length: exponents z and α	68
4.3.4	PDF of front fluctuations	68
4.3.5	Front covariance	72
4.4	Conclusions	73
5	Coffee-ring fronts	75
5.1	Introduction	76
5.2	Model and simulation details	79
5.3	Results	82
5.3.1	Aggregate morphology	82
5.3.2	Front velocity	84
5.3.3	Front roughness	87
5.3.4	Height-difference correlation function	89
5.3.5	Correlation length	92
5.3.6	Intrinsic anomalous scaling	95
5.3.7	Macroscopic shapes for $r_{AB} \neq 0$	99

5.3.8	Front structure for $r_{AB} = 0$	102
5.3.9	Free versus periodic boundary conditions	104
5.3.10	Off-lattice ballistic deposition	106
5.4	Conclusions	108
6	Contact process fronts	113
6.1	Introduction	114
6.2	Model and simulation details	115
6.3	Results	118
6.3.1	Density and roughness: exponents θ and β	118
6.3.2	Front correlation length: exponents α and z	123
6.3.3	Height-difference correlation function	126
6.3.4	Front structure factor	130
6.3.5	Mean squared height gradient	132
6.3.6	PDF of front fluctuations	135
6.3.7	Front covariance	140
6.4	Conclusions	143
7	Thesis summary and future work	147
	Appendices	151
A	Relation between α and z in the KPZ equation	151
B	The coefficient λ of the nonlinear term	151
C	From the microscopic $A + A \leftrightarrow A$ model to the FKPP eq. . .	152
	Bibliography	154

Nomenclature

BD	Ballistic Deposition, page 12 ¹
CP	Contact Process, page 39
DP	Directed Percolation, page 33
DPD	Directed Percolation Depinning, page 26
DSM	Dynamic Scattering Modes, page 19
EW	Edwards-Wilkinson, page 15
FBC	Free Boundary Conditions, page 82
FKPP	Fisher-Kolmogorov-Petrovsky-Piscunov, page 58
FV	Family-Vicsek, page 50
GOE	Gaussian Orthogonal Ensemble, page 18
GOE-TW	Distribution of the largest eigenvalue of the GOE, page 19
GSE	Gaussian Symplectic Ensemble, page 19
GSE-TW	Distribution of the largest eigenvalue of the GSE, page 19
GUE	Gaussian Unitary Ensemble, page 18
GUE-TW	Distribution of the largest eigenvalue of the GUE, page 19

¹The page number is that where the acronym is introduced for the first time.

HBC	Helical Boundary Conditions, page 61
JK	Jackknife, page 55
KPZ	Kardar-Parisi-Zhang, page 16
MF	Mean-Field, page 37
PBC	Periodic Boundary Conditions, page 61
PDF	Probability Density Function, page 18
QEW	Quenched Edwards-Wilkinson, page 25
QKPZ	Quenched Kardar-Parisi-Zhang, page 25
RD	Random Deposition, page 11
RDwR	Random Deposition with surface Relaxation, page 12
RG	Renormalization Group, page 7
sFKPP	Stochastic Fisher-Kolmogorov-Petrovsky-Piscunov, page 59
TW	Tracy-Widom, page 18

Introduction

Surface kinetic roughening is a phenomenon that occurs in out-of-equilibrium systems where a flat surface gradually becomes rougher over time due to, for example, the random deposition of particles. This process can be observed in various contexts, such as the growth of thin films, the formation of snowflakes, or the corrosion of metals. The study of kinetic roughness is of significant interest because it exemplifies non-equilibrium systems exhibiting critical phenomena. Criticality in this context refers to the emergence of scale-invariant behavior and universality classes, where different systems exhibit similar scaling behaviors despite their microscopic differences. Understanding kinetic roughness is not only essential for gaining insights into fundamental aspects of non-equilibrium physics but also has practical implications in various scientific and technological applications, ranging from cell proliferation to the development of novel materials.

In this thesis, we are interested in the study of the universality and kinetic roughening properties of non-equilibrium fronts, addressing them from a theoretical standpoint. We study the critical fluctuations and characterize the universal properties of different rough fronts through extensive numerical simulations. We determine the critical exponents that govern the spatio-temporal fluctuations of the front. Additionally, we analyze the statistical properties of the front fluctuations, such as their correlation functions, with the objective of identifying universal behaviors.

The thesis is divided into seven chapters. Chapters 1 and 2 establish the theoretical framework, and Chapter 3 sets out the methodology which will be considered in the remaining chapters. As the main novel contributions of the thesis, chapters 4, 5, and 6 collect the study of three different systems which have in common the emergence of a growth front. Through extended

computer simulations, we analyze the universal properties of these systems, to reach a better understanding of the related physical system or to extend the knowledge of a given universality class. Each of these chapters presents its own results and the corresponding conclusions. In the final chapter, we provide a summary of the thesis results, elucidate its contributions to the scientific field, and outline directions for future research.

We next explain briefly the content of each one of the thesis chapters:

- In Chapter 1 we introduce the fundamental concepts related to kinetic surface roughening. First, we focus on particle deposition models. We develop simple particle models (discrete viewpoint) and pose stochastic growth equations (continuum viewpoint) with time-dependent noise in order to characterize the different universality classes that will appear in this thesis. Then, we introduce models with a depinning transition and system where quenched disorder. Finally, we present experiments in which interfaces have been measured and characterized.
- In Chapter 2 we focus on the Directed Percolation universality class, and specifically in the Contact process model, that will appear in next chapters. We dedicate a section to the Directed Percolation Depinning model, which connects concepts from the first and second chapters. To conclude, we also discuss some experiments related to these universality classes.
- Chapter 3 sets out the methodology we will use to study our systems in the following chapters. Here we define the observables we measure and how estimate their statistical errors.
- In Chapter 4 we study front dynamics for a reaction-diffusion system, which in the continuum is described by the stochastic Fisher-Kolmogorov-Petrovsky-Piscunov equation.
- In Chapter 5 we study the kinetic behavior of the fronts of coffee-ring aggregates via simulations of an off-lattice model, so-called patchy colloids model, considered for this context.
- In Chapter 6 we study the interface representation of the contact process at its directed-percolation critical point, where the scaling prop-

erties of the interface can be related to those of the original particle model.

- Chapter 7 encapsulates a brief overview of all the work conducted throughout the thesis.

Published articles

1. B. G. Barreales, J. J. Meléndez, R. Cuerno, and J. J. Ruiz-Lorenzo, *J. Stat. Mech.*, 023203 (2020).
2. B. G. Barreales, J. J. Meléndez, R. Cuerno, and J. J. Ruiz-Lorenzo, *Phys. Rev. E* **106**, 044801 (2022).
3. B. G. Barreales, J. J. Meléndez, R. Cuerno, and J. J. Ruiz-Lorenzo, *Phys. Rev. E* **108**, 044801 (2023).

Financial support

The thesis was supported by Junta de Extremadura (Spain) through Grant No. IB16013 (partially funded by FEDER) and by Junta de Extremadura and Fondo Social Europeo (FSE, EU) through pre-doctoral Grant No. PD18034.

Chapter 1

Surface kinetic roughening

Non-equilibrium phenomena are complex and often challenging to understand, but they are prevalent in various fields, including Biology [1], Engineering [2], or Economy [3]. In Physics, non-equilibrium phenomena appear, for instance, in fluid flow in porous media [4], the growth of thin films [5], active matter [6, 7] or quantum matter [8, 9], among others. In these and many other contexts, the emergence of strong correlations associated with space-time criticality become particularly relevant [10]. Frequently, criticality is associated with the concepts of scaling and universality classes, which refer to a group of systems that exhibit a similar scaling behavior.

Surface kinetic roughening is an example of non-equilibrium criticality which is interesting because of its multidisciplinary nature. In a simplified manner, surface kinetic roughening occurs in systems where a flat surface becomes increasingly rough over time due to the random motion of particles onto the surface. This phenomenon can be observed in a variety of contexts, such as the growth of thin films, the formation of snowflakes, or in the corrosion of metals, which in turn influence a variety of scientific and technological applications such as proliferation of cells or development of new materials [11].

From the theoretical point of view, we are herein interested in surface kinetic roughening through the study of critical fluctuations of the interface of a driven system subjected to some kind of noise. The ensuing universality classes and their properties are being quite recently seen to generalize and expand [12, 13] those of equilibrium critical dynamics to non-equilibrium

conditions [10], becoming relevant even for non-interfacial systems.

1.1 Critical phenomena

In Physics, criticality refers to the behavior of a system near a critical point, where it undergoes significant changes in its properties, with prevalence of scale invariance. Systems exhibiting criticality are called critical systems. The changes in their macroscopic behavior can manifest as phase transitions, which involve substantial changes in the properties of a system as its internal structure (or order) changes. Phase transitions can be either discontinuous or continuous.

Discontinuous phase transitions, also called first-order phase transitions, are characterized by a sudden jump or discontinuity in the system properties. Examples include the solid-liquid phase transition or the liquid-gas phase transition [14].

On the other hand, continuous phase transitions, also known as second-order phase transitions, occur without any sudden change. Instead, they are marked by gradual continuous changes. A key feature of continuous phase transitions is the emergence of long-range correlations, where fluctuations in one part of the system can affect the behavior of distant parts. Such type of behaviors are termed critical phenomena and are often associated with the concept of universality. Well-known examples of a continuous phase transitions are the para-ferromagnetic transition at the Curie temperature and the liquid-gas transition at the triple point [14].

The study of continuous phase transitions has been particularly fruitful in the field of magnetism, with the model of ferromagnetic materials providing a valuable framework. Ferromagnets are systems that exhibit spontaneous magnetization even in the absence of an external magnetic field. At the critical temperature (Curie temperature), a ferromagnetic material undergoes a continuous phase transition from a ferromagnetic phase to a paramagnetic phase. This transition is associated with the loss of spontaneous magnetization and the emergence of critical fluctuations. The behavior of the system near the critical temperature is described by a set of critical exponents, which govern the scaling properties of various physical quantities, such as the magnetization or the specific heat.

Critical exponents occur in all continuous phase transitions, actually. They provide valuable insights into the universal behavior of those systems undergoing continuous phase transitions. For instance, the Ising model, a simple theoretical model of ferromagnetism, predicts specific values for the critical exponents of the para-ferromagnetic transition. Experimental observations of various physical systems have confirmed the universality of these critical exponents, highlighting the remarkable similarities in the behavior of diverse systems near their respective critical points. For example, a simple fluid and a uniaxial ferromagnet have exactly the same critical exponents. The existence of universal scaling exponents and their calculation for various systems is a central problem of statistical mechanics. Nonetheless, the renormalization group (RG) method, introduced by Wilson in 1971, permits a systematic calculation of the scaling exponents [15]. The concept of universality class expresses the idea that only a few fundamental variables determine the exponents that describe scaling behavior. Consequently, diverse systems that may seem unrelated at first glance, exhibit strikingly comparable behavior [16].

Regardless of their character (continuous or discontinuous), equilibrium phase transitions take place if both phases are in mechanical, thermal, and chemical equilibrium. This is the case of the aforementioned para-ferromagnetic transition. Nevertheless, it has been acknowledged that the occurrence of phase transitions (or more precisely phenomena resembling them) which entail changes from disordered states to ordered states are not exclusively restricted to physical systems in thermal equilibrium [17]. There are many examples in nature of the emergence of criticality in slowly driven non-equilibrium systems such as earthquakes in seismic systems, avalanches in granular media, and rainfall in the atmosphere [18]. In the context of this thesis, it must be remarked that some non-equilibrium systems exhibit the so-called self-organized criticality (SOC). Their macroscopic behavior displays the spatial or temporal scale-invariance characteristic of the critical point of a continuous phase transition, but without the need to tune control parameters to a precise value, because the system, effectively, tunes itself as it evolves towards criticality [11].

In roughening processes, simple scaling relations connect apparently independent quantities and exponents, allowing one to study and characterize these systems in universality classes analogous to those of equilibrium crit-

ical phenomena. Theoretical models are the basis for the study of those growth processes. Furthermore, simulation studies provide an important link between theory and experiment, allowing one to distinguish the essential factors that determine morphology from the unimportant details. From these models one obtains large-scale properties that are universal, i.e. independent of the specific microscopic details of the model under consideration [11]. Incidentally, it is worthy mentioning that the interfaces produced by growth processes are self-affine, which means that rescaling anisotropically a part of the interface yields an interface that is statistically indistinguishable from the whole [11]. We will be on these ideas below. Actually, they are the conceptual leitmotivs inspiring this thesis.

1.2 Scaling properties

In this section we enumerate a small number of scaling behaviors that allows one to characterize kinetic roughening surfaces. We will discuss this topic more specifically in Chapter 3.

The key concept is that of front, which will be called surface or interface indistinctly hereafter. In all cases, the front is defined as a set of local space-time variables $h(\mathbf{x}, t)$. In the simplest case, we define the front as the ensemble of particles in an aggregate that are highest in each substrate position, resulting in a set of height variables $h(\mathbf{x}, t)$ where \mathbf{x} are the positions of the substrate. As an example, Fig. 1.1 shows a particle aggregate in a one-dimensional substrate of size L . The heights $h(x, t)$, where $x = 1, \dots, L$, are denoted as blue points. The mean front, $\bar{h}(t)$, defined as the average of the local heights $h(\mathbf{x}, t)$, measures the mean position of the front.

Apart from its position, one more variable describing a front is its width $w(L, t)$, which characterizes the roughness of the interface, defined as the standard deviation of the height $h(\mathbf{x}, t)$. In Fig. 1.1 the mean height or mean front, $\bar{h}(t)$, has been plotted as a solid orange line and the width of the front is indicated by a magenta arrow.

The typical time evolution of $w(L, t)$ has two behavioral regions separated by a crossover time t_x , namely,

$$w(L, t) \sim \begin{cases} t^\beta, & \text{if } t \ll t_x, \\ L^\alpha \equiv w_{\text{sat}}(L), & \text{if } t \gg t_x. \end{cases} \quad (1.1)$$

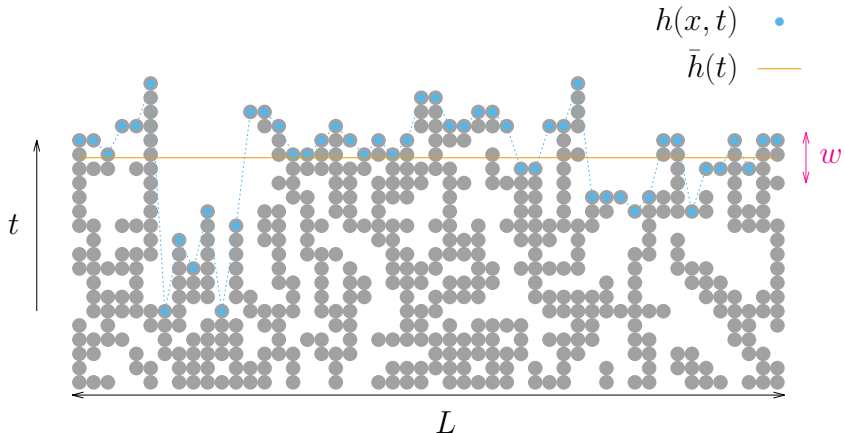


Figure 1.1: Example of a particle aggregate of lateral size L . The local heights $h(x, t)$ (blue dots) define the front. The system evolves over time, as more particles are aggregated and the heights grow in the vertical direction. The mean front $\bar{h}(t)$ and the width $w(L, t)$ are represented by a solid orange line and a magenta arrow, respectively.

Initially, the width increases as a power of time; the exponent β , called the *growth exponent*, characterizes the time-dependent dynamics of the roughening process. The power-law regime does not extend indefinitely in time, but it is followed by a saturation regime at which the front width reaches a saturation value, w_{sat} . As L increases, the saturation value, $w_{\text{sat}}(L)$, increases as well, through another power law. The exponent α , called the *roughness exponent*, is a second critical exponent which characterizes the roughness of the saturated interface. The crossover time t_x depends of the system size as

$$t_x \sim L^z, \quad (1.2)$$

where z is called the *dynamic exponent*.

The scaling exponents α , β , and z are not independent. Indeed, if one approaches the crossover point from the left and from the right, one has $w(t_x) \sim t_x^\beta$ and $w(t_x) \sim L^\alpha$, respectively. These two relations, along with $t_x \sim L^z$, imply that

$$z = \alpha/\beta, \quad (1.3)$$

which is valid for any growth process obeying the scaling relation (1.1).

One more important feature of most surfaces is the existence of space

correlations. In growth processes, correlations develop along the surface, which implies that heights at different sites of the surface are not completely independent of one another. In other words, local heights depend on average upon the heights of neighboring sites. Although the growth process is local, the information about the height of each neighbor spreads globally through this lateral process. The characteristic distance over which the heights are correlated (i.e. over which the heights “know” about each other) is called the parallel correlation length, ξ_{\parallel} .

At the beginning of the growth process, $t = 0$, usually all sites are uncorrelated. At $t > 0$, the parallel correlation length increases with time during the growth process. However, this correlation length cannot keep growing indefinitely in a finite system since it is constrained by the system size, L . When ξ_{\parallel} reaches the size of the system, the entire interface becomes correlated, resulting in the saturation of the interface width. Thus, $\xi_{\parallel} \sim L$ at saturation, which occurs at a time t_x given by (1.2). Replacing L by ξ_{\parallel} , we get $\xi_{\parallel} \sim t_x^{1/z}$, which holds for $t < t_x$ as well. According to this,

$$\xi_{\parallel} \sim \begin{cases} t^{1/z}, & \text{if } t \ll t_x, \\ L, & \text{if } t \gg t_x. \end{cases} \quad (1.4)$$

From this point of view, the dynamic exponent z quantifies the power-law increase of the parallel correlation length along the surface.

In the growth direction, the fluctuations are characterized by another correlation length, the perpendicular correlation length, ξ_{\perp} . It has the same scaling behavior as the width $w(L, t)$.

Before proceeding further, we should clarify a potential ambiguity in the dimension notation. The dimension of an interface will be denoted by d . Therefore, $d = 1$ denotes a one-dimensional interface embedded in a two-dimensional plane, while $d = 2$ represents a two-dimensional interface embedded in a three-dimensional space. Moreover, interfaces of higher dimensions are also interesting to consider.

1.3 Deposition models and growth equations

In this section we discuss discrete models in which particles are deposited onto a substrate. A growing front is consequently created, which can be

characterized using the scaling equations mentioned in the previous section and computing the critical exponents β , α , and z . For each model, we will derive the related continuous growth equations. We will be able then to introduce the main universality classes of surface kinetic roughening.

1.3.1 Discrete deposition models

Random deposition, random deposition with relaxation, and ballistic deposition are likely the simplest discrete models involving particle deposition which generate non-equilibrium interfaces.

In particular, *random deposition* (RD) may be considered as the most basic surface growth model. In this model, particles fall down along a vertical direction at a random position towards the substrate. Upon falling, they attach themselves to either the substrate or to previous particles existing in that position (see the schema in Fig. 1.2). The surface height increases as particles accumulate on top of each other in individual columns, without any correlation between them; Fig. 1.3a illustrates the corresponding surface morphology. Each column has an equal probability of growing, which is given by $p = 1/L$, where L is the size of the system.

The simplicity of the model allows one to calculate exactly the critical exponents. The probability that a column has height h after the deposition of N particles follows a binomial distribution,

$$P(h, N) = \binom{N}{h} p^h (1-p)^{N-h}. \quad (1.5)$$

One may compute then the average of the height and the second moment of the height. The width of the interface is straightforwardly calculated to give

$$w^2(t) = \langle h^2 \rangle - \langle h \rangle^2 = \frac{N}{L} \left(1 - \frac{1}{L} \right). \quad (1.6)$$

The evolution time may be defined for this model as the mean number of deposited layers, $t = N/L$. From Eq. (1.6) and Eq. (1.1), we have $w(t) \sim t^{1/2}$, and therefore

$$\beta = \frac{1}{2}. \quad (1.7)$$

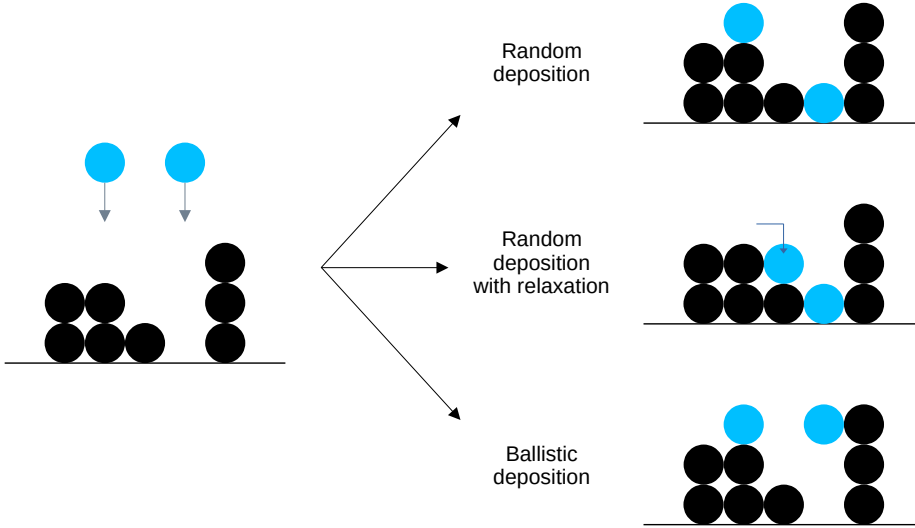


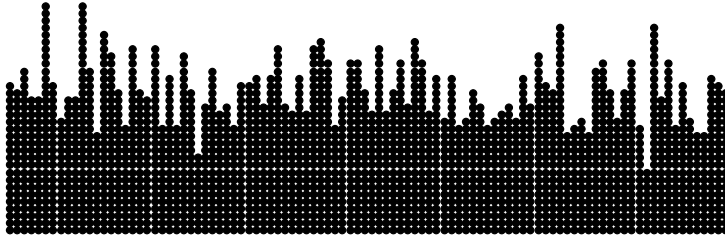
Figure 1.2: Diagrams of particle adhesion rules in deposition models: random deposition, random deposition with relaxation, and ballistic deposition.

Note that, in the RD model, the interface width grows indefinitely, without saturation. Since there are no space or lateral correlations, the correlation length ξ_{\parallel} is always zero, the interface does not saturate, and the roughness exponent α is not well defined.

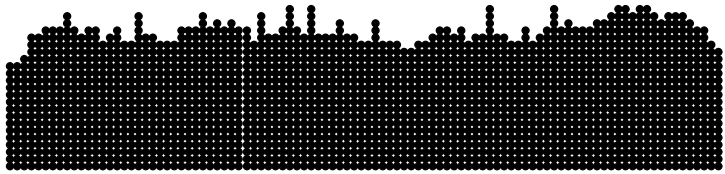
Another discrete model, very simple but nonetheless interesting, is *random deposition with surface relaxation* (RDwR). To include surface relaxation in the RD model, one allows each deposited particle to diffuse along the surface up to a finite distance (typically up to the nearest neighbor sites), stopping when it finds a position with a lower height. A schema of how particles are deposited in this model is depicted in Fig. 1.2. An example of this interface, on the other hand, is shown in Fig. 1.3b. One straightforwardly realizes that it is much smoother compared to the RD model without relaxation.

Observe that, in the RDwR model, the heights of nearby columns influence particle positioning, hence correlations appear. As we shall see below, analytical solutions in one dimension provide $\beta = 1/4$ and $\alpha = 1/2$.

Ballistic deposition (BD) is still another simple discrete model which generates a non-equilibrium interface with interesting growth properties.



(a) Random deposition morphology.



(b) Random deposition with surface relaxation morphology.



(c) Ballistic Deposition morphology.

Figure 1.3: Particle aggregates for RD, RDwR, and BD models. As a reference, the substrate size is always $L = 100$ in all cases, and the total number of particles in each morphology is 2000.

One may also consider it as a modification of RD. Again, particles fall vertically at a random position of the substrate, where they may attach themselves to the substrate or to another particle previously deposited in the same position. As a new feature they may now aggregate laterally to particles that are in neighboring sites. Assuming an one-dimensional model with nearest-neighbor sticking rule, for simplicity, the new particle will stick to the first site along its trajectory that has an occupied nearest neighbor, see Fig. 1.2.

The morphology of a BD system is shown in Fig. 1.3c. Qualitatively, the aggregate is quite different to those previously listed. In particular, in this case, the density of particles is lower. Quantitatively, the critical exponents in one dimension computed by early numerical simulations are $\alpha = 0.47(2)$ and $\beta = 0.330(6)$ [19, 20].

As it is clear from the above discussion, these three models, which are easy to simulate and with small differences between them, generate quite different interfaces (see Fig. 1.3). This leads one to realize that small variations in the microscopic rules can yield noticeable differences in the kinetic surface roughening behavior. We will see this in the following section, as these three models belong to three different universality classes.

1.3.2 Continuum growth equations

In general, it is possible to associate stochastic growth equations with microscopic growth processes. This is of interest for the analytical study of such growth models.

We will derive first a differential equation to describe the simplest model, RD. Let $h(\mathbf{x}, t)$ be the interface height, where \mathbf{x} denotes a position within a d -dimensional substrate. The growth process may then be described by

$$\frac{\partial h(\mathbf{x}, t)}{\partial t} = F + \eta(\mathbf{x}, t), \quad (1.8)$$

with F being the average number of particles per unit time arriving at site \mathbf{x} , and $\eta(\mathbf{x}, t)$ being an uncorrelated space-time noise with mean and variance

$$\begin{aligned} \langle \eta(\mathbf{x}, t) \rangle &= 0, \\ \langle \eta(\mathbf{x}, t) \eta(\mathbf{x}', t') \rangle &= 2D \delta^d(\mathbf{x} - \mathbf{x}') \delta(t - t'), \end{aligned} \quad (1.9)$$

where D is a parameter which controls the noise amplitude. This noise reflects the random fluctuations in the deposition process or, more generally, the random time-dependent fluctuations at the interface.

The statistical properties described by Eq. (1.8) are those of an interface growing through RD. This model can be solved exactly, both in its discrete form or through its continuum equation, obtaining the same exponent $\beta = 1/2$. This leads one to define the so-called RD universality class, whose exponents are listed in Table 1.1.

The second discrete model we have seen above is RDwR. It is easy to derive the continuum growth equation which describes this model. Starting from Eq. (1.8), and using symmetry principles, one may demonstrate that an additional contribution of the form $\nu\nabla^2h$ (in the simplest case) must be added to account for surface relaxation [11]. One obtains then the *Edwards-Wilkinson* (EW) equation:

$$\frac{\partial h(\mathbf{x}, t)}{\partial t} = v_0 + \nu\nabla^2h + \eta(\mathbf{x}, t), \quad (1.10)$$

where ν is called surface tension, since the Laplacian $\nu\nabla^2h$ tends to smooth the interface. The term v_0 is the average growth velocity of the interface. It is usually not shown, since it may be absorbed by the Galilean transformation $h \rightarrow h + v_0t$.

The EW equation can be solved exactly, yielding the following critical exponents for dimension d [11]:

$$\alpha = \frac{2-d}{2}, \quad \beta = \frac{2-d}{4}, \quad z = 2. \quad (1.11)$$

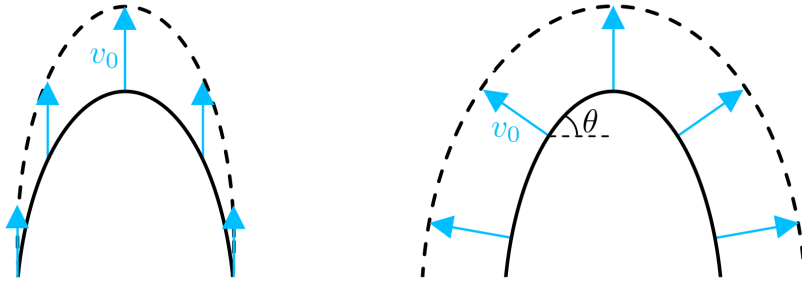
Thus, the discrete RDwR model and the continuous EW equation define a universality class, different from RD, usually called Edwards-Wilkinson universality class. The critical exponents of this universality class are collected in Table 1.1 as well.

The EW equation is the simplest linear equation to study the growth of interfaces by particle deposition. A modification of the EW equation which incorporates nonlinear terms was first proposed by Kardar, Parisi, and Zhang [21]. In Fig. 1.4a, an EW interface is shown. Note that this equation allows only growth along the perpendicular direction of the substrate, h -direction. It is reasonable to expect that the interface may also grow along the local normal direction, as shown in Fig. 1.4b. As a first approximation, one assumes then that the interface evolves locally according to the EW equation (coordinates $\delta x_{\text{loc}}, \delta h_{\text{loc}}$) but generating an increase δh along the vertical axis (see Fig. 1.4c) [13]. Using simple trigonometric rules, one obtains

$$\delta h = \delta h_{\text{loc}} \sqrt{1 + \tan^2 \theta} = v_0 \delta t \sqrt{1 + (\nabla h)^2}. \quad (1.12)$$

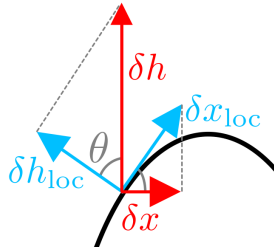
Assuming $|\nabla h| \ll 1$, one may expand the time derivative of the front as

$$\frac{\partial h(\mathbf{x}, t)}{\partial t} = v_0 + \frac{v_0}{2} (\nabla h)^2 + \dots \quad (1.13)$$



(a) Sketch of an interface that grows according to the EW equation. The interface always grows along the vertical axis with velocity v_0 .

(b) Sketch of an interface that grows along the local normal direction. The interface grows isotropically, so that each local piece of the interface advances in the direction normal to the interface.



(c) The local coordinates (growth normal to the interface) are related to the growth along the vertical direction.

Figure 1.4: Interfaces growing along a preferred axis (a) or growing locally in the normal direction (b). Panel (c) shows how to define the local coordinates for the interface (b).

Inserting the right-hand side contribution into the EW equation, and keeping only the lowest-order nonlinear term, one obtains the so-called *Kardar-Parisi-Zhang* (KPZ) equation:

$$\frac{\partial h(\mathbf{x}, t)}{\partial t} = v_0 + \nu \nabla^2 h + \frac{\lambda}{2} (\nabla h)^2 + \eta(\mathbf{x}, t). \quad (1.14)$$

In Eq. (1.14), ν and λ are constants and η is a noise term obeying Eq. (1.9), as in the previous equations. The velocity term v_0 is usually omitted, as for EW equation.

Since $(\nabla h)^2$ is positive, the introduction of the new term results in interface rising by adding material to it if $\lambda > 0$; if $\lambda < 0$, then material is

locally removed from the interface instead. This contrasts with the effect of the linear term, which tries to maintain the total mass unchanged by reorganizing the interface height.

The KPZ equation has been solved exactly in one dimension, obtaining the critical exponents $\beta = 1/3$, $\alpha = 1/2$ and $z = 3/2$ [12, 13, 22]; scaling is the same regardless of the sign of λ . The exponents computed numerically for the BD model are thus in good agreement with those of KPZ equation. Actually, from physical and symmetry principles, it is possible to demonstrate that the stochastic growth equation that describes BD is the KPZ equation, see Eq. (1.14) [11]. Consequently, the BD model and the KPZ equation belong to the same universality class.

1.3.3 KPZ universality class

The KPZ universality class is of paramount importance in the field of statistical physics, and in particular in surface growth processes, due to the frequency with which its universal behavior emerges in a wide variety of different systems [13, 22].

The KPZ exponents, either analytical (for $d = 1$) or estimated numerically (for $d > 1$), fulfill the scaling relation

$$\alpha + z = 2, \tag{1.15}$$

which is valid in any dimension. It has been deduced by RG methods, but it can also be derived using scaling arguments (see Appendix A).

The determination of the exact exponents in any substrate dimension d is one of the most important open issues in statistical physics. In spite of the lack of analytical solutions, the critical exponents for $d > 1$ have been numerically computed; particularly, the KPZ exponents for $d = 1, 2, 3$ are collected in Table 1.1. Through recent extensive simulations of discrete growth models and real-space RG calculations, Oliveira computes in Ref. [23] the exponent β up to $d = 15$ and conjectures the following equation for this exponent:

$$\beta_{\text{KPZ},d} = \frac{7}{8d + 13}. \tag{1.16}$$

Knowing β one can derive from Eqs. (1.3) and (1.15) the remaining exponents for this universality class. The critical exponents computed for $d = 2$

and $d = 3$ are collected in Table 1.1, as well.

Table 1.1: Critical exponents for the three universality classes discussed in Sec. 1.3. Asterisks indicate that the value of the corresponding exponent is derived from other exponents.

RD	$\beta = 1/2$	α not defined	
EW	$\beta = \frac{2-d}{4}$	$\alpha = \frac{2-d}{2}$	$z = 2$
KPZ ($d = 1$)	$\beta = 1/3$	$\alpha = 1/2$	$z = 3/2$
KPZ ($d = 2$)	$\beta = 0.242(2)$ [23]	$\alpha = 0.390(3)*$	$z = 1.610(3)*$
KPZ ($d = 3$)	$\beta = 0.186(4)$ [23]	$\alpha = 0.314(3)*$	$z = 1.686(4)*$

Universality classes are not only determined by the values of the critical exponents, but also by some other universal properties which likewise aid to categorize systems into universality classes. For instance, the one-point statistics of the field fluctuations is known to be another universal trait of the KPZ universality class. The probability density function (PDF) of the front fluctuations [rescaled by the roughness, see Eq. (3.7)] for one-dimensional KPZ class is provided by the Tracy–Widom (TW) distribution [12, 22]. The TW distribution arises in the context of random matrix theory [24], which deals with fluctuation properties of eigenvalues of matrices whose entries are random numbers. Among them, matrices of Gaussian random numbers constitute the most fundamental ensembles of random matrices. The Gaussian ensembles are families of normally distributed random matrices with distributions invariant under different unitary transformations. They have been well studied, partly because of their analytical properties, but also because of the associated spectra, that closely approximate those of many systems with large degrees of freedom. We can distinguish three ensembles: Gaussian Unitary Ensemble (GUE) formed by real symmetric matrices; Gaussian Orthogonal Ensemble (GOE) of complex Hermitian matrices; and Gaussian

Symplectic Ensemble (GSE) containing quaternion, self-dual Hermitian matrices. The distributions of the largest eigenvalue of these ensembles were explicitly obtained by Tracy and Widom [25, 26], and they were denoted as $\chi_{\text{TW},\tilde{\beta}}$, corresponding to the three Gaussian ensembles: GOE ($\tilde{\beta} = 1$), GUE ($\tilde{\beta} = 2$) and GSE ($\tilde{\beta} = 4$). Hereinafter, we will refer to these distributions as GOE-TW, GUE-TW, GSE-TW. This distinction is relevant, since the one-point distribution of the height fluctuations for one-dimensional KPZ universality class changes according to the global geometry of the interfaces, i.e., whether the interface is flat or circular, or equivalently, depending on the initial condition for infinite systems [13]. When the interface is flat, the PDF of rescaled front fluctuations should be provided by the GOE-TW. By contrast, circular interfaces are described by the GUE-TW.

Experiments with turbulent liquid-crystals have shown this geometry-dependency [27]. These experiments study the convection of nematic liquid crystals driven by an electric field applied between two parallel plates. Depending on the applied voltage, regimes of turbulence appear, called dynamic scattering modes (DSM). There are two regimes: DSM2, composed of topological defect lines, and DSM1 which is metastable. DSM2 nucleates randomly and takes over the metastable DSM1 state through a random growth process. Figure 1.5a shows two interfaces, one circular and one flat, and one can distinguish the two regimes, the darker one being the one that is spreading. Figure 1.5b shows the probability distribution of the rescaled local height for the circular and the flat interfaces, which are the GUE and GOE-TW distributions, respectively (there is a small horizontal translation that shrinks as time elapses).

One of the other most studied quantities is the spatial covariance function, which we call the height covariance $C_1(r, t)$; we will define this function in Sec. 3.1. Theoretical studies have shown that, in the asymptotic limit ($t \gg 1$), the covariance of the interface fluctuations for the one-dimensional KPZ class is given exactly by the time correlation of the stochastic process called Airy_1 for flat interfaces [28, 29] and Airy_2 for the curved ones [30, 31]. The correlation functions for the Airy processes have been estimated numerically by Bornemann *et al.* [32, 33]. Figure 1.5c plots the correlation functions of the Airy processes along with the experimental liquid-crystal turbulence data obtained for circular and flat interfaces in Ref. [27]. Interestingly, the 1D EW universality class shares this same feature [34]. Similarly,

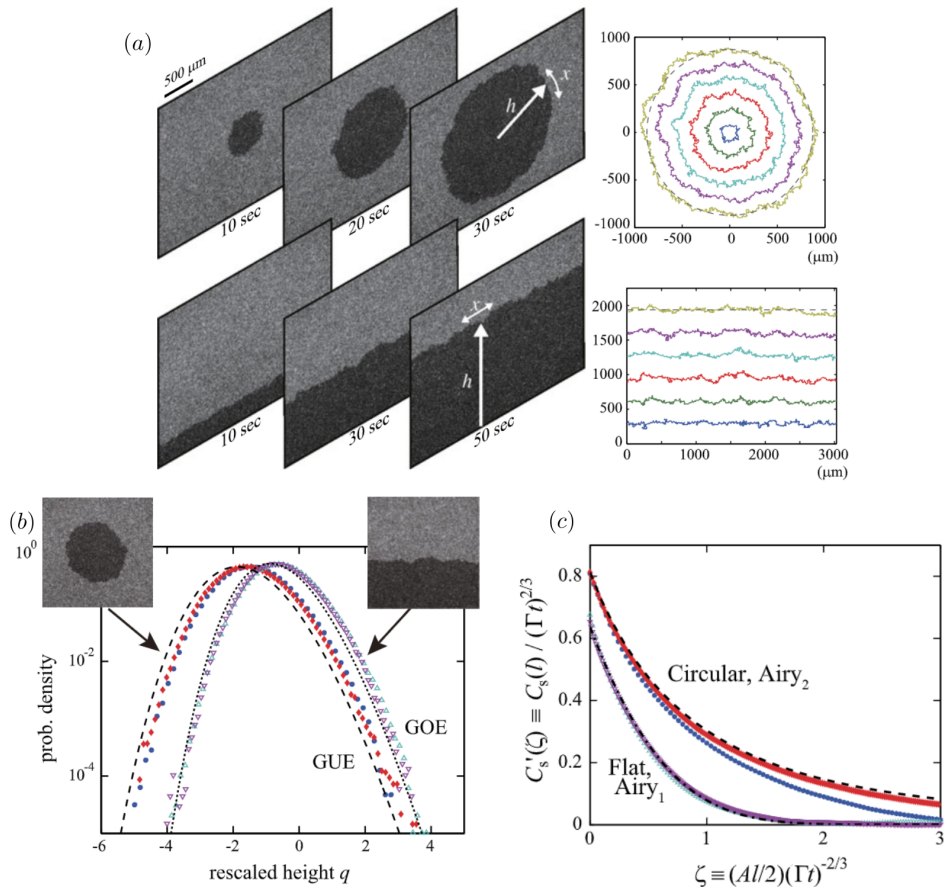


Figure 1.5: Kardar-Parisi-Zhang interfaces in liquid-crystal turbulence. (a) Growing DSM2 cluster with a circular (top) and flat (bottom) interface. (b) The blue and red solid symbols show the histograms for the circular interfaces at $t = 10$ s and 30 s; the light blue and purple open symbols are for the flat interfaces at $t = 20$ s and 60 s, respectively. The dashed and dotted curves show the GUE and GOE-TW distributions, respectively. (c) Rescaled correlation function. The symbols indicate the experimental data for the circular and flat interfaces, as explained in (b). The dashed and dashed-dotted lines indicate the correlation function for the Airy₂ and Airy₁ processes, respectively. See, for more details, Ref. [27].

the covariance of the 1D EW and KPZ equations with columnar noise has been recently discovered to be identical, and provided in those cases by that of the Larkin model of elastic interfaces in disordered media [35].

Universality for the two-dimensional KPZ universality class and its asso-

ciated limit distributions (i.e., higher-dimensional analogs of GOE-TW and GUE-TW) along with universal spatial correlation (analogous to covariance of the Airy processes) have been well characterized too [36–38]. For $d = 3$ the KPZ radial class is studied in detail in [39].

1.3.3.1 Relation with other equations

The KPZ equation, as we have seen in Eq. (1.14), describes the temporal change of a height field $h(\mathbf{x}, t)$ which one interprets as a growing interface. However, by performing simple transformations one can go from this equation to another that describe very different physical systems. Some examples follow:

1. *Stochastic Burgers' equation for incompressible fluid flow.*

From Eq. (1.14), let us define $\mathbf{v} = -\nabla h$ such that $\nabla \times \mathbf{v} = \mathbf{0}$. Then, one gets:

$$\frac{\partial \mathbf{v}}{\partial t} + \lambda \mathbf{v} \cdot \nabla \mathbf{v} = \nu \nabla^2 \mathbf{v} - \nabla \eta(\mathbf{x}, t), \quad (1.17)$$

which is the (stochastic) Burgers' equation, a fundamental partial differential equation that arises in fluid dynamics [40]. It describes the behavior of a viscous fluid and it is often used to model phenomena such as shock waves, turbulence, and wave propagation in fluids. In this equation, $\mathbf{v}(\mathbf{x}, t)$ represents the velocity field of the fluid as a function of position \mathbf{x} and time t , and ν is the kinematic viscosity of the fluid. The first and second terms on the left-hand side represent advection, which describes the transport of fluid velocity. The second term implements non-linearity in the equation. The first term on the right-hand side represents the diffusive term, accounting for the effects of viscosity, while the noise term represents stochastic forcing. In the limit $\nu \rightarrow 0$, this equation describes shock waves.

2. *Diffusion with random sources and sinks.*

From Eq. (1.14) and using the Cole-Hopf transformation $W(\mathbf{x}, t) = \exp\left[\frac{\lambda}{2\nu} h(\mathbf{x}, t)\right]$, we obtain a linear equation in W :

$$\frac{\partial W}{\partial t} = \nu \nabla^2 W + \left(\frac{\lambda}{2\nu} \eta(\mathbf{x}, t)\right) W. \quad (1.18)$$

For $\lambda = 0$, one has a diffusion equation. Thus, one can understand the additional term with parameter λ as a creation or destruction term, depending on the sign of η . Moreover, Eq. (1.18) can alternatively be interpreted as a Schrödinger equation in imaginary time with potential $\frac{\lambda}{2\nu}\eta(\mathbf{x}, t)$, which allows one to write its path integral version, as follows

$$W(\mathbf{x}, t) = \int_{(0,0)}^{(\mathbf{x},t)} \mathcal{D}\mathbf{x}(\tau) \exp\left(-\frac{1}{2\nu} \int_0^t d\tau \left[\frac{1}{2} \left(\frac{d\mathbf{x}}{d\tau} \right)^2 - \lambda\eta(\mathbf{x}(\tau), \tau) \right]\right). \quad (1.19)$$

3. Sums over paths in random media.

Equation (1.19) can be also thought of as describing polymers or direct paths evolve in the presence of a random potential $\eta(\mathbf{x}, \tau)$, which is the noise of the original differential KPZ equation. The first term in the exponential of Eq. (1.19) is the bending energy, which ensures that the polymer with minimum energy would be the straight one. In addition, the temperature fluctuations are parameterized by 2ν , while $\mathbf{x}(\tau)$ parameterizes the path or polymer.

1.4 Models with a depinning transition

Previous sections focused on interfaces that grow and become rough due to random time-dependent fluctuations, which stem from the random nature of the deposition process. However, there is a class of interface phenomena where there is no deposition, but an interface moves through an disordered medium instead (it is also possible for both to occur simultaneously, although this is not of interest to us in this section). As an example, let us imagine an experiment involving a fluid interface that permeates a paper towel. The inhomogeneities of the medium affect the interface velocity, as different points in the medium resist the flow differently. This randomness can be interpreted as a type of noise that remains constant over time, called quenched noise. In our example, fluid pressure and capillarity propel the fluid, but the inherent medium disorder slows it down. If the disorder prevails, the interface becomes pinned. On the contrary, if the driving forces overcome the disorder, the interface remains in motion. By changing the

driving force, the transition from a pinned to a moving interface may be achieved; this phenomenon is called depinning (or pinning-depinning) transition, and will be described below.

1.4.1 Depinning transition

Let F be a driving force acting on an interface in a porous medium, as schematized in Fig. 1.6. The disorder acts as an inhomogeneous friction force, pinning parts of the interface. Other parts are free to advance, and they try to drive the neighboring parts of the interface into motion as well.

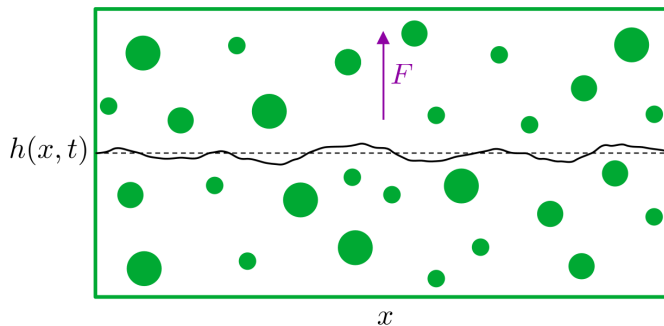


Figure 1.6: Schematic representation of an interface moving in a random medium by the action of a driving force F . The circles are randomly distributed pinning centers.

We can distinguish three main regimes around the depinning transition that takes place at a critical threshold force F_c [11]:

- (i) **Pinned phase** For $F < F_c$, the average interface velocity is zero, and the front gets pinned by the quenched randomness.
- (ii) **Critical moving phase** Near the depinning transition, for $F \gtrsim F_c$, the interface consists of pinned and unpinned regions. If the driven forces are stronger than the pinning forces in a specific area, that part suddenly moves forward. However, it eventually comes to a stop again in another area with strongly pinning sites. As a result, the movement of interface is gradual and steady but occasionally interrupted by sudden movements. The velocity takes the form

$$v \sim (F - F_c)^\theta, \quad (1.20)$$

where θ is the velocity exponent. Besides, if we denote by ξ_{\parallel} and ξ_{\perp} the correlation lengths corresponding to the characteristic length and width of the pinned domains, respectively, they diverge at pinning as

$$\xi_{\parallel} \sim (F - F_c)^{-\nu_{\parallel}}, \quad \xi_{\perp} \sim (F - F_c)^{-\nu_{\perp}}, \quad (1.21)$$

with ν_{\parallel} and ν_{\perp} being the correlation length exponents in the parallel and perpendicular directions of the interface, respectively. When the pinned domains are homogeneously distributed, $\nu_{\parallel} = \nu_{\perp}$.

- (iii) **Large velocity regime** For very large driving forces, $F \gg F_c$, the interface effectively feels a rapidly fluctuating noise, so that the velocity of the interface is proportional to the driving force. In this regime, the thermal fluctuations override the effect of quenched randomness, and the growth may be described by the standard time-dependent KPZ equation.

Thus, there are in principle five critical exponents characterizing the interface at the depinning transition. The first three are the aforementioned velocity exponent θ , Eq. (1.20), and correlation exponents ν_{\parallel} and ν_{\perp} , Eq. (1.21). The remaining two are any two of the three exponents α , z , and β defined in Sec. 1.2, which are related as $z = \alpha/\beta$. However, two scaling relations valid in the vicinity of the depinning transition can be derived, that connect the exponents.

On the one side, the motion of the interface for $F \approx F_c$ is composed of jumps of size $w \sim L^{\alpha}$, where $L \sim \xi_{\parallel}$ near the threshold. These jumps take place over a time period $t \sim \xi_{\parallel}^z$. Thus the velocity of the interface is

$$v \sim \frac{\xi_{\parallel}^{\alpha}}{\xi_{\parallel}^z} \sim (F - F_c)^{\nu_{\parallel}(z-\alpha)}. \quad (1.22)$$

By comparing Eq. (1.22) with Eq. (1.20) one gets the scaling relation

$$\theta = (z - \alpha)\nu_{\parallel}. \quad (1.23)$$

On the other hand, the width of the interface is of the order of ξ_{\perp} . In this case, using Eq. (1.1), one may derive the following scaling relation for the front width,

$$w \sim \xi_{\perp} \sim (F - F_c)^{-\nu_{\perp}} \sim \xi_{\parallel}^{\nu_{\perp}/\nu_{\parallel}} \sim L^{\nu_{\perp}/\nu_{\parallel}} = L^{\alpha}, \quad (1.24)$$

from which one can compute the roughness exponent as

$$\alpha = \nu_{\perp} / \nu_{\parallel}. \quad (1.25)$$

The scaling relations Eq. (1.23) and Eq. (1.25) reduce the number of independent exponents to three.

1.4.2 Quenched noise in stochastic growth equations

The EW and KPZ equations (see Eqs. (1.10) and (1.14), respectively) are the most basic equations that describe how a driven interface moves. In both cases, the noise is assumed to be time-dependent. When the medium is disordered, the quenched noise caused by the disorder can be more significant than the thermal noise. In this case, one may modify both equations in order to take into account the quenched noise term $\eta(\mathbf{x}, h)$, which replaces the thermal noise term $\eta(\mathbf{x}, t)$. This results in the *quenched Edwards-Wilkinson (QEW) equation*,

$$\frac{\partial h(\mathbf{x}, t)}{\partial t} = F + \nu \nabla^2 h + \eta(\mathbf{x}, h), \quad (1.26)$$

and the *quenched Kardar-Parisi-Zhang (QKPZ) equation*,

$$\frac{\partial h(\mathbf{x}, t)}{\partial t} = F + \nu \nabla^2 h + \frac{\lambda}{2} (\nabla h)^2 + \eta(\mathbf{x}, h). \quad (1.27)$$

In both cases, the noise $\eta(\mathbf{x}, h)$ has zero mean and correlations of the form

$$\begin{aligned} \langle \eta(\mathbf{x}, h) \rangle &= 0, \\ \langle \eta(\mathbf{x}, h) \eta(\mathbf{x}', h') \rangle &= N \delta^d(\mathbf{x} - \mathbf{x}') \delta(h - h'), \end{aligned} \quad (1.28)$$

that is, an uncorrelated quenched (time-independent) disorder with amplitude $N > 0$.

The QEW and QKPZ equations describe the growth of an interface in a disordered medium. In the original EW and KPZ equations it is assumed that the disorder is annealed. This means that it fluctuates in the same time scale of the growth of the interface. By contrast, the quenched equations assume that the disorder is fixed in time and space, and it does not change as the interface grows. This noise term is referred to as quenched, which means that it is a random function of \mathbf{x} that is fixed in time.

These growth equations establish two main universality classes: QEW and QKPZ [41]. Some models, including the random-field Ising model (RFIM), are in the QEW universality class [11, 41]; the corresponding exponents related to the depinning transition are $\alpha = 1.25$ and $\beta = 0.871$ [42]. Other models, including the directed percolation depinning (DPD) model (see Sec. 2.6), are in the QKPZ universality class. In this case, $\alpha = \beta = 0.63$ are those of the QKPZ at the transition point, while in the moving phase, $F > F_c$ (see Sec. 1.4), the DPD model features still larger exponents $\alpha_{\text{mp}} = 0.75$ and $\beta_{\text{mp}} = 0.74$ [43]. Further discussion of the QKPZ universality class (or QKPZ classes) is provided in Sec. 1.4.3.

The main symmetry properties of Eqs. (1.26) and (1.27) are very much alike, and they often contend to describe physical interfaces that exhibit a depinning transition. In this scenario, just like with time-dependent noise, whether the nonlinear term $\frac{\lambda}{2}(\nabla h)^2$ is present or not is crucial in determining the interface scaling. Just as important is the value of λ , which in QKPZ diverges close to the depinning transition as

$$\lambda \sim (F - F_c)^{-\phi}, \quad (1.29)$$

where $\phi > 0$. In order to obtain the velocity exponent θ and the exponent ϕ we can impose an average tilt m to the interface and study the mean velocity of the interface v as a function of m and the reduced force $F - F_c$ (see Appendix B).

1.4.3 Some properties of the quenched KPZ equation

At this point, we briefly review some key facts on the QKPZ equation, Eq. (1.27) [44, 45]. This model has a very rich dynamical behavior since up to three different universality classes are identified associated with it. First of all, a pinning-depinning transition exists at a non-zero critical value of the driving force $F = F_c$, such that the interface is pinned (the average velocity is zero) for $F \leq F_c$ or moving (nonzero average velocity) for $F > F_c$.

1. At depinning ($F = F_c$) and for $\lambda > 0$, the QKPZ equation displays the exponent values $\beta = \alpha \simeq 0.63$ and $z = 1$ [46]. This is the case commonly cited when referring to the universality class of QKPZ.

2. For $F \gg F_c$ and $\lambda > 0$, the scaling exponents are those of the standard KPZ universality class [46, 47]. This is to be expected, as discussed in Sec. 1.4.
3. For $\lambda < 0$, Eq. (1.27) also describes a pinning transition, but for a very different class, so-called negative QKPZ, of faceted interfaces [48–50].

For comparison, the scaling behavior of the KPZ equation (which we can recover by replacing the disorder $\eta(\mathbf{r}, h)$ in Eq. (1.27) by similarly uncorrelated, time-dependent noise $\eta(\mathbf{r}, t)$), depends neither on the value of F nor on the sign of λ [11, 51]. These three different universality classes have been fully elucidated recently in experiments of reactive fronts in disordered media [50], which we describe in the next section.

1.5 Rough interfaces in nature

Although the focus of this work is theoretical, we would like to point out that one of the important aspects of surface kinetic roughening is its connection with real growing interfaces. Various examples in nature illustrate the intricate dynamics associated with these interfaces. Consider a scenario in which one of the phases is more stable than the other, hence taking over the region of the metastable state. For example, when one phase is solid and molecules are deposited sequentially on it, such as in thin film growth. Or consider the intriguing notion of an aggregate of particles capable of reproduction, such as living cells. In each of these cases, the interface, or the edge of the aggregate, will move in either direction, typically with fluctuations growing in time [13]. These natural manifestations eloquently justify the importance of exploring theoretical frameworks that can be applied to real-world systems, bridging the gap between theory and practical applications. We will discuss some examples in this section.

1. *Growth dynamics of cancer cell colonies.*

Hurgo *et al.* [52] studied the two-dimensional growth dynamics of HeLa cervix cancer cell colonies. The colonies spread linearly and radially in two dimensions, so that the fronts are one-dimensional. Figure 1.7 shows the evolution of a cell colony spreading linearly because of cell

division. The front moves along the normal direction and fluctuations begin to emerge because of the stochastic nature of cell behavior. The snapshots also display the increase of the front roughness over time. The analysis of the roughness of these colony fronts yields the critical exponents $\alpha = 0.50(5)$, $\beta = 0.32(4)$, and $z = 1.5(2)$. These scaling exponents are consistent with those of the 1D KPZ universality class.

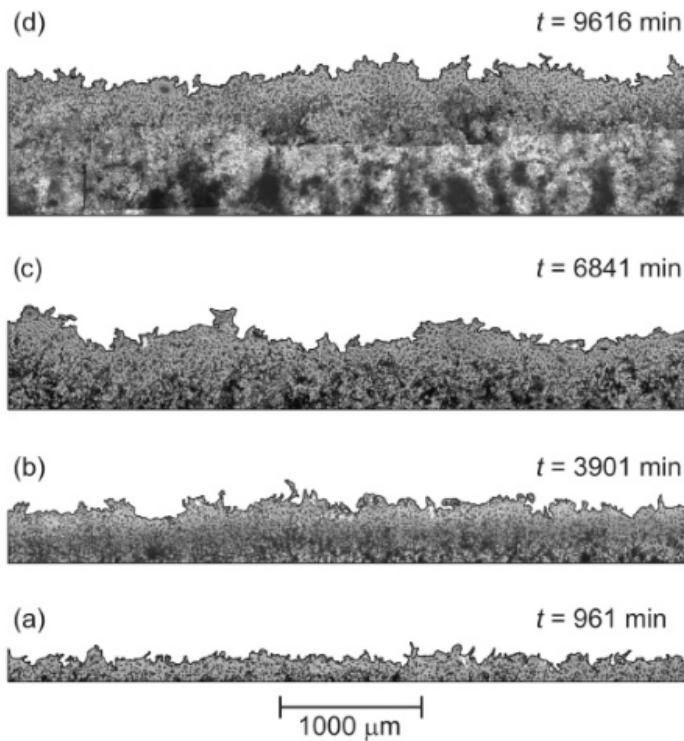


Figure 1.7: Front evolution of cancer cell colonies [52].

2. Kinetic roughening of paper burning front.

Propagation of a burning front in paper was first studied by Zhang *et al.* [53] (see Fig. 1.8a). They designed an experiment where a sheet of paper is burnt uniformly using slow combustion, i.e. flameless fire, and the fluctuation of the propagating front was consistent with a roughening exponent $\alpha \approx 0.70$. Nearly ten years later, Myllys *et al.* [54] carried out an extensive study on the dynamics of these fronts, using different types

of paper. The time evolution of these fronts are shown in Fig. 1.8b. Their results show a crossover in the data from short-time behavior (higher apparent exponents) to asymptotic long-time regime, where the scaling properties are well described by the 1D KPZ universality class as well.

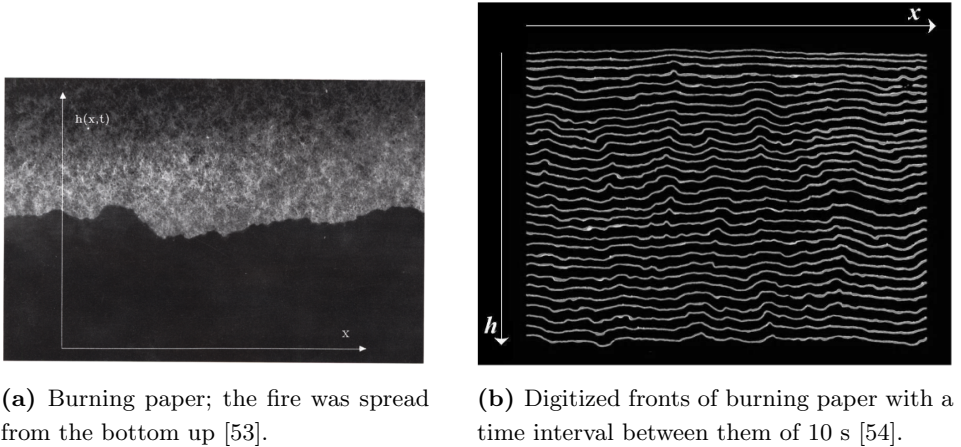
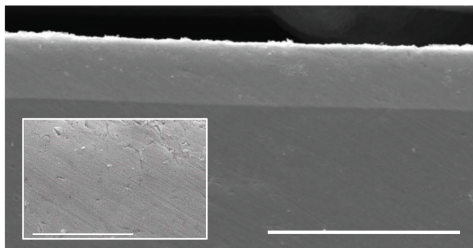


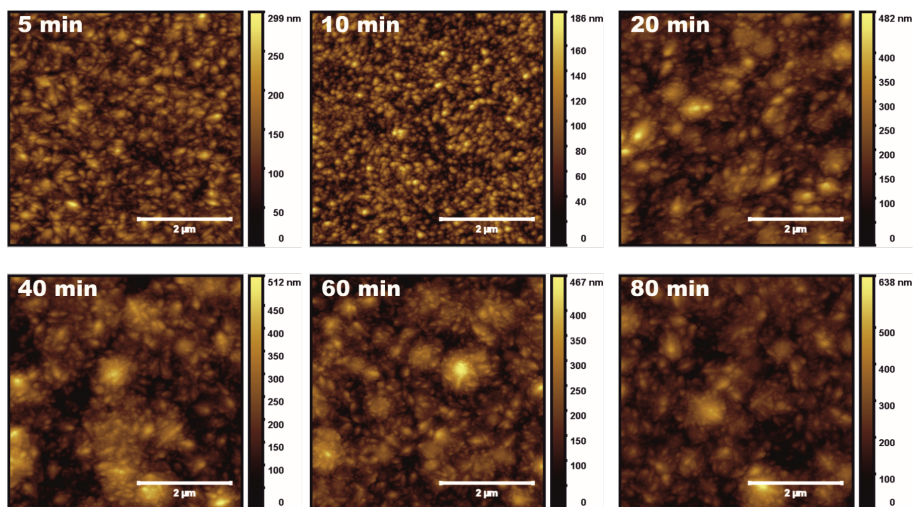
Figure 1.8: Slow combustion of a paper.

3. *Surface growth dynamics of nanofilms.*

In Ref. [55], Orrillo *et al.* studied the surface growth dynamics of NiW alloy substrates obtained by electrochemical deposition. This deposition technique is characterized by a growth dynamics resulting from the competition between the diffusive transport of metal ions through the electrolyte to reach the film surface and the kinetics of their final attachment. There are many other techniques that also result in kinetically rough surfaces; for instance, those inducing epitaxial growth [56, 57]. Figure 1.9a displays a characteristic cross-image of NiW film electrodeposited on polished steel substrate for 60 minutes. The surface morphologies (top view) of NiW films for different times are shown in Fig. 1.9b. Using the scaling concepts of kinetic roughening, the authors concluded that the observed long-time scaling behavior was consistent with the 2D KPZ universality class. In particular, they measured $\beta = 0.20(5)$ after 10 minutes [55].



(a) Cross-section image of NiW film electrodeposited on steel substrate for 60 min. Inset: Magnified image. Image from Ref. [55].



(b) Surface morphologies of NiW films electrodeposited for times as indicated in each case [55]. The color range indicates the relative height difference between points in the same image. Images from Ref. [55].

Figure 1.9: Deposition of nanostructured NiW alloy films by electrodeposition.

4. Chemical reaction front in disordered media.

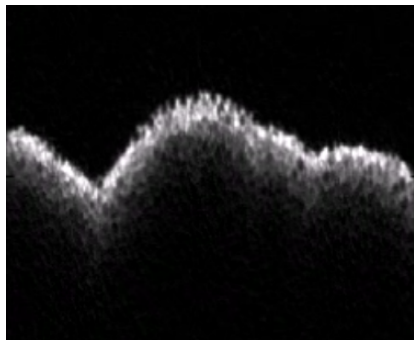
Another very interesting work is Ref. [50], where Atis *et al.* studied the propagation of a chemical reaction front in a disordered medium. They controlled an external flow and observed up to three different universality classes varying the mean flow velocity. The experiment was made with an autocatalytic reaction resulting in a front separating the reacted phase from the unreacted phase. The disordered medium was generated with

a mixture of glass beads packed inside a rectangular cell.

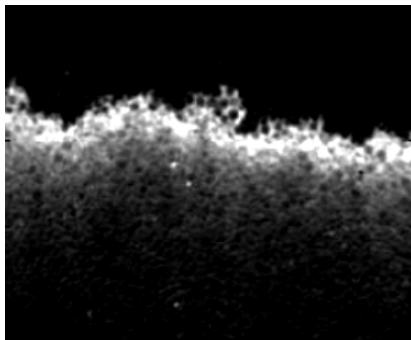
In the absence of flow, the reaction fronts are uniformly moving through the glass beads with a smooth front shape (see Fig. 1.10a) and with a constant velocity $V_\chi = 11.2 \mu\text{m/s}$. The control parameter is defined as $F = (\bar{U} + V_\chi)/V_\chi + 0.38$, where \bar{U} is the mean flow velocity. The front exhibits distinct scaling behavior depending on F :

- For $|F| > 2.5$, which corresponds to $\bar{U} > 12.5$ and $\bar{U} < -43.4 \mu\text{m/s}$, the front propagates in the same direction as the mean flow (even if the chemical reaction velocity is oriented in the opposite direction) with a velocity proportional of F (see Fig. 1.10b). The front, of either orientation, exhibits scale-invariant fluctuations with statistical properties in agreement with the 1D KPZ universality class.
- For $F < 2.5$, some regions of the front pin to the inhomogeneities of the medium. When the opposite flow is amplified, the pinned portions become larger. At $F_{c+} \approx 0.56$ ($\bar{U} \approx -14.896$), the front eventually stops and remains static. The scaling exponents in this configuration are consistent with those of the positive 1D QKPZ universality class. The front undergoes a depinning transition for $F \rightarrow F_{c+}$. Below F_{c+} , the transient front propagation becomes very short-lived; for $F \approx 0$, the front is static almost instantaneously.
- For $-2.22 \lesssim F \lesssim 0$, the front quickly becomes static after a transient propagation and displays a particular sawtooth pattern (see Fig. 1.10d). The receding fronts are consistent with the negative 1D QKPZ universality class. Another depinning transition occurs at $F_{c-} \approx -2.22$, below which the triangular shapes become unstable and the front goes back to the moving phase.

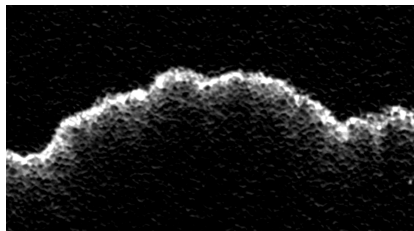
This system, which combines chemical wave propagation with disordered flow in a porous medium, exhibits self-affine structures that display scaling exponents consistent with either the KPZ or QKPZ classes (see Sec. 1.4.3). Notably, by adjusting a single parameter, this system transitions through three universality classes, making it an exceptionally comprehensive example for studying growth phenomena.



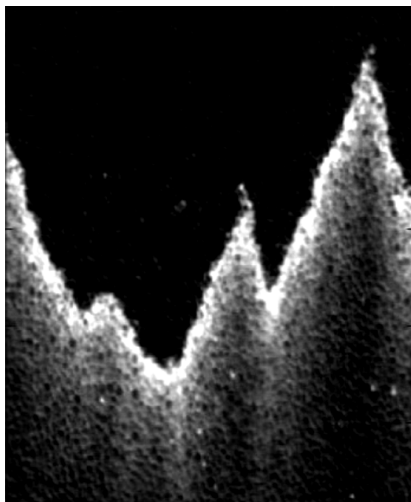
(a) Reaction front in the absence of flow, $F \simeq 1.38$. The front is moving from the bottom to the top.



(b) Upward propagating reaction front at large flow rate, $F \simeq 3.16$. In this configuration, both the chemical reaction wave and the flow velocity are towards the top.



(c) Upward propagating reaction front at $F \simeq 0.58$. In this configuration, the chemical wave velocity is oriented towards the top and the mean flow velocity towards the bottom.



(d) Downward propagating reaction front at $F \simeq -1.25$. In this configuration the chemical wave velocity is oriented towards the top and the mean flow velocity towards the bottom.

Figure 1.10: Reaction front propagation for several F . The images are captures of the movies included in the supplemental material of Ref. [50].

In conclusion, the formation of self-affine structures in these different examples raises the important question of universality in out-of-equilibrium phenomena.

Chapter 2

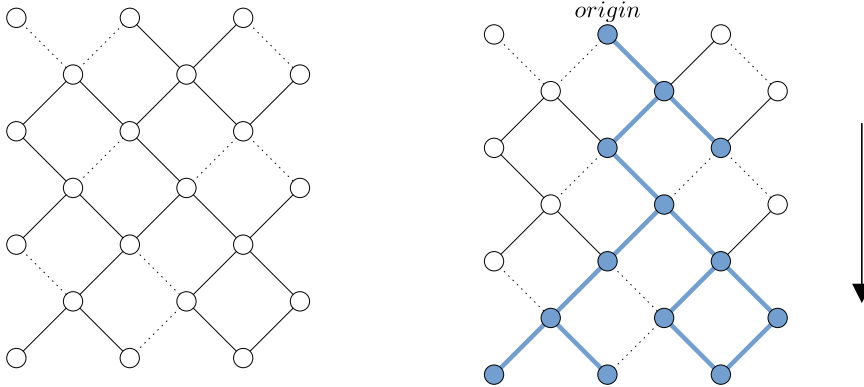
Directed Percolation

The word percolation refers to the movement and filtering of fluids through porous materials. For instance, in coffee percolation, soluble compounds leave the coffee grounds and join the water to form the liquid coffee that one drinks. Many percolation models have been described in the literature [58–60]. From the viewpoint of this thesis, we are interested in Directed percolation (DP) models. These restrict the flow of the agent along a given direction, for example, due to the effect of gravity [61, 62].

2.1 Lattice model and scaling behavior

Simple models for percolation in a lattice are represented by pores of the filter (sites of the lattice) and channels between neighboring pores (bonds of the lattice that connect adjacent sites). The permeability of the filter is determined by the percolation probability p , which controls the connectivity of the channels. Figure 2.1a shows an example of a lattice with bonds and channels, these channels being open (solid lines) or closed (dashed lines) independently with a random probability p . Varying the probability p one finds that there is a phase transition, the so-called percolation transition, from a macroscopically permeable phase to an impermeable one. This transition is continuous and takes place at a critical threshold p_c .

If the percolation is isotropic, or undirected, the fluid may pass through open channels in any direction. On the contrary, in DP, flow is restricted



(a) Scheme of bond percolation lattice. Channels are open (solid lines) or closed (dashed lines) independently with a probability p .

(b) Scheme of bond directed percolation, starting with a single wet site at the origin.

Figure 2.1: Schemes of bond directed percolation.

to a preferred direction in space (see Fig. 2.1b). Both models exhibit a percolation transition, but the corresponding critical thresholds and universal properties are markedly different. Hereafter, we will focus on DP, which represents one of the simplest and most important universality classes.

DP may be converted into a stochastic process by interpreting the preferred direction as a temporal coordinate [61]. For example, in Fig. 2.1b, one may enumerate horizontal rows by a temporal index t . Knowing the configuration of wet sites at time t one may compute the next configuration at time $t + 1$ using simple probabilistic rules. If one interprets wet sites as particles and dry sites as vacancies, these rules are the same as those of a reaction-diffusion process:

- (i) *Death*: if both channels to the nearest neighbors at time $t + 1$ are blocked, the particle disappears by a death process, $A \rightarrow \emptyset$.
- (ii) *Diffusion*: if only one channel is open, the particle diffuses to such a position, $A \rightarrow A$.
- (iii) *Offspring*: if both channels are open the particle duplicates itself, creating an offspring, $A \rightarrow 2A$.

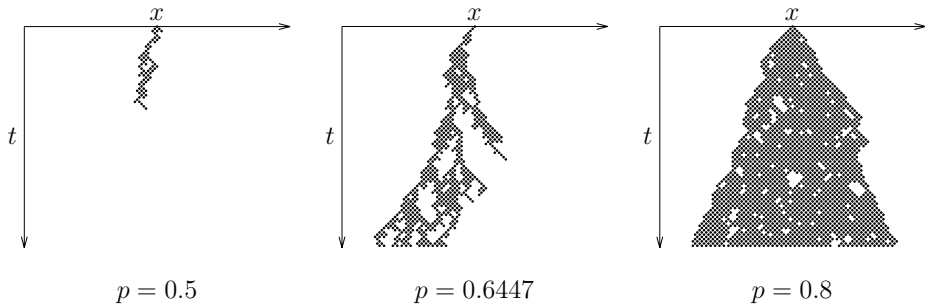


Figure 2.2: DP clusters grown from a single particle for different percolation probabilities p .

- (iv) *Coalescence*: if two particles happen to reach the same site, they merge to a single one by a coalescence process, $2A \rightarrow A$.

Therefore, the DP can be interpreted as a reaction-diffusion process and, in general, any stochastic particle process that follows these rules belongs to the universality class of DP.

It is straightforward to simulate such a system. Representative results of the generated clusters for various percolation probabilities are shown in Fig. 2.2. For $p < p_c$, all generated clusters remain finite in size. On the contrary, for $p > p_c$, some clusters (but not all) extend infinitely throughout the entire system. These two cases are clearly separated by a transition point at $p_c = 0.6447$ [63]. At this critical point, clusters of all sizes are produced, with large-scale properties that are universal, i.e. independent of the specific microscopic details of the model under consideration.

The phase transition shown on DP is also called an absorbing phase transition. Indeed, there is a transition from an active to an inactive phase, which is an absorbing state because these configurations can be reached by the dynamics but cannot be left. This type of transition occurs, for example, in models of the spread of an infectious disease. In these models, the lattice sites are considered as individuals that can be healthy or infected. In the active phase, infected individuals can either recover or infect their nearest neighbors. Depending on the infection rate, the spreading process may either survive or evolve into an absorbing state where the infection is completely eliminated (inactive state) [60].

Absorbing phase transitions are characterized by at least the independent critical exponents β_ρ , ν_\perp and ν_\parallel , which will be defined below. In particular, the exponent β_ρ describes the scaling of the density of particles in the active phase

$$\rho \sim (p - p_c)^{\beta_\rho}, \quad (2.1)$$

where p is the percolation probability. This exponent β_ρ should not be confused with the growth exponent $\beta \equiv \beta_w$ defined in Eq. (1.1). β_ρ is defined instead as the exponent that characterizes the power-law growth of the order parameter near the critical probability. It is analogous to that of the Ising model transition, where the magnetization, m , near the critical point (Curie temperature, T_c) scales as $m \sim (T - T_c)^{\beta_m}$.

Conversely, exponents ν_\perp and ν_\parallel describe the scaling of the two correlation lengths that characterize the transition in DP: the one measured in the direction where the percolation is directed $\xi_t \equiv \xi_\parallel$, and the one which is measured in the perpendicular direction $\xi_x \equiv \xi_\perp$ (see Fig 2.1b: t is the direction parallel to the percolation and x the perpendicular direction). They both diverge close to criticality as

$$\xi_\parallel \sim (p - p_c)^{-\nu_\parallel}, \quad \xi_\perp \sim (p - p_c)^{-\nu_\perp}, \quad (2.2)$$

where the exponents ν_\parallel and ν_\perp are generally different (i.e., there is not symmetry between space and time). These magnitudes also evolve over time. Starting with a fully occupied lattice, the density decays with time at the transition $p = p_c$ as

$$\rho(t) \sim t^{-\alpha_\rho}. \quad (2.3)$$

Using Eqs. (2.1), (2.2), and (2.3) it follows that

$$\alpha_\rho = \beta_\rho / \nu_\parallel. \quad (2.4)$$

As before, α_ρ is not to be confused with the roughness exponent $\alpha \equiv \alpha_w$ of Eq. (1.1). The x -correlation length grows with time as

$$\xi_\perp \sim t^{1/z}, \quad (2.5)$$

where z is the dynamic exponent, as defined in Eq. (1.4). Using Eqs. (2.2) and (2.5),

$$\xi_\perp \sim (p - p_c)^{-\nu_\perp} \sim \xi_\parallel^{\nu_\perp/\nu_\parallel} \sim t^{1/z}, \quad (2.6)$$

from which the exponent z that characterizes DP fulfills the scaling relation

$$z = \frac{\nu_{\parallel}}{\nu_{\perp}}. \quad (2.7)$$

As for kinetic roughening, z quantifies the power-law increase of the correlation length; in this case, it is the x -correlation length ξ_{\perp} . When the correlation length ξ_{\perp} becomes comparable with the lateral size of the system, these asymptotic power laws break down if the system reaches the absorbing state. If L is the lateral size of the system, the absorbing state is reached at a characteristic time t_f that scales as

$$t_f \sim L^z; \quad (2.8)$$

analogous to Eq. (1.2) discussed in Sec. 1.2.

2.2 DP conjecture

The DP conjecture, that was formulated by Janssen and Grassberger [64, 65], states that a particular model typically falls into DP universality if it satisfies the following conditions:

- The model displays an absorbing phase transition.
- The order parameter of the transition is a non-negative scalar.
- The dynamic rules are short-ranged.
- The system lacks any exceptional characteristic, like unconventional symmetries, conservation laws, or quenched randomness.

The universality class of DP is highly resilient: not only there have not been any counterexamples discovered so far for this hypothesis [66, 67], but there are even specific models that, not fulfilling some of these conditions, still belong to this universality class.

2.3 Mean-field approximation

Through the interpretation of DP as a stochastic particle processes, a simple mean-field (MF) approximation can be performed in terms of the mean

particle density as [61]

$$\frac{\partial \rho(t)}{\partial t} = \mu_p \rho(t) - \mu_d \rho(t) - \mu_c \rho(t)^2, \quad (2.9)$$

where μ_p is the rate for offspring production (which corresponds to a linear term for particle gain), μ_d is the rate for particle death (which corresponds to a linear term for particle loss), and μ_c is the rate for coalescence (which corresponds to a quadratic loss term).

Defining

$$\tau = \mu_p - \mu_d, \quad (2.10)$$

which, as we will see below, plays the role of a control parameter, the solution of the mean-field equation in the asymptotic limit of large t is [61]

$$\rho(t) \sim \begin{cases} -\tau \left(\mu_c - \frac{\tau}{\rho_0} \right)^{-1} e^{\tau t} & \xrightarrow[t \rightarrow \infty]{} 0 & \text{if } \tau < 0, \\ (\rho_0^{-1} + \mu_c t)^{-1} & \xrightarrow[t \rightarrow \infty]{} 0 & \text{if } \tau = 0, \\ \frac{\tau}{\mu_c} + \frac{\tau}{\mu_c^2} \left(\mu_c - \frac{\tau}{\rho_0} \right) e^{-\tau t} & \xrightarrow[t \rightarrow \infty]{} \frac{\tau}{\mu_c} & \text{if } \tau > 0, \end{cases} \quad (2.11)$$

where ρ_0 denotes the density at $t = 0$. The solution $\rho = 0$ corresponds to the absorbing state, while for $\tau > 0$ the solution approaches also a steady-state but with non-vanishing stationary density of active sites $\rho = \tau/\mu_c$. The transition takes place at $\tau = \tau_c = 0$, where one obtains an algebraic decay. Comparing these results with Eqs. (2.1) and (2.3), and using $\alpha_\rho = \beta_\rho/\nu_\parallel$ one gets

$$\begin{aligned} \beta_{\rho, \text{MF}} &= 1, \\ \alpha_{\rho, \text{MF}} &= 1, \\ \nu_{\parallel, \text{MF}} &= 1. \end{aligned} \quad (2.12)$$

To derive the third critical independent exponent, one cannot neglect the spatial dependence. Therefore, a diffusion term in the mean field equation must be included, representing the diffusion motion to which the particles are subjected:

$$\frac{\partial \rho(t, \mathbf{x})}{\partial t} = \tau \rho(t, \mathbf{x}) - \mu_c \rho(t, \mathbf{x})^2 + D \nabla^2 \rho(t, \mathbf{x}), \quad (2.13)$$

where D is the diffusion constant. Inserting the scaling Ansatz $\rho(t, \mathbf{x}) = (\mu_c t)^{-1} f(\mathbf{x}/t^{1/z})$, one obtains a consistent solution only if $z_{\text{MF}} = 2$ [61]. Therefore,

$$\nu_{\perp, \text{MF}} = 1/2. \quad (2.14)$$

2.4 Phenomenological Langevin equation

In order to go beyond mean-field, we need to introduce fluctuations, so we end up with the the phenomenological Langevin equation which reads as [64]:

$$\frac{\partial \rho(t, \mathbf{x})}{\partial t} = \tau \rho(t, \mathbf{x}) - \mu_c \rho(t, \mathbf{x})^2 + D \nabla^2 \rho(t, \mathbf{x}) + \eta(t, \mathbf{x}). \quad (2.15)$$

The noise $\eta(t, \mathbf{x})$ accounts for fluctuation effects on a coarse-grained level. It is a density-dependent Gaussian noise with correlations

$$\begin{aligned} \langle \eta(t, \mathbf{x}) \rangle &= 0, \\ \langle \eta(t, \mathbf{x}) \eta(t', \mathbf{x}') \rangle &= \kappa \rho(t, \mathbf{x}) \delta(t - t') \delta^d(\mathbf{x} - \mathbf{x}'), \end{aligned} \quad (2.16)$$

where κ controls the noise amplitude.

Using dimensional analysis, it can be demonstrated from the Langevin equation that the upper critical dimension for DP is $d_c = 4$. For $d > 4$ the noise can be neglected, and the mean-field exponents are accurate; in these cases, the diffusive mixing is strong enough to suppress correlations. Below d_c , on the contrary, fluctuations become significant, and the exponents need to be determined through a RG calculation or via numerical simulations. Table 2.1 summarizes the values of the estimated critical exponents for $d < d_c$ and the mean-field ones for DP.

2.5 Contact process

The contact process (CP) is a well-studied lattice model that belongs to the universality class of DP. The CP was originally introduced by Harris [73] as a model for epidemic spreading. It studies the dynamics of spreading processes in systems with active and inactive states.

Table 2.1: Critical exponents for the DP universality class [61]. There are only three independent exponents, the relations between them being $\alpha_\rho = \beta_\rho/\nu_\parallel$ and $z = \nu_\parallel/\nu_\perp$. The numbers in brackets give the estimated uncertainty in the last digit(s).

	$d = 1$ [68, 69]	$d = 2$ [70, 71]	$d = 3$ [72]	MF
β_ρ	0.276486(8)	0.583(3)	0.813(9)	1
ν_\perp	1.096854(4)	0.733(8)	0.584(5)	1/2
ν_\parallel	1.733847(6)	1.295(6)	1.110(10)	1
α_ρ	0.159464(6)	0.4505(10)	0.732(4)	1
z	1.580745(10)	1.7660(16)	1.901(5)	2

The model is composed of a lattice in which each site can be in either an active state [$s_i(t) = 1$] or in an inactive state [$s_i(t) = 0$] [61, 62, 74]. The active sites have the ability to activate neighboring inactive sites, leading to a cascading effect of activation. The dynamic is characterized by two key parameters: the infection rate and the recovery rate. The infection rate represents the probability of an active site infecting an adjacent inactive site, while the recovery rate represents the probability of an active site returning to the inactive state.

The absorption transition occurs when the infection rate exceeds a critical value. Below the critical threshold of the infection rate, the system reaches a steady state where all sites become inactive, and the activity completely dies out; this is the absorbing state. As the infection rate increases and surpasses the critical threshold, a phase transition takes place. The system undergoes an abrupt change and starts exhibiting a persistent active state.

In the standard CP, the transitions rates, T , are

$$T[0 \rightarrow 1] = \frac{\lambda n}{2d}, \quad T[1 \rightarrow 0] = 1, \quad (2.17)$$

where n is the number of active neighbors, d is the dimension of the lattice, and λ is the parameter that controls the infection rate; it plays the same role as the percolation probability in bond DP [61]. The critical value λ_c depends on the dimension d and is listed in Table 2.2.

There are a number of ways of implementing the CP in a simulation algorithm, all equivalent in terms of scaling behavior. A widely used practice is to maintain a list of all infected locations. Each time step involves selecting an active node at random from the list, and selecting either creation, with probability $p = \lambda/(1 + \lambda)$ or annihilation, with probability $1 - p$. In the case of annihilation, the selected node becomes inactive. In the case of creation, a randomly nearest neighbor of the active node is chosen and, if it is inactive, then it becomes active. The time increment Δt associated with an event is $1/N_p$, where N_p is the number of active nodes.

The relation between p and λ is derived as follows. Since the parameter λ corresponds to the number of infections per unit time, $p = \lambda\Delta t$ is the probability of infection within a time interval Δt . In the same way, since annihilation of particles occurs at unitary rate, the probability to remove a particle is Δt . This means that the transitions of Eq. (2.17) are carried out with the probabilities $T[0 \rightarrow 1]\Delta t$ and $T[1 \rightarrow 0]\Delta t$, respectively. Applying the normalization condition, we obtain that $\Delta t = 1 - p$. Therefore, $p = \lambda/(1 + \lambda)$ [75, 76].

Table 2.2: Critical points λ_c of the contact process on a hypercubic lattice in d dimensions [72, 77, 78].

	$d = 1$	$d = 2$	$d = 3$
λ_c	3.297848(22)	1.64877(3)	1.31686(1)

2.6 Directed Percolation Depinning

The depinning transition allows one to establish a connection between growth processes and DP. The directed percolation depinning model [11, 44, 46, 47], which explains, for example, fluid motion in a disordered medium, exemplifies the depinning transition in the QKPZ universality class. As we will see below, this depinning transition is related to an underlying DP process oriented perpendicular to the direction of interface growth; the front motion is arrested by the emergence of a directed percolation cluster of quenched disorder.

Let us imagine a fluid trying to advance through a disordered medium. This system may be discretized into a lattice with a fraction p of blocked cells, representing the quenched disorder. The blocked cells act as obstacles to the advance of the fluid, which is free to move forward on unblocked cells. At time $t = 0$, the interface is a horizontal line at the bottom of the lattice. Each time step, an unblocked cell is chosen randomly from among the nearest neighbors of the interface. This cell is now wet, and the interface advances to this position. The process is then repeated iteratively. When an unblocked cell is chosen to make it wet, any cell below it in the same column becomes then wet too, even if it was blocked. A schematic of this process can be seen in Fig. 2.3.

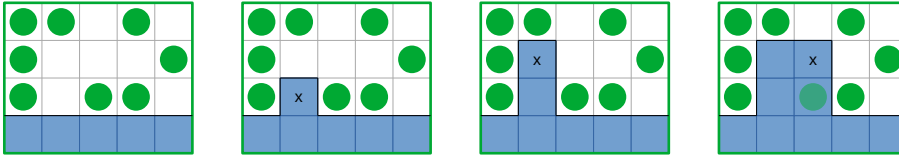


Figure 2.3: Evolution of a DPD model interface, which is shown by a black line. The wet cells are blue and the green circles are obstacles to the growth of the interface (blocked cells). The cross denote the unblocked cell chosen in each step to advance.

For p below a critical value p_c , the interface propagates without stopping, while for $p > p_c$ the interface is pinned by the blocked cells. In Fig. 2.4 one may appreciate a pinned interface, where the fluid has flowed until it reaches a connected cluster of blocked cells. Such a directed path is actually a path on a directed percolation cluster, hence the DP process occurs perpendicular to the direction along which the interface is growing.

Two correlation lengths characterize the transition, one parallel to the interface ξ_{\parallel} (measuring the average length) and one perpendicular to it ξ_{\perp} (measuring the width). Near p_c , they both diverge as seen in Eq. (1.21) in the context of depinning transition, or as seen in Eq. (2.2) in the context of percolation transition. The role of ξ_{\parallel} to the interface in the context of depinning transition is that of ξ_{\parallel} to the directed direction in the context of DP.

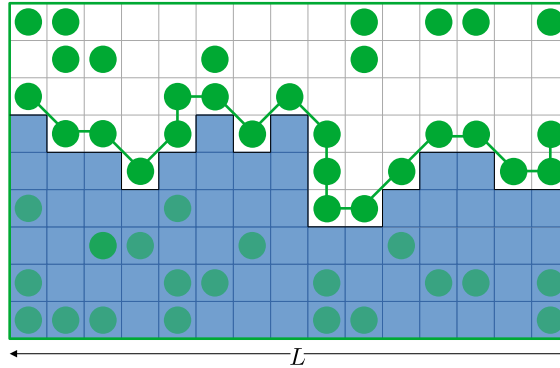


Figure 2.4: DPD pinned interface. The cluster of blocked cells that blocks the interface is indicated by a green line.

From numerical calculations, the correlation exponents values are known to be $\nu_{\parallel} = 1.733$ and $\nu_{\perp} = 1.097$ [79, 80], according to the critical exponent of DP (see Table 2.1). The roughness exponent α can be computed from these exponents, using Eq. (1.25); its value is $\alpha = 0.633(1)$ [79, 80], in accordance with the QKPZ universality class at the depinning transition. As for the critical probability, its value is $p_c = 0.470$ [43, 80], consistent with DP calculations.

Knowing that $\xi_{\parallel} > \xi_{\perp}$, the correlation lengths fulfill $\xi_{\parallel} \gg \xi_{\perp}$. For this, the jump between two pinned clusters where the interface is pinning takes a time $t \sim \xi_{\parallel}$. Comparing with Eq. (1.4), it follows that the dynamic exponent is $z = 1$. This exponent, consistent with QKPZ class, differs from that of DP and Eq. (2.7) is not fulfilled. Recall that, in DP [see Eq. (2.5)], the exponent z quantifies the power-law increase of the correlation length perpendicular to the directed direction; here, we are interested in the exponent z that scales with the correlation length parallel to the growing interface.

To estimate the interface velocity one may assume that it advances vertically a distance equal to the width of the blocking directed path, which is of the order of ξ_{\perp} . Thus, assuming $t \sim \xi_{\parallel}$ the velocity scales as

$$v \sim \xi_{\perp}/\xi_{\parallel} \sim |p - p_c|^{\nu_{\parallel} - \nu_{\perp}}, \quad (2.18)$$

so that, using Eq. (1.20), the velocity exponent is

$$\theta = \nu_{\parallel} - \nu_{\perp}, \quad (2.19)$$

whose value is $\theta = 0.636$ [79, 80]. In order to clarify ideas, all the DPD exponents have been summarized in Table 2.3, where the relations between them have also been pointed out.

The interest of the DPD model lies in the fact that it illustrates the depinning transition in the QKPZ universality class, while at the same time it can also be related to the universality class of DP. Indeed, DPD can be described by the QKPZ equation for $F \sim F_c$, i.e., near the critical point.

For $F \gg F_c$, the interface grows proportionally to F , in such a fast way that the thermal noise becomes relevant again over the quenched noise. In this case, the growth of the interface becomes characterized by the time-independent KPZ universality class.

Table 2.3: Critical exponents of the DPD model and the QKPZ universality class at the depinning transition, for $d = 1$. The exponents β , α , and z are those defined in Sec. 1.2 in the context of kinetically rough interfaces, and are related by Eq. (1.3). The exponents θ , ν_{\parallel} , and ν_{\perp} are defined in Sec. 1.4 in the context of depinning transitions, and verify Eqs. (1.23) and (1.25). The transition in standard DP is also characterized by two correlation exponents, ν_{\parallel} and ν_{\perp} [see Eq. (2.2)], which are consistent with the values of DPD; note that Eq. (2.7) is not fulfilled. Moreover, in this section, we have demonstrated that in DPD the velocity exponents obeys Eq. (2.19).

β [46]	α [46]	z [46]	ν_{\parallel} [79, 80]	ν_{\perp} [79, 80]	θ [79, 80]
0.63	0.63	1	1.733	1.097	0.636

2.7 DP in nature

The DP universality class has been extensively studied in both theory and simulations over the past 30 years [60]. It has been firmly established that the vast majority of absorbing phase transitions exhibit the same critical behavior, aligning with the characteristics of DP. This outcome is not surprising, considering that DP represents the simplest scenario where a single effective absorbing state exists without any additional symmetry or conservation laws.

Despite this, it has been challenging and time-consuming to find ex-

perimental evidences of DP criticality. As stated in Ref. [81], the main difficulties arise from the need to eliminate long-range interactions, handle macroscopic systems to control quenched disorder, and observe them on sufficiently long scales to accurately measure critical behavior. In this section we will have a look at some of the work that has overcome these challenges, being able to connect DP theory with experimental observations [81–84].

Lemoult *et al.* [84] characterized the transition that gives rise to turbulence in basic shear flow, specifically in a Couette flow. The authors use a combination of experimental and numerical simulation methods to investigate the critical behavior and concluded that it undergoes a second-order transition that falls into the DP class for $d = 1$.

In fact, the spreading of turbulence in shear flows can be described as a contact process: turbulence cannot arise spontaneously due to the linear stability of the laminar state, but can only be generated by interactions with pre-existing turbulent domains. The laminar state in Couette flow qualifies as the absorbing state. Analogous to the probability of percolation, the transition to sustained turbulence is governed by a single parameter, in this case the Reynolds number.

The experiment was conducted in a circular Couette geometry, where a fluid is contained between two concentric cylinders. This setup offers the advantage of periodic boundary conditions in the streamwise (azimuthal) direction, allowing for unlimited observation times compared to pipes and channels. To capture the critical behavior, the measurements require large aspect ratios, as the relevant length scales are expected to diverge at the critical point. To ensure a constant Reynolds number over the long observation times, viscosity changes of the working fluid were minimized by controlling its temperature. This was achieved by circulating fluid of constant temperature around the outside of the outer cylinder and on the inside of the inner cylinder.

Images for Couette flow experiments below, at and above the critical point, are shown in Fig. 2.5. Below the critical point turbulence disappears after sufficiently long times. At the critical point turbulence survives, but only occupies a small fraction of the domain. Sufficiently far above the critical Reynolds number turbulent patches occupy most of the flow domains. The turbulent fraction plays the role of the order parameter.

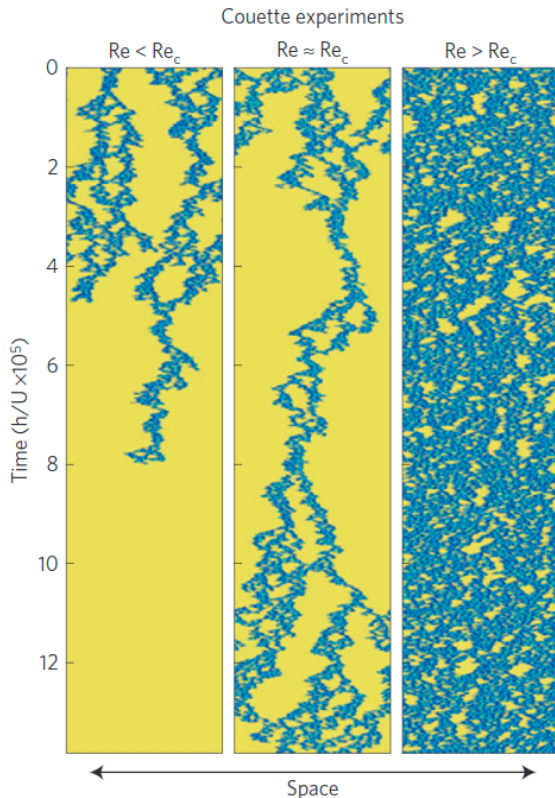


Figure 2.5: Space-time plots for Couette flow below, at and above the critical point. Laminar regions are shown in yellow and turbulent regions are shown in blue. From [84].

The critical exponents measured in the experiments were $\beta_\rho = 0.25(4)$, $\nu_\perp = 1.00(21)$ and $\nu_\parallel = 1.75(29)$, in good agreement with the critical exponent of DP shown in Table 2.1 for $d = 1$.

Alternatively, Takeuchi et al. [81, 83] studied the critical behavior of a phase transition between two topologically different turbulent states in nematic liquid crystals, yielding a complete set of static critical exponents in full agreement with those of the DP class in $d = 2$ dimensions.

They worked within electrohydrodynamic convection regimes, which occur when a thin layer of nematic liquid crystal is subjected to a sufficiently strong external voltage. By varying the voltage V , two topologically different turbulent states, called dynamic scattering modes 1 and 2 (DSM1 and DSM2) were observed. The difference between them is the density of topo-

logical defects; in DSM1 the density remains very low and in DSM2 these defects are considerable and lead to a lower light transmittance. We have already mentioned experiments with turbulent liquid crystal in Sec. 1.3.3.

Specifically, they studied the transition between these two states and considered it an absorbing phase transition, wherein DSM1 acts as the absorbing state. Above the threshold V_c , which signifies the onset of DSM2, patches of DSM2 dynamically move within a background of DSM1 (see Fig 2.6). The order parameter is defined as the ratio of the surface area occupied by active (DSM2) regions to the total area.

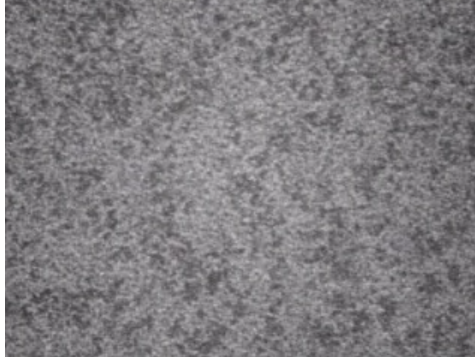


Figure 2.6: Screenshot of Movie S1 [81] at $V > V_c$. Active (DSM2) regions appear darker than the absorbing DSM1 background.

Table II in [83] collects the critical exponent that characterize the critical behavior of the DSM1-DSM2 transition. To summarize some of these results, they estimated $\beta_\rho = 0.59(4)$ and $\alpha_\rho = 0.48(5)$. All reported measured exponent values agree within one percent with those of the DP universality class for $d = 2$ (see Table 2.1).

Chapter 3

Methodology

In this chapter, we outline the methodology systematically used in the subsequent chapters. The observables represent the measurements computed in every system introduced throughout this thesis. Regarding all computed quantities, we estimated the associated uncertainties via the jackknife method, as explained below.

3.1 Observables

The main step in surface growth studies is to establish a correspondence between a given particle model and the corresponding interface dynamics. In some cases, as we will see in Chapters 4 and 5, such a correspondence arises trivially, as one observes the particles growing in some direction and thus establishes the interface as the separation between an occupied and an empty phase. In other cases, the interface is not related to the motion of the particles, but represents other quantities. For example, in Chapter 6, the “heights” that define the interface are the activities of particles.

In all cases, the interface or front position is defined by a set of local heights $h(i, t)$, where i denotes the substrate positions at which the front is measured. If the system is growing in a lattice, the number of positions equals the sites of the lattice. If the system is off-lattice, columns of a certain width are defined to discretize the system. Once the local heights have been established, all the magnitudes of the front under study are derived from it.

Given the aforementioned set of heights, the front position is simply defined as the mean height, that is, the average of the local heights $h(\mathbf{x}, t)$:

$$\bar{h}(t) = \frac{1}{L^d} \sum_{\mathbf{x}} h(\mathbf{x}, t), \quad (3.1)$$

where L denotes the lateral length of the substrate and d is the system dimension. If the system shape is not square, one has to take into account the size in each direction: L_x, L_y, \dots

The front width, or roughness, $w(L, t)$, is defined as the standard deviation of the front values,

$$w^2(L, t) = \left\langle \overline{[h(\mathbf{x}, t) - \bar{h}(t)]^2} \right\rangle. \quad (3.2)$$

Throughout this thesis, the difference between symbols must be noted. The overline symbol $\overline{(\dots)}$ for a given observable, denotes its space average. The angle brackets $\langle \dots \rangle$ denotes instead average over different realizations of the noise (or, interchangeably initial configurations, or simply runs).

The typical time evolution of $w(L, t)$ has been detailed in Sec. 1.2, specifically in Eq. (1.1). Under these conditions (the simplest ones), the roughness $w(L, t)$ satisfies the so-called Family-Vicsek (FV) scaling law [11, 51]

$$w(L, t) = t^\beta f(t/L^z), \quad (3.3)$$

where β and z are the growth and dynamic exponents, respectively. In Eq. (3.3) the scaling function has two asymptotic limits. For $t \ll L^z$ one has $f(y) \sim \text{const}$; thus, in such a limit

$$w(L, t) \sim t^\beta. \quad (3.4)$$

On the other hand, for $t \gg L^z$, it is $f(y) \sim y^{-\beta}$, so that $w = \text{const} \equiv w_{\text{sat}}$, with w_{sat} being a saturation value which scales with the lateral size of the system as

$$w_{\text{sat}}(L) \sim L^\alpha, \quad (3.5)$$

where α is the roughness exponent. Recall that α , β , and z are related by $\alpha = \beta z$ [Eq. (1.3)]. Also, the short- and long-time behaviors can equivalently be cast in terms of a lateral correlation length $\xi(t)$, as discussed in Sec. 1.2, defined as

$$\xi(t) \sim t^{1/z}, \quad (3.6)$$

in such way that $\xi(t) \ll L (\gg L)$ for short (long) times.

The rescaled front fluctuations $\chi(\mathbf{x}, t)$, computed around the mean and normalized by the roughness, are defined as

$$\chi(\mathbf{x}, t) = \frac{h(\mathbf{x}, t) - \bar{h}(t)}{t^\beta}. \quad (3.7)$$

From this, we define the skewness s and the kurtosis k as functions of the local height fluctuation $\delta h = h(\mathbf{x}, t) - \bar{h}(t)$, namely, $s = \langle \delta h^3 \rangle_c / \langle \delta h^2 \rangle_c^{3/2}$ and $k = \langle \delta h^4 \rangle_c / \langle \delta h^2 \rangle_c^2$, where $\langle \dots \rangle_c$ denotes the cumulant average.

The study of these fluctuations is relevant in this context since the PDF of the height fluctuations is known to be another universal trait. For instance, in one-dimensional KPZ universality class it is provided by either the GOE-TW or the GUE-TW distributions, as discussed in Sec. 1.3.3.

As in equilibrium critical dynamics [10], for kinetic roughening systems scaling behavior reflects into the behavior of correlation functions. Two additional space correlation functions will be considered to describe the spatio-temporal evolution of the front, namely, the height covariance $C_1(\mathbf{r}, t)$,

$$C_1(\mathbf{r}, t) = \frac{1}{L^d} \sum_x \langle h(\mathbf{x} + \mathbf{r}, t) h(\mathbf{x}, t) \rangle - \langle \bar{h}(t) \rangle^2 \quad (3.8)$$

and the height-difference correlation function $C_2(r, t)$,

$$\begin{aligned} C_2(\mathbf{r}, t) &= \frac{1}{L^d} \sum_x \langle [h(\mathbf{x} + \mathbf{r}, t) - h(\mathbf{x}, t)]^2 \rangle \\ &= 2\langle \overline{h(t)^2} \rangle - \frac{2}{L} \sum_x \langle h(\mathbf{r} + \mathbf{x}, t) h(\mathbf{x}, t) \rangle. \end{aligned} \quad (3.9)$$

For $d > 1$, we have computed these correlations for \mathbf{r} varying in the x -direction only and averaging in the remaining $d - 1$ directions. Note that the three observables defined in this section are mathematically related. Indeed, under the assumption of rotational invariance, so that dependence on \mathbf{r} is only through $r = |\mathbf{r}|$, one has that $C_2(r, t) = 2[w^2(t) - C_1(r, t)]$ [51].

The study of the height covariance correlation function $C_1(\mathbf{r}, t)$ allows one to provide a further characterization of the two-point front statistics. As discussed in Sec. 1.3.3, the height covariance in KPZ universality class is expected to behave as a universal property of front fluctuations. For one-dimensional KPZ interfaces, it is expected to converge to the Airy process

covariance,

$$C_1(r, t) = a_1 t^{2\beta} A_i \left(a_2 r / t^{1/z} \right), \quad (3.10)$$

where $A_i(u)$ denotes the covariance of the Airy_i process, with $i = 1$ for flat interfaces and $i = 2$ for radial ones, as discussed in Sec. 1.3.3 [13, 22, 33].

The parameters a_1 and a_2 appearing in Eq. (3.10) are suitable numerical constants [85–87] which need to be estimated in order to test Eq. (3.10). The value of a_1 is given by

$$a_1 = \frac{C_1(0, t)}{t^{2/3} \text{Airy}_1(0)}. \quad (3.11)$$

One may then estimate the value of a_2 by choosing a point of the graph of the Airy_1 function, $(\tilde{x}, \text{Airy}_1(\tilde{x}))$; specifically, in our analyses we have selected $\tilde{x} = \tilde{x}_0 = 0.5$. The relation between \tilde{x} and a_2 is $\tilde{x} \equiv a_2 r / t^{2/3}$. Then, from Eq. (3.10),

$$\frac{C_1(\tilde{x}_0 t^{2/3} / a_2)}{t^{2/3}} = a_1 \text{Airy}_1(\tilde{x}_0). \quad (3.12)$$

Given the value of $C_1(\tilde{x}_0 t^{2/3} / a_2)$, a linear interpolation of data allows one to compute the value of its argument, and hence solve for a_2 .

While $C_1(\mathbf{r}, t)$ may be used for testing universal properties, $C_2(\mathbf{r}, t)$ allows us to evaluate, for example, the correlation length $\xi(t)$. Indeed, under kinetic roughening conditions, the FV dynamic scaling Ansatz implies for C_2

$$C_2(\mathbf{r}, t) = r^{2\alpha} g_{\text{FV}}(r/\xi(t)), \quad (3.13)$$

where g_{FV} is a scaling function which behaves as $g_{\text{FV}}(u) \sim u^{-2\alpha}$ for $u \gg 1$ and $g_{\text{FV}}(u) \sim \text{const}$ for $u \ll 1$ [11, 51]. In this way, for r smaller than the correlation length, it is $C_2(r, t) \sim r^{2\alpha}$ while, for r greater than the correlation length, $C_2(r, t)$ reaches a plateau $C_{2,p}(t)$ and becomes r -independent, so that

$$C_{2,p} \sim \xi^{2\alpha} \quad \text{for } r \gg \xi(t). \quad (3.14)$$

Moreover, one may evaluate the correlation length using

$$C_2(\xi_a(t), t) = a C_{2,p}(t), \quad (3.15)$$

where a is a constant, typically $a = 0.8$ or 0.9 . With this choice, the correlation length at a given time t is defined as the distance along the front

at which the correlation function C_2 takes 80% or 90% (respectively) of its plateau-value $C_2, p(t)$. We remark that the precise value of a does not modify the scaling of the correlation length.

There are kinetically rough systems in which the height-difference correlation function exhibits an anomalous behavior which does not agree with the FV form given by Eq. (3.13). When this so-called anomalous scaling exists, the FV scaling needs to be generalized into [88–90]

$$C_2(\mathbf{r}, t) = r^{2\alpha} g(r/\xi(t)), \quad (3.16)$$

where $g(u) \sim u^{-2\alpha}$ for $u \gg 1$ and $g(u) \sim u^{-2(\alpha-\alpha_{\text{loc}})}$ for $u \ll 1$. Now α_{loc} is a so-called *local roughness exponent* which characterizes the front fluctuations measured at distances smaller than the system size L . Under FV scaling, the two roughness exponents are equal [11, 51], $\alpha = \alpha_{\text{loc}}$, so that $g(u) = g_{\text{FV}}(u)$ and Eq. (3.16) coincides with Eq. (3.13). However, there are cases in which $\alpha_{\text{loc}} \neq \alpha$, so that front fluctuations at small and large distances are characterized by two independent roughness exponents. In these cases, $C_2(\mathbf{r}, t)$ curves obtained for different times displace systematically with time and do not overlap at small r ; this a landmark behavior of anomalous scaling.

Anomalous scaling may be originated by different causes [88, 91]. One of them is superroughening, which takes place when the global roughness exponent α is larger than or equal to one. Another case is when an independent exponent scaling α_{loc} exists and induces different scaling properties for small and large length scales; these systems are said to display intrinsic anomalous kinetic roughening [89–91].

Anomalous scaling can also be characterized efficiently [88] through the front structure factor $S(\mathbf{k}, t)$, defined as

$$S(\mathbf{k}, t) = \langle |\mathcal{F}[h(\mathbf{x}, t)]|^2 \rangle, \quad (3.17)$$

where \mathcal{F} denotes the space Fourier transform and \mathbf{k} is a d -dimensional wave vector. For isotropic systems displaying intrinsic anomalous scaling, $S(\mathbf{k}, t)$ behaves as [88]

$$S(k, t) = k^{-(2\alpha+d)} s(kt^{1/z}), \quad (3.18)$$

where $s(y) \propto y^{2(\alpha-\alpha_{\text{loc}})}$ for $y \gg 1$, $s(y) \propto y^{2\alpha+d}$ for $y \ll 1$, and $k = |\mathbf{k}|$. Analogously to the case of the height-difference correlation function, Eq. (3.18)

generalizes the FV Ansatz for the structure factor [11, 51], which is retrieved for $\alpha_{\text{loc}} = \alpha$. In presence of intrinsic anomalous scaling (and not for super-roughening), two main implications of Eq. (3.18) should be stressed:

- (i) For large $k \gg t^{-1/z}$, the scaling of the structure factor with k reveals the local roughness exponent, namely,

$$S(k) \sim k^{-(2\alpha_{\text{loc}}+d)}. \quad (3.19)$$

- (ii) The $S(k, t)$ curves as functions of k do not overlap for different times.

3.2 Calculation of uncertainty

In this section we describe the methodology employed for statistical data analysis. We have computed the statistical error on different observables for highly-correlated raw numerical data. The methodology for error estimation will be described below. Additional details may be found elsewhere [92–95]. It has been our practice to denote the estimated uncertainty in the last digit(s) by enclosing the numbers in round brackets. These error bars are represented in the graphics, but they may be challenging to see in numerous instances.

To study statistically a system several trials, or runs, are performed. As particles are created randomly, times between runs are not the same. To compare a magnitude, from runs at different times, we define temporal boxes with a width Δt , in which we include points from different simulations corresponding to any time $t \in (t, t + \Delta t)$. We define then the best estimate of a magnitude x in the temporal box $(t, t + \Delta t)$ of the i -th run as the simple mean of the all the points therein, namely,

$$\hat{x}_i = \frac{1}{n} \sum_{j=1}^n x_j, \quad (3.20)$$

where n is the number of points included in the box. The mean, \bar{x} , is in turn given by

$$\bar{x}_i = \frac{1}{N} \sum_{i=1}^N \hat{x}_i, \quad (3.21)$$

where N is the number of runs (that is, number of initial conditions).

As a general rule, the errors for all the results reported in next sections have been calculated with the jackknife (JK) procedure [96, 97]. The i -th jackknife estimate of a magnitude x is the average over all runs, but omitting the data for the i -th run:

$$x_i^{\text{JK}} = \frac{1}{N-1} \sum_{k=1, k \neq i}^N \hat{x}_k. \quad (3.22)$$

The variance of \bar{x} is then defined as

$$\sigma_{\text{JK}}(\bar{x}) = \frac{N-1}{N} \sum_{k=1}^N (\bar{x} - x_i^{\text{JK}})^2. \quad (3.23)$$

Hence, for each temporal box we have the estimate $\bar{x} \pm \sqrt{\sigma_{\text{JK}}}$ (to within one standard deviation). Note that for a given set of x_i , the standard error formula and Eq. (3.23) are identical. In this scenario, the jackknife powers is utilized due to nonlinear dependencies between the variables.

Normally, to determine a given critical exponent one needs to fit data to a power-law. It is important to realize that data show a huge correlation (e.g., the $\xi \sim t^{1/z}$ data are highly correlated among them). Hence, one should strictly use the full covariance matrix to perform the global fit in order to compute a given exponent using the least-square fit. The problem arises because, in general, the full covariance matrix is singular or almost singular (i.e., its determinant is close to zero) [92–95], which prevents the computation of the inverse matrix required for the fitting procedure. In order to circumvent this problem, we have used the following procedure, which takes into account the statistical correlation of the data and has demonstrated its excellent performance, for instance, in the study of spin glasses and in the computation of the hadron masses in lattice QCD [92–94]:

1. The mean value, \bar{z} , of a given exponent (e.g., z) is computed using data from all the runs using the diagonal covariance matrix of the data.
2. The statistical error for this exponent is computed using the jackknife procedure. One removes the i -th run from the data and computes the i -th value, z_i^{JK} , associated to this jackknife block, using again its diagonal covariance matrix. The error is then computed using the

standard equation in the jackknife procedure, namely,

$$\sigma_{\text{JK}}(\bar{z}) = \frac{N-1}{N} \sum_{k=1}^N (\bar{z} - z_i^{\text{JK}})^2. \quad (3.24)$$

Note that, if one uses only the diagonal covariance matrix, the statistical error of the exponent is strongly underestimated. With the aforementioned procedure, we take into account the strong correlations among the data, and provide the exponent with the right statistical error.

Finally, note that we have chosen the intervals of all the fits in order to obtain a reduced χ^2 (χ^2 divided by degrees of freedom, where degrees of freedom is the number of datapoints minus the number of parameters being fitted) near to one, where χ^2 has been computed assuming a diagonal covariance matrix [96]. It is an indication that the weighted sum of squared deviations between the fitted function and the data points is the same as that expected for a random sample from a population characterized by the function with the current value of the parameters and the given standard deviations.

The so-called p -value or the quality of the fit Q^1 [96] has also been taken into account in the choice of intervals, always considering $p > 0.05$.

¹It is the probability to have a value greater than the resulting value of χ^2 occurring by random chance, i.e. one minus the cumulative distribution function of the χ^2 -distribution for the number of degrees of freedom and the resulting χ^2 .

Chapter 4

Reaction-diffusion fronts

The work presented in this chapter has been published as B. G. Barreales, J. J. Meléndez, R. Cuerno, and J. J. Ruiz-Lorenzo, J. Stat. Mech., 023203 (2020).

In this chapter, we study the dynamics of fronts in the discrete $A + A \leftrightarrow A$ reaction-diffusion system, which can be described in continuous form by the (stochastic) Fisher-Kolmogorov-Petrovsky-Piscunov equation. Our study focuses on the two-dimensional version of the discrete model, using extensive numerical simulations and an improved analysis of the interface between stable and unstable phases over time. We determine the critical exponents that govern the spatio-temporal fluctuations of the front, with a particular emphasis on the front width and correlation length. These exponents match those obtained in a previous study [98], and are consistent with the KPZ universality class for one-dimensional interfaces. Additionally, we explore one-point statistics and the covariance of rescaled front fluctuations, which had not been investigated previously, thus providing further evidence for KPZ universality.

4.1 Introduction

Reaction-diffusion systems are a unique setting for studying collective behavior and nonlinear properties using statistical mechanics [99]. The most common example of these systems is the change in space and time of the

concentration of one or more chemical substances, which happens when substances change into other forms through reactions spreading in space through diffusion [100]. Reaction-diffusion systems have been observed in various experimental contexts in addition to chemical reactions, including developmental biology [101], epidemic processes in complex networks [102], and reactive turbulence [103], among others. In the history of the field, the Fisher-Kolmogorov-Petrovsky-Piscunov (FKPP) equation [104, 105] has been instrumental in advancing our understanding of this type of systems. The FKPP equation for a non-negative scalar field $\rho(\mathbf{r}, t)$ is

$$\frac{\partial \rho(\mathbf{r}, t)}{\partial t} = D \nabla^2 \rho(\mathbf{r}, t) + R \rho(\mathbf{r}, t) - \frac{R}{K} \rho(\mathbf{r}, t)^2. \quad (4.1)$$

When this equation is used to describe the propagation of a population in a medium, for instance, $\rho(\mathbf{r}, t)$ is the population density, D is the diffusion coefficient (which represents the population capacity to disperse in the medium), R is the intrinsic growth rate of the population, and K is the carrying capacity of the medium (which represents the maximum population density that the environment can sustain without exhausting available resources).

An example where the FKPP equation can be applied is the study of the spread of an invasive species in an ecosystem. Let us suppose that an invasive plant species has been introduced into an island and is expanding in its territory. The population growth rate of the plant is high, and it spreads out easily due to the lack of natural predators on the island. One can model the expansion of this population using the FKPP equation. In this case, the variable $\rho(\mathbf{r}, t)$ would represent the density of the population of the invasive plant at each location \mathbf{r} of the island and at each time t . The equation would take into account population diffusion $D \nabla^2 \rho(\mathbf{r}, t)$, meaning that the plants can disperse to nearby regions. It would also consider the population growth rate $R \rho(\mathbf{r}, t) \left(1 - \frac{\rho(\mathbf{r}, t)}{K}\right)$, where the term R reflects the plant reproduction rate, and the term $\left(1 - \frac{\rho(\mathbf{r}, t)}{K}\right)$ limits growth as the population approaches the carrying capacity K of the ecosystem. It is essential to note that the FKPP model is a simplification of reality and does not account for many complex factors that can influence the spread of an invasive species, such as interactions with other species, environmental changes, and stochastic factors. Still, it provides a useful framework for understanding general aspects of population spread dynamics.

Our focus here will be on the fact that Eq. (4.1) describes the propagation of a front of dimension d ; thus, $\mathbf{r} = (\mathbf{r}_{\parallel}, r_{\perp}) \in \mathbb{R}^{d+1}$, where $r_{\perp} \in \mathbb{R}$ represents the growth direction and $\mathbf{r}_{\parallel} \in \mathbb{R}^d$ represents the position on the substrate. For initially segregated conditions $\rho(\mathbf{r}, t = 0) = \rho_{\text{eq}}$ for $r_{\perp} \leq 0$ and $\rho(\mathbf{r}, t = 0) = 0$ for $r_{\perp} > 0$, Eq. (4.1) describes the propagation of a front $h(\mathbf{r}_{\parallel}, t)$ along the r_{\perp} coordinate, separating a stable phase ($\rho = 1$) which invades an unstable one ($\rho = 0$) [106, 107]. Once again, there are many examples: the behavior of DNA reaction networks [108], colloidal systems [109, 110], the propagation of diseases throughout populations [111], or the dynamics of invasions among human populations [112].

In any case, the FKPP equation provides a mean-field description of the invasion process. In general, it is important to investigate the impact of stochastic fluctuations, such as those in population density. These fluctuations not only modify quantitatively system properties, such as the average front velocity [113, 114], but may also give rise to new phenomena not accounted for by mean-field approximations [10, 113]. In some cases, fluctuations may even dominate the large-scale behavior of the system [10, 115]. To account for fluctuations, one can use more microscopic, discrete models [62] that are consistent with the front dynamics described by Eq. (4.1) [62, 116], but which allow for a more explicit assessment of the role of external or internal noise. Thus, for instance, the $A + A \leftrightarrow A$ reaction-diffusion model [117] has been shown [118, 119] to implement a stochastic generalization of Eq. (4.1), being specifically described at a mesoscopic level by the so-called stochastic FKPP (sFKPP) equation,

$$\partial_t \rho = D \nabla^2 \rho + \rho - \rho^2 + \sqrt{\rho(1-\rho)/N} \eta(\mathbf{r}, t), \quad (4.2)$$

where $\eta(\mathbf{r}, t)$ denotes zero-average, uncorrelated Gaussian white noise of unit variance, and N is the number of particles in the system. Equation (4.2) indeed recovers Eq. (4.1) in the macroscopic $N \rightarrow \infty$ limit; for simplicity we have considered $R = K = 1$. It should be noted that there are other microscopic models available that might lead to probabilistic generalizations that differ from Eq. (4.2), but still have Eq. (4.1) as a macroscopic (or mean-field) approximation. An example of such a model is directed percolation [see Sec. 2.3 and specifically Eq. (2.13)], which has been widely studied [61, 120].

The $A + A \leftrightarrow A$ system is actually a case in which the hydrodynamic

behavior is dominated by fluctuations. Indeed, the advancing front displays kinetic roughening [11, 51], namely scale-invariant fluctuations characterized by critical exponents (see Chapter 1), which have been systematically studied [98, 121–124]. The main conclusion [98, 124], confirmed by recent work on the sFKPP equation [115], is that the fluctuations of d -dimensional fronts in the ($d + 1$ -dimensional) $A + A \leftrightarrow A$ system are in the KPZ universality class of kinetically rough d -dimensional interfaces.

Recently, there has been considerable focus on exploring the various characteristics of 1D KPZ universality in systems involving interacting particles [12, 13, 22, 125], as well as growth models such as Eden or ballistic deposition [13, 22]. However, the investigation of reaction-diffusion systems from the same perspective has received relatively less attention. For the $A + A \leftrightarrow A$ system, early numerical investigations [121] revealed kinetic roughening behavior in the dynamics of the front. Surprisingly, the critical exponents obtained did not align with the KPZ values. Later studies [122] also produced non-KPZ exponents, which were interpreted as potential evidence that d -noisy pulled fronts [107] could fall in the universality class of the KPZ equation for interfaces in ($d + 1$) dimensions [123]. In turn, a more thorough analysis of numerical simulations for the $A + A \leftrightarrow A$ model [98] clarified the situation as being conditioned by the specific method employed for the measurement of the critical exponents, and unequivocally demonstrated that the relevant universality class for kinetic roughening was indeed that of the KPZ equation for d -dimensional interfaces, in terms of critical exponents. Although space-related critical exponent values were well-characterized, those related to time remained less explored for the discrete model. Yet, recent research on the sFKPP equation and related continuum systems [115, 120, 124] has solidified the consensus on the significance of KPZ scaling for this category of reaction-diffusion systems. Note that, however, knowledge of critical exponents may not suffice to identify the universality class in kinetic roughening: examples are known in which a linear system (hence, with non-TW point statistics) shares the same critical exponent values as the nonlinear 1D KPZ equation, which paradigmatically displays TW one-point fluctuations [126].

From a more general point of view, it is quite interesting to characterize these fluctuations that can probably be found within the broad class of physical and biological systems which are described at a mean-field level by the

FKPP Eq. (4.1). Recent advances in (bio)materials science enable the design and control of materials at the submicron and nanoscale [127] through, for example, DNA circuits based on reaction-diffusion systems [128, 129]. Working at such small scales, it is important to assess the potential quantitative and qualitative influence of external and internal noise in the relevant reaction-diffusion processes and systems. The $A + A \leftrightarrow A$ model is a prime example of cases where microscopic fluctuations can have macroscopic implications [115]. Interestingly, and staying within the KPZ-related interacting particle systems, we recall that the paradigmatic asymmetric simple exclusion process (ASEP) model was historically proposed in the 1960s as a simplified description of the dynamics of ribosomes translating along a messenger RNA molecule [130]. Recent results on 1D KPZ statistics [13, 22] elucidate the emergence of fluctuation properties in biophysics and cell biology at the level of a few molecules.

4.2 Model and simulation details

We study front propagation and fluctuations for $d = 1$. Hence, we consider a $L_x \times L_y$ lattice, with the front advancing along the OY direction; in the notation introduced in Eq. (4.1), $\mathbf{r} = (r_{\parallel}, r_{\perp}) \equiv (x, y)$. At $t = 0$, each point of the lattice is either unoccupied or occupied by a particle with a probability equal to the equilibrium density $\rho_{eq} = \mu/(1 + \mu)$ (see Appendix C) [98, 121], so that the initial configuration consists of a number of particles which are uniformly distributed within a region of area $L_x \times L_{y,0}$, where $L_{y,0} \ll L_y$. In general, periodic boundary conditions (PBC) are assumed along the x coordinate, but in special cases helical boundary conditions (HBC) have been used.

The time evolution of the particles is ruled by reaction (birth or death) and diffusion. Each time step, a particle is chosen randomly. Then, one of the nearest neighbor sites of that particle is selected with equal probability, $D = 1/4$ (since the lattice is two-dimensional). If the selected adjacent site is unoccupied, then either a new particle is created at the adjacent site with probability μ , or the particle moves towards it. If the adjacent site is occupied, on the other hand, then the chosen particle is removed, and the particle at the adjacent site remains. According to this, the parame-

ter μ describing the probability of creating a particle is the birth rate for the process. The transcription of these microscopic rules in the form of a FKPP equation, for a continuum description of the system, is developed in Appendix C.

At each time, a local density is defined for the lattice as

$$\rho_l(\mathbf{r}, t) = \sum_{\langle \mathbf{s}, \mathbf{r} \rangle} n(\mathbf{s}, t), \quad (4.3)$$

where $n(\mathbf{s}, t)$ stands for the occupation of the \mathbf{s} -th site at time t , and the sum spans over all the nearest neighbors ($\langle \mathbf{s}, \mathbf{r} \rangle$) of site \mathbf{r} . Given $\rho_l(\mathbf{r}, t)$, the front position $h(x, t)$ is defined as the maximum y -coordinate for sites $\mathbf{r} = (x, y)$ such that $\rho_l(\mathbf{r}, t) > \rho_{eq}/2$ for the given value of x and t . Alternative related definitions may be employed (see Ref. [98]) without relevant changes in the results.

Once the local heights $h(x, t)$ have been defined, the computed observables are those mentioned in Sec. 3.1. As an illustration of the model, Fig. 4.1 and Fig. 4.2, plot snapshots of configurations of particles; the front is highlighted in each case.

Tables 4.1 (for PBC) and 4.2 (for HBC) collect all the simulation conditions considered herein. Note that the time step in each simulation is taken as the value required for all the particles to have the chance to diffuse. Hence $\delta t = 1/N(t)$, where $N(t)$ is the total number of particles at time t .

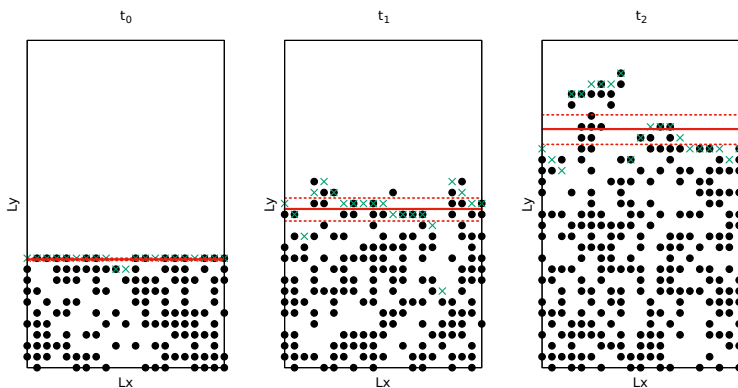


Figure 4.1: Schema of the reaction-diffusion model. Green crosses denote the position of the front $h(x, t)$, the red line highlights the mean front $\bar{h}(t)$ and the dashed red lines represent the front width $w(t)$, that grows with time.

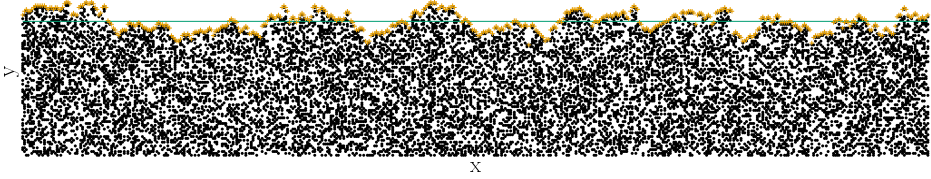


Figure 4.2: Snapshot of a $L_x = 500$ system for $\mu = 0.5$ and a fixed value of t . The front $h(x, t)$ is plotted as orange crosses and $\bar{h}(t)$ appears as a green line

Table 4.1: Parameter for simulations reported herein where periodic boundary conditions have been used. L_x and L_y are the dimensions of the simulation lattice, while $L_{y,0}$ indicates the size along the y -direction of the region in which particles are homogeneously distributed at $t = 0$, and t_{\max} is the maximum time reached in the simulations. The last column shows the number of runs performed in each case.

L_x	L_y	$L_{y,0}$	μ	t_{\max}	runs
250	1000	250	0.1	7.5×10^6	104
			0.3	7.5×10^6	100
			0.5	7.5×10^6	1600
500	500	125	0.01	1.1×10^4	100
			0.025	5.8×10^3	100
			0.05	3.8×10^3	100
			0.1	2.6×10^3	100
			0.2	1.9×10^3	100
			0.3	1.5×10^3	100
			0.4	1.2×10^3	100
0.5	6.0×10^2	1600			
512	512	128	0.5	9.3×10^2	2002
1000	1000	250	0.01	2.0×10^4	100
			0.025	1.0×10^4	100
			0.05	7.8×10^3	100
			0.1	5.4×10^3	100
			0.2	3.7×10^3	100
			0.3	2.8×10^3	100
			0.4	2.5×10^3	100
0.5	2.0×10^3	100			

Table 4.2: Parameter for simulations employing helical boundary conditions with an overall slope m . Parameters L_x , L_y and t_{\max} are as in Table 4.1. The initial configurations occupy a trapezoidal area with $L_{y,0}$ and $L_{y,0} + mL_x$ heights. The last column shows the number of runs performed.

L_x	L_y	$L_{y,0}$	μ	m	t_{\max}	runs
500	2000	125	0.1	0	1.8×10^3	200
				0.1	1.8×10^3	
				0.2	1.7×10^3	
				0.3	1.6×10^3	
			0.5	0	6.0×10^2	
				0.1	5.6×10^2	
				0.2	5.2×10^2	
				0.3	4.8×10^2	

4.3 Results

4.3.1 Front velocity

The mean front position was computed as a function of time for two different system sizes, namely, $L_x = L_y = 500$ and $L_x = L_y = 1000$, using $L_{y,0} = L_y/4$ in both cases. We observed that, for all values of μ , the mean front position grows linearly with time, regardless of the values of L_x and L_y , namely

$$\langle \bar{h}(t) \rangle = vt + h_0. \quad (4.4)$$

The slope v in Eq. (4.4) is taken as the front velocity, and it is plotted in Fig. 4.3 as a function of μ . Within the mean-field approximation [Eq. (4.1)], v is related to μ as

$$v = 2D\mu^{1/2}, \quad (4.5)$$

where D is the diffusion coefficient ($D = 1/4$ in our case). Data from Fig. 4.3 display the same behavior, i.e., $v \approx 0.5\mu^{0.5}$ for $\mu \geq 0.05$, consistent with previous findings [98].

An important issue for the subsequent discussion is to investigate the relevance of the nonlinear term $(\lambda/2)(\nabla h)^2$ in Eq. (1.14) for the continuum

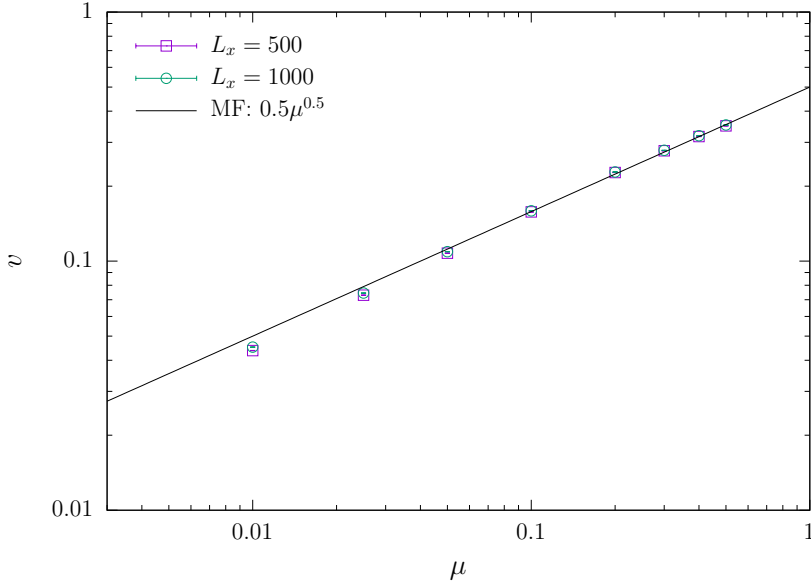


Figure 4.3: Front velocity v as a function of μ for two different system sizes; error bars are smaller than the symbol sizes. The straight line represents the mean-field prediction, which contains no free parameters.

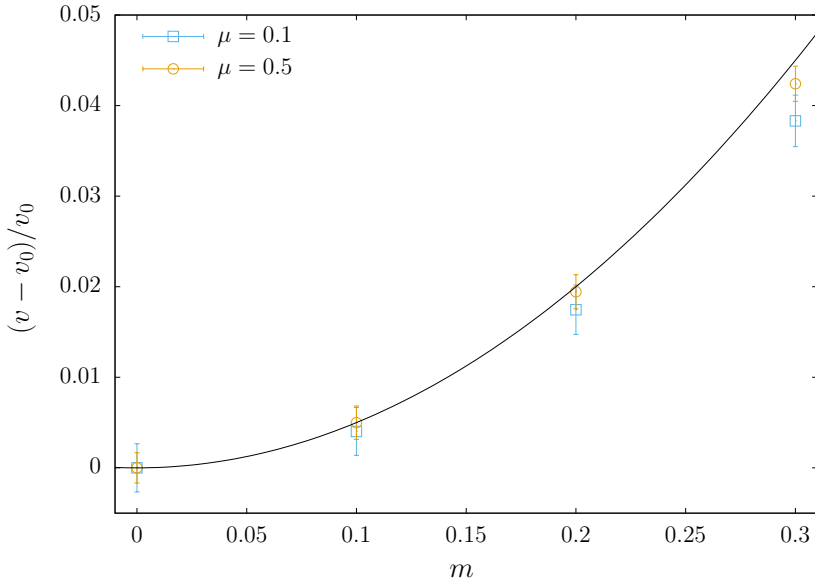


Figure 4.4: Normalized front velocity $(v - v_0)/v_0$ as a function of the average tilt m imposed by helical boundary conditions, where $v_0 = v(m = 0)$, for a system size of $L_x = 500$ and two different μ values. The solid line corresponds to the $m^2/2$ parabolic prediction, which has no free parameters.

description of our discrete model. To this end, we proceed as described in Appendix B: we implemented helical boundary conditions such that $x(L+1) = x(1) - (L+1)m$, and measured the resulting front velocity as a function of the average slope m . This tilt modifies the front velocity as Eq. (B.5). Displayed in Fig. 4.4, our results demonstrate a parabolic dependence of v on m . For $\mu = 0.1$ and $\mu = 0.5$, we found $\lambda = 0.1580(3)$ and $\lambda = 0.3481(4)$, respectively.

4.3.2 Front roughness: exponent β

Previous research on kinetic roughening in the $A + A \leftrightarrow A$ model has reported values of $\beta = 0.27(1)$ and $\alpha = 0.41(2)$ [98, 121]. Although these are similar to the exact values for the KPZ universality class of one-dimensional interfaces, they are not identical to them. This discrepancy between theoretical and computed values has been attributed [98] to the imprecise definition of the interface for small μ . In fact, the front position is defined using the local density, as in Eq. (4.3). When μ is small, there are generally only a few particles surrounding an occupied site, which can result into an underestimation of $\rho_l(\mathbf{r})$ and, consequently, influence the position and width of the interface.

The validity of this interpretation is supported by the results presented in Fig. 4.5, which displays the squared front roughness $w^2(t)$, Eq. (3.2), as a function of time t for $L_x = L_y = 500$ and various values of the birth rate μ . As shown in Fig. 4.5, the growth exponent β , Eq. (3.4), for fixed $L_x = L_y$ is highly dependent on the value of μ , approaching the KPZ limit for $\mu \simeq 0.5$. As expected, the apparent effective value of β , which characterizes the $w^2(t) \sim t^{2\beta}$ power-law behavior for each dataset, decreases as time increases. This is an indication of eventual saturation to the steady-state roughness value due to the finite size of the simulated systems [11, 51]. It is remarkable that $w^2(t, \mu)$ is a decreasing function of μ , due to the saturation of the front roughness.

The dependence of β with the system size is demonstrated in Table 4.3. The data indicate a clear trend towards the KPZ value of $\beta_{\text{KPZ}} = 1/3$ as L_x and μ increase. Our findings thus confirm that the theoretical KPZ behavior is systematically reached as μ and L_x increase. For smaller μ and L_x , on the contrary, the exponent values are close to $\beta = 1/4$, which is the

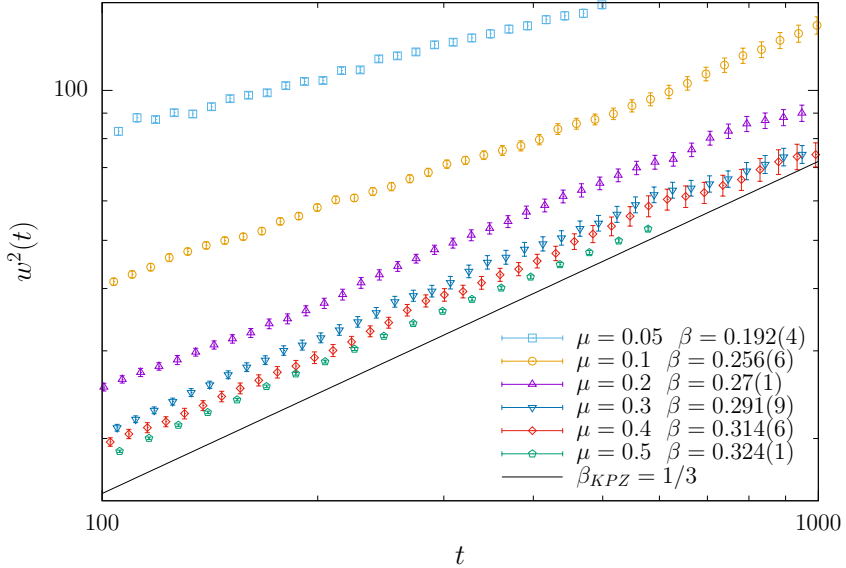


Figure 4.5: Front roughness $w^2(t)$ as a function of time for various values of μ , computed for a system size of $L_x = L_y = 500$. The legend indicates the values of β , obtained as discussed in the main text. The solid black line corresponds to the KPZ scaling, $w^2(t) \sim t^{2\beta_{\text{KPZ}}} = t^{2/3}$.

exact value corresponding to the EW equation [Eq. (1.10)], also known as the linearized ($\lambda = 0$) KPZ equation. The EW equation often provides preasymptotic behavior in the context of KPZ scaling [11, 51]. As a reference, and unless explicitly stated otherwise, all our numerical simulations are hereafter performed with $\mu = 0.5$ and $L_x = 500$, based on the results of these numerical simulations.

Table 4.3: Growth exponent β for different values of μ and L_x .

	$\mu = 0.1$	$\mu = 0.3$	$\mu = 0.5$
$L_x = 250$	0.230(7)	0.294(6)	0.314(4)
$L_x = 500$	0.256(6)	0.291(9)	0.324(5)
$L_x = 1000$	0.28(1)	0.305(4)	0.320(4)

4.3.3 Front correlation length: exponents z and α

In Sec. 3.1 it was mentioned that the correlation length $\xi(t)$ at a specific time t can be computed by identifying the plateau of the $C_2(r, t)$ curves at sufficiently large distances r . For the reaction-diffusion model studied herein, we computed for this purpose the values $\xi_{0.8}$ and $\xi_{0.9}$, defined as the distances r where $C_2(r, t)$ reaches $0.8C_{2,p}(t)$ and $0.9C_{2,p}(t)$, respectively, where $C_{2,p}$ denotes the plateau at time t , defined as

$$C_{2,p}(t) = C_2(L_x/2, t). \quad (4.6)$$

The estimated values for the correlation length are plotted against time in Fig. 4.6. By fitting these estimates of $\xi_{0.9}$ and $\xi_{0.8}$ to Eq. (3.6) over the time range $t \in [20, 600]$, we obtain $1/z = 0.673(9)$ and $1/z = 0.676(7)$, respectively. Both of these values are consistent, within the error bars, and agree with the exact value of $1/z_{\text{KPZ}} = 2/3$ for the 1D KPZ universality class. This is actually the first direct measurement of the dynamic exponent for the $A + A \leftrightarrow A$ model, to the best of our knowledge.

The roughness exponent can also be determined from the height-difference correlation function according to Eq. (3.14), as seen in Sec. 3.1. In Fig. 4.7 we have plotted $C_{2,p}$ versus $\xi_{0.8}(t)$ and $\xi_{0.9}(t)$; the slopes provide $2\alpha = 0.994(6)$ for $\xi_{0.8}$ and $2\alpha = 0.99(1)$ for $\xi_{0.9}$, where our best fits were over the time ranges $t \in [14, 600]$ and $t \in [20, 600]$, respectively. Both results are consistent with the exponent α for the 1D KPZ universality class: $2\alpha_{\text{KPZ}} = 1$.

Finally, the height-difference correlation function $C_2(r, t)$ is shown in Fig. 4.8. As a test of Eq. (3.13), in Fig. 4.9 we have represented $C_2(r, t)/r^{2\alpha}$ against $r/\xi_{0.9}$, assuming $\alpha = 0.5$. We found a time-independent universal function that approximates g_{FV} in Eq. (3.13); both the quality of the collapse and the agreement with the expected universal behavior of the scaling function are better for large values of $(r/\xi(t))$.

4.3.4 PDF of front fluctuations

As discussed in Sec. 1.3.3, one of the characteristics of the KPZ universality class is the one-point statistics of the field fluctuations [12, 22]. In the case of 1D interfaces with PBC, the probability density function (PDF) of the

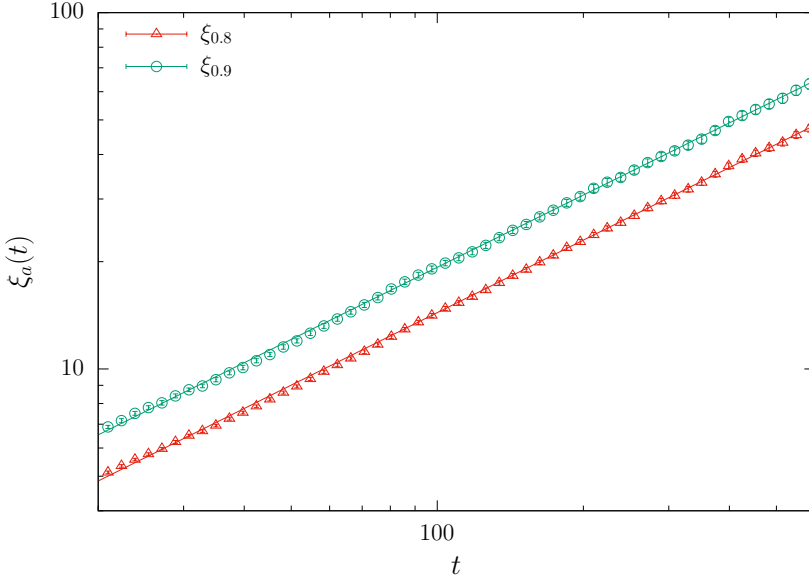


Figure 4.6: Estimated $\xi_{0.8}(t)$ and $\xi_{0.9}(t)$ vs. t computed from C_2 (symbols). The lines represent the best fits of the simulation data.

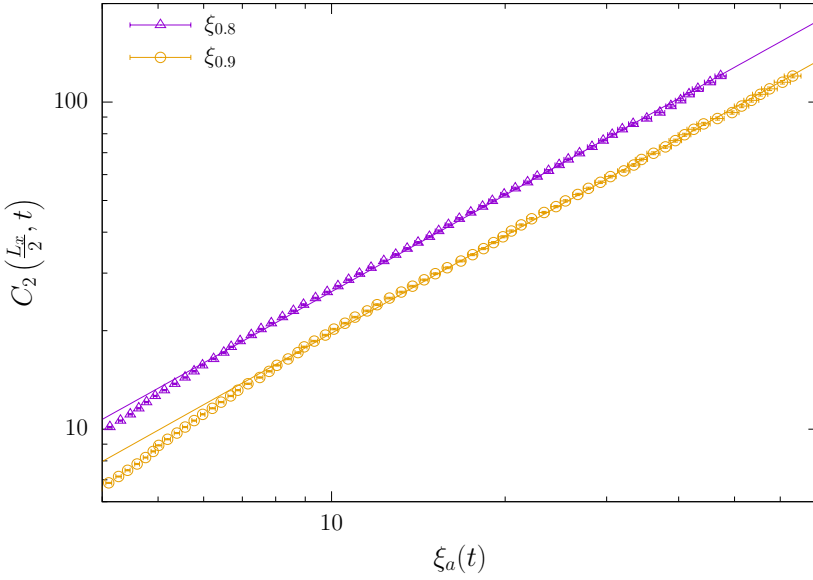


Figure 4.7: Height-difference correlation function $C_2(L_x/2, t)$ plotted as a function of $\xi_{0.8}(t)$ and $\xi_{0.9}(t)$ for various times. The lines represent the best fits of the numerical values obtained in our simulations.

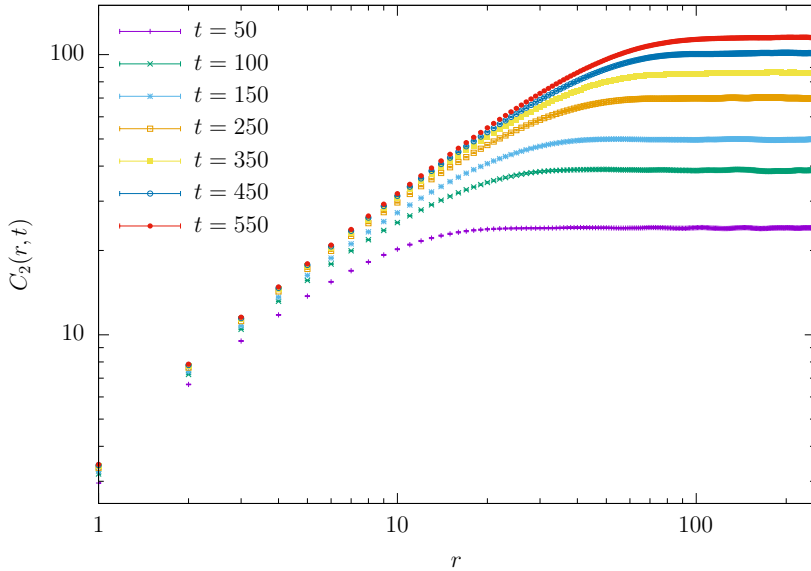


Figure 4.8: Height-difference correlation function $C_2(r, t)$ plotted as a function of r for various values of time as indicated in the legend.

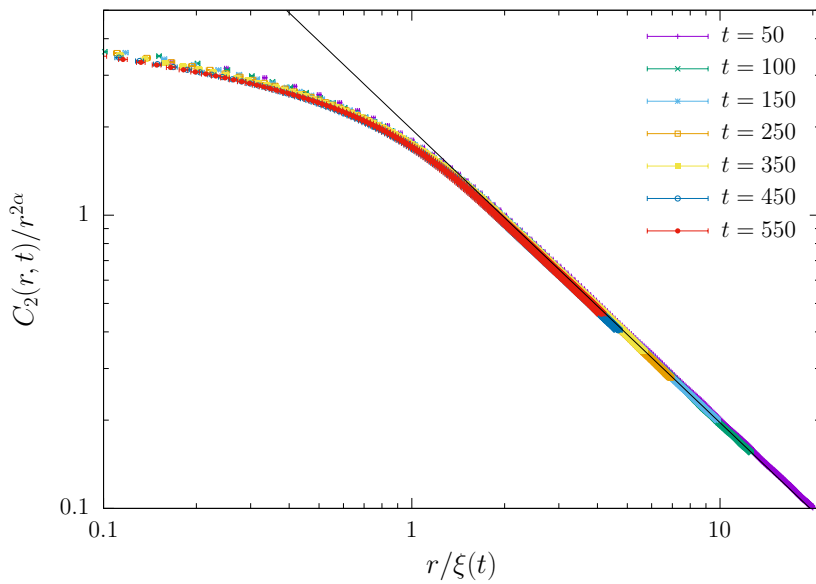


Figure 4.9: Data collapse of the height-difference correlation function, assuming $\alpha = 1/2 = \alpha_{\text{KPZ}}$. The master curve onto which the collapse occurs is the function $g(r/\xi(t))$ of Eq. (3.13), with the solid black line representing the theoretical behavior for large u , $g_{\text{KPZ}}(u) \sim u^{-2\alpha_{\text{KPZ}}} = u^{-1}$.

rescaled front fluctuations, given by Eq. (3.7), is expected to follow the GOE-TW distribution [12, 22].

Figure 4.10 illustrates the PDF of the rescaled front fluctuations computed for $L_x = 250$ and $L_x = 500$, $\mu = 0.5$, and $t \ll L_x^z$ (that is, prior to front saturation to a steady state), along with the exact GOE-TW distribution (solid line). The skewness s and kurtosis k have been computed for the numerical distributions, resulting in $s = 0.22(1)$, $k = 0.16(2)$ for $L_x = 250$ and $s = 0.25(1)$, $k = 0.17(3)$ for $L_x = 500$. The values for the GOE-TW PDF, on the other hand, are $s = 0.29346452408$ and $k = 0.1652429384$ [131]. It is apparent that our data show better agreement with the theoretical expectations for larger L_x , indicating that the small differences between the exact GOE-TW values and our numerical results can be attributed to the finite size of our simulated systems.

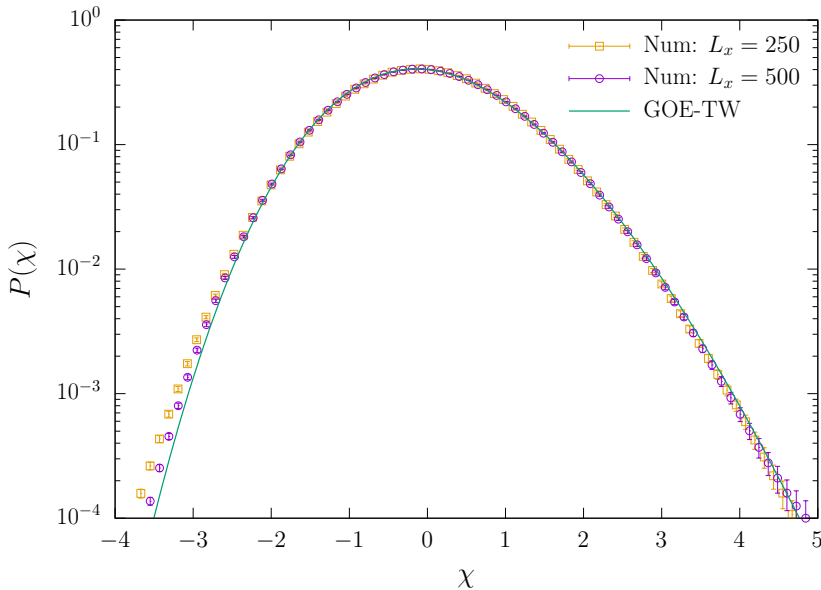


Figure 4.10: Histograms of the front fluctuations for varying L_x . The solid line represents the theoretical prediction of GOE-TW. The time interval for $L_x = 250$ is chosen as $t \in [10, 300]$, while for $L_x = 500$ it is $t \in [120, 600]$.

4.3.5 Front covariance

As already mentioned (see Sec. 1.3.3), universal behavior in the 1D KPZ equation occurs for additional magnitudes [13, 22], such as the full space-time behavior of the height covariance $C_1(r, t)$, Eq. (3.8). Indeed, under PBC, this function appropriately rescaled is expected to converge to the Airy_1 process covariance [Eq. (3.10)] [13, 22, 33]. In order to test this result, we have estimated the numerical constants a_1 and a_2 , as explained in Sec. 3.1 [see Eqs. (3.11) and (3.12)]. Specifically, we have obtained $a_1 = 2.15$ and $a_2 = 0.74$ for a system with $L_x = L_y = 512$. The rescaled C_1 together with the Airy_1 covariance are shown in Fig. 4.11, which shows a very good scaling plot.

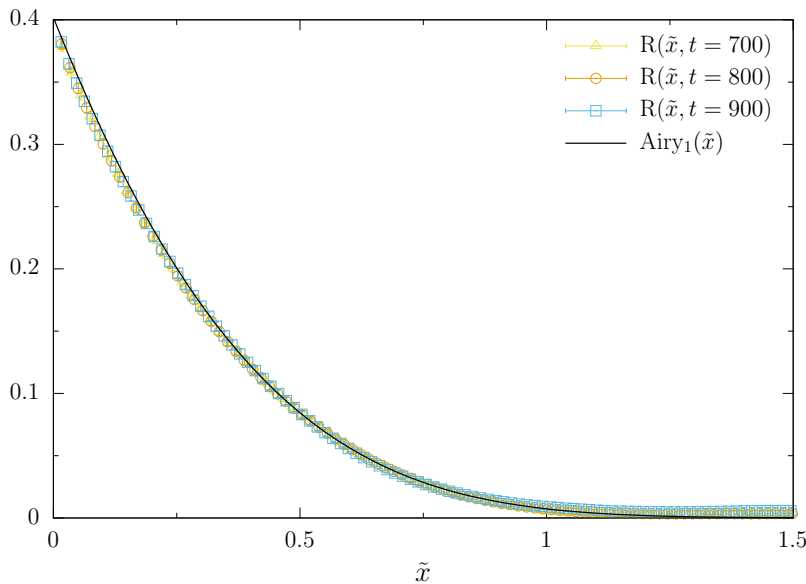


Figure 4.11: Rescaled $C_1(r, t)$ for $t = 700, 800,$ and 900 on a system with $L_x = L_y = 512$. Specifically, we denote $R(\tilde{x}, t)$ as $C_1(\tilde{x}t^{2/3}/a_2)/(a_1t^{2/3})$ with $a_1 = 2.15$ and $a_2 = 0.74$. The solid line represents the $\text{Airy}_1(\tilde{x})$ function. To enhance clarity, only every second point is shown in the figure.

4.4 Conclusions

We have revisited the 2D $A + A \leftrightarrow A$ reaction-diffusion model via numerical simulations in order to fully characterize the kinetic roughening dynamics of the evolving front within the context of the 1D KPZ universality class. Beyond confirming space-related [98, 115] and time-related [115] exponent values (note that results in Ref. [115] are for the sFKPP equation), we address the one and two-point statistics of field fluctuations as a further stringent test of KPZ universality, proving consistent behavior with the appropriate Airy_1 process. This fully settles the universality class of the 2D $A + A \leftrightarrow A$ model with respect to the kinetic roughening properties of the front dynamics.

In the context of 1D KPZ-class systems, it is noteworthy that the dynamical behavior exhibits a quite remarkable level of complexity. This complexity is characterized by a range of intriguing additional properties, such as ergodicity loss and aging, non-trivial persistence, peculiar fluctuation properties around steady state, etc. [13, 22]. These distinctive properties certainly justify a more comprehensive investigation in future studies focusing on the same type reaction-diffusion systems we have addressed in this study.

We have computed the complete set of critical exponents: β , α , and z . In particular, we provide the first direct measurement of the dynamic exponent (through the correlation length) for this model, to the best of our knowledge. The values are in agreement with those of the 1D KPZ universality class.

In addition to the exponents, we have considered one- and two-point statistics as the main traits characterizing the universality class. Indeed, the identification of surface kinetic roughening universality classes, incorporating additional properties beyond exponent values, is gaining significance due to the presence of potential ambiguities [126] and, more generally, because it enables us to better understand scale invariance in far-from-equilibrium contexts [87, 132, 133]. The one-point function (i.e., the PDF of the rescaled front fluctuation) is consistent with the GOE-TW distribution that characterizes the 1D KPZ in flat interfaces. The height covariance, which measures the two-point statistics, scales in agreement with the covariance of the Airy_1

process, which is the expected behavior in the 1D KPZ class.

As discussed in the introduction, our study characterizes a peculiar type of fluctuations which are described at the mean-field level by the FKPP equation [Eq. (4.2)] and which can therefore emerge in numerous and interesting systems: biological, physical, etc.

In conclusion, this work highlights this class of reaction-diffusion systems as an alternative context for KPZ behavior in terms of potential new experimental realizations, or as a novel point of view on open challenges, such as the properties of this wide universality class in higher dimensions [22].

Chapter 5

Coffee-ring fronts

This thesis chapter originally appeared in the literature as B. G. Barreales, J. J. Meléndez, R. Cuerno, and J. J. Ruiz-Lorenzo, Phys. Rev. E 106, 044801 (2022).

In this chapter, we study the kinetic roughening behavior of fronts of coffee-ring aggregates via extensive numerical simulations of an off-lattice model. The model describes aggregation of patchy colloids and depends on a parameter r_{AB} which determines how well two particles stick together. We find a discontinuous pinning-depinning transition at $r_{AB} = 0$, only noticeable choosing suitable boundary conditions. For $0 < r_{AB} \leq 1$, comparison with standard ballistic deposition simulations reveals that the patch structure causes a morphological instability. The intermediate time regime exhibits one-dimensional KPZ exponents for $r_{AB} > 0.01$, and the system suffers a strong crossover dominated by the $r_{AB} = 0$ behavior for $r_{AB} \leq 0.01$. A detailed analysis of correlation functions shows that the aggregate fronts are always in the moving phase for $0 < r_{AB} \leq 1$ and that their kinetic roughening behavior is intrinsically anomalous for $r_{AB} \leq 0.01$, including $r_{AB} = 0$. Finally, we find that the asymptotic morphological behavior is dominated by macroscopic shapes.

5.1 Introduction

The so-called coffee-ring effect stands out as one of the nontrivial non-equilibrium behaviors emerging in the context of statistical physics and influencing several industrial processes [134]. Let us consider a drop of a liquid containing suspended particles which dries up on a solid substrate. During the evaporation process, the contact line of the droplet becomes immobilized on the substrate, causing liquid to flow outward from inside the droplet [135, 136]. The suspended solid particles are then dragged by capillary flow to the edges of the drop, where they agglomerate in such a way that, after evaporation, they give rise to a characteristic ring-like stain. Thus, this familiar but complex effect results from the convergence of diverse physical-chemical factors (capillarity, Marangoni flow), but also of geometrical ones.

In this context, Yunker *et al.* [137] showed that the structure of the ring-like pattern could be sensitively altered by changes in the shape of the suspended particles; interestingly, this effect was observed without any corresponding alteration in the contact-line behavior of the capillary rates. Specifically, increasing the aspect ratio of the particles leads to the emergence of intricate patterns, not necessarily ring-like ones, reaching the entire suppression of the coffee-ring effect for ellipsoidal particles of large enough eccentricity ε . The underlying physics for this phenomenon lies in the behavior of elongated particles, which are dragged to the drop edge only until they reach the liquid-air interface, where they are subject to strong long-range capillary attraction [138, 139]. Consequently, the formation of loosely-packed particle clusters becomes prominent at the interface, effectively impeding any further movement of particles. The conventional ring-like pattern does not manifest; instead a homogeneous stain is observed. By contrast, spherical particles exhibit a considerably more efficient flow towards the droplet edge, where they aggregate and give rise to a discernible ring-like configuration after evaporation. Nonetheless, it is noteworthy that inserting a quantity of eccentric particles into a suspension dominated by spherical ones also leads to the suppression of the coffee-ring effect. This phenomenon occurs as long as the diameters of the spherical particles exceed the minor axis of the ellipsoidal particles [137].

In a later work, Yunker *et al.* characterized the space-time evolution of

the front of the particle aggregate by measuring its height h and roughness w as functions of time [140]. Regardless of the specific particles eccentricity, the front width increased in time following a power law characteristic of surface kinetic roughening, namely Eq. (1.1). For spherical particles ($\varepsilon = 1$) $\beta \simeq 1/2$ was measured, consistent with a random deposition behavior. Increasing the eccentricity of the suspended particles to $\varepsilon = 1.2$ changes the growth exponent to $\beta \simeq 1/3$, characteristic of the 1D KPZ universality class. Further consistence with KPZ scaling was confirmed by the roughness exponent $\alpha \simeq 1/2$ and by the skewness and kurtosis of the distribution of height fluctuations, both of them are observed to take values consistent with those of the TW distribution exhibited by 1D KPZ processes. Finally, for even more eccentric particles ($\varepsilon > 2.5$), the dynamic evolution of the front yields larger values $\alpha \simeq 0.61$, $\beta \simeq 0.68$, which the authors interpreted as consistent with the QKPZ universality class.

The latter fact is surprising, since sources of quenched disorder cannot be clearly identified in the experiment [87, 141]. Yunker *et al.* [137] argued that, when highly eccentric particles reach the air-liquid interface at specific sites, these sites become preferential locations for the subsequent deposition of additional particles. Such a preference is attributed to the pronounced capillary attractions previously mentioned, which act to the detriment of regions lacking particles. This non-uniform pattern of growth, leading to distinctive QKPZ exponent values, could potentially be instigated by a colloidal analogue of the “Matthew effect” [140], in the sense that particle-rich regions become richer and particle-depleted ones remain poorly populated [142]. However, the colloidal Matthew effect implies a dynamical instability for the front morphology, in which quenched disorder plays no role, as eloquently demonstrated for example in the supplementary video 3 of the experiments described in Ref. [140]. This interpretation was tested by numerical simulations [87] of the lattice growth model introduced in Ref. [140] to describe the large ε experiments. Simulations showed that the resultant instability indeed leads to elevated values of the scaling exponents, consistent with those observed in the experiments involving large eccentricities. More precisely, at large ε , the Matthew effect gives rise to anomalous kinetic roughening for the front [87–90]. In particular, the critical exponent values may not be universal, but rather depend on geometry and physical parameters.

The origins and characteristics of QKPZ scaling associated with the coffee-ring effect have attracted considerable interest. In this context, Oliveira and Aarão Reis [143] used a ballistic-deposition-like lattice model based on the so-called RCA model [144], in which particles fall towards the substrate by moving one position down vertically and D positions horizontally. Thus, the parameter D models the aspect ratio of the suspended particles; in particular, $D = 0$ corresponds to ballistic deposition. Through their investigation, Oliveira and Aarão Reis determined that for $D = 0$ the obtained value of β was approximately 0.33, consistent with the anticipated 1D KPZ value. In contrast, for $D = 8$, they derived a value of β around 0.68, which aligns with the 1D QKPZ framework. While these extreme values agree with those measured in Ref. [140], the continuous variation of β with D contrasts with the experimental observations. Additionally, Ref. [143] provides insight into the dynamic exponent z ; specifically, the authors report $z \simeq 1.56$ for $D = 0$, compatible with 1D KPZ behavior ($z = 1.5$), but $z \simeq 2.56$ for $D = 8$, well above the 1D QKPZ prediction ($z = 1$). It is concluded that the β and z exponents computed for large D were attributable to the “columnar” growth of the front, without needing the incorporation of quenched disorder, in qualitative agreement with the analysis performed in Ref. [87].

An alternative theoretical framework to describe the kinetic roughening behavior seen in the experiments of Ref. [140] was later taken by Dias *et al.* [145–147]. This approach is founded on the concept of “patchy” colloids with weak and strong bonds. They considered an off-lattice model in which circular particles with patches fall vertically onto a flat interface. In order to model the anisotropy of the experimental ellipsoidal colloids using circular disks, the latter are assumed to have two patch pairs, namely A at the poles and B along the equator. The falling particles eventually aggregate to the substrate, or to already deposited particles, via patch-patch interactions ruled by three binding probabilities, P_{AA} , P_{AB} , and P_{BB} , corresponding to the three possible patch-patch configurations. Full details of this model will be discussed in Sec. 5.2.

Dias *et al.* found two different regimes depending on $r_{AB} \equiv P_{AB}/P_{AA}$, with $P_{AB} = P_{BB}$ for simplicity. For large r_{AB} values $0.5 \leq r_{AB} \leq 1$ (i.e., small particle eccentricity), scaling exponents are consistent [146, 147] with 1D KPZ behavior; for small $0.01 < r_{AB} < 0.1$ (i.e., large particle ec-

centricity), simulations yielded $\beta \simeq 0.63$ and $z \simeq 1$, which was ascribed to 1D QKPZ scaling, crossover behavior being obtained for intermediate $0.1 < r_{AB} < 0.5$. In general, the average front velocity was nonzero for any value of r_{AB} in the simulations of Refs. [146, 147], at variance with the QKPZ equation. Indeed, this continuum model is well-known to display a pinning transition between a pinned phase, in which the average front velocity is zero, and a moving phase (see Sec. 1.4). The transition is termed directed percolation depinning, as it is induced by the emergence of a directed percolation cluster of quenched disorder sites where front motion is arrested (see Sec. 2.6). The scaling exponents measured in Refs. [146, 147] for $0.01 \leq r_{AB} \leq 0.1$ are those of the QKPZ equation right at the transition point (see Sec. 1.4.3), while the moving phase of the DPD transition features still larger exponents $\alpha_{mp} = 0.75$ and $\beta_{mp} = 0.74$ [41, 43]. Hence, the conclusion in Refs. [146, 147] is that a pinning transition takes place for each value of r_{AB} in the finite interval $[0.01, 0.1]$.

In this chapter, we perform a systematic study of the kinetic roughening behavior of the fronts generated through the off-lattice aggregation model of Dias *et al.* in the full $r_{AB} \in [0, 1]$ parameter range, in which we consider longer evolution times and larger system sizes.

5.2 Model and simulation details

The patchy colloids model [145, 146] is a two-dimensional system that simulates the behavior of circular colloids with two different types of patches, namely A and B, see Fig. 5.1. The colloids can either fall onto a substrate or bind to already present colloids. If a deposited colloid falls onto a previous colloid, it can bind to it with a probability determined by the patch types of the two colloids and the temperature. The probability of two A-type patches binding is given by P_{AA} , and those of two B-type patches and the one A-type and one B-type patch binding are given by P_{BB} and P_{AB} , respectively. The binding probabilities are modeled as Arrhenius-like functions of temperature T ,

$$P_i \propto e^{-E_a^{(i)}/k_B T}, \quad (5.1)$$

where k_B is Boltzmann's constant and $E_a^{(i)}$ holds for the activation energy which characterizes the strength of each bond type ($i = AA, AB, \text{ and } BB$).

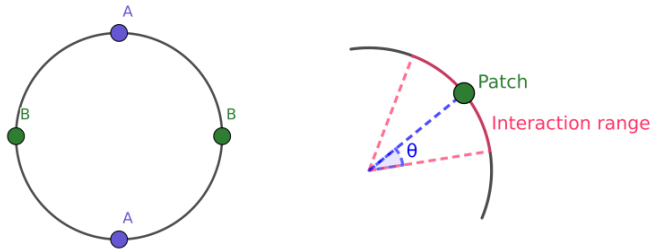


Figure 5.1: Left panel: Single patchy colloidal particle with four patches, as considered in the model of Ref. [145]. Right panel: Interaction range around a patch, described by θ .

Referring to [146], we make the assumption that $P_{AA} = 1$, and for simplicity we also assume that $P_{AB} = P_{BB}$, which does not affect the generality of our conclusions. To measure the probability of sticking between two colloids, the sticking coefficient r_{AB} is defined as the ratio of the probability of sticking between two unlike patches (P_{AB}) to the probability of sticking between two like patches (P_{AA}):

$$r_{AB} = P_{AB}/P_{AA}. \quad (5.2)$$

The interaction between colloids is limited to a specific region, namely within an angle of $\theta = \pi/6$ around each patch, as illustrated in Fig. 5.1. Two colloids only bind if their interaction ranges overlap, in which case the newly-formed aggregate particle orients itself so that its patches align with those of the pre-existing particle to which it attaches [148].

For low r_{AB} , the aggregate morphology is similar to that of ellipsoidal colloids, as it favors AA interactions; in particular, for $r_{AB} = 0$ only AA unions are favorable, resulting in long 1D chains of particles. By contrast, the behavior for $r_{AB} = 1$ is similar to that of circular (isotropic) particles, which leads to the formation of a coffee-ring aggregate. However, it should be noted that the $r_{AB} = 1$ case is not identical to the off-lattice ballistic deposition model, which belongs to the KPZ universality class, due to the finite interaction range with angle θ and the related alignment step in the attachment process. This difference will be shown to be significant later on.

Figure 5.2 illustrates the likelihood of bond formation for our model: for a bond to form, the interaction ranges of both particles must overlap. As this overlap is determined by an angle $\theta = \pi/6$ around each of the four patches,

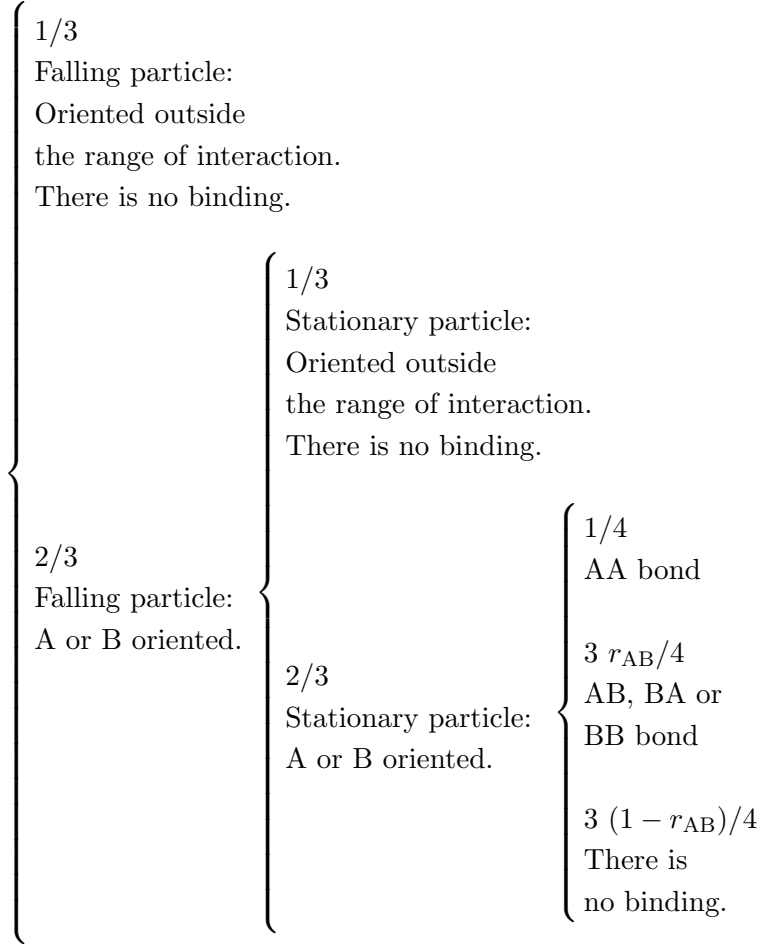


Figure 5.2: Schema of bond formation.

the probability of overlap is $4/9$. Additionally, bond formation depends on the facing patches, which can be AA, AB, BA, or BB. If the facing patches are AA, a bond is always formed with a probability $P(\text{AA}) = 1$. In all other cases, bond formation occurs with a probability r_{AB} , which is a parameter of the system [specifically, $P(\text{AB}) = P(\text{BA}) = P(\text{BB}) = r_{AB}$]. Therefore, when two particles interact, they may or may not form a bond. Time increases by one unit with each new particle added to the system, regardless of whether bonding occurs or not.

We study the front propagation in the perpendicular direction of an one-dimensional substrate of size L . To measure the front position we divide

the lattice into L columns with equal widths $\Delta = 2R = 1$. At $t = 0$, the system is completely empty. At each time step, a particle of radius R falls randomly onto a position x on the substrate with random orientation. As mentioned, the particle may then either attach to the surface or interact with an existing, stationary particle if it is present within a range of $(x - \Delta, x + \Delta)$, where Δ is either the diameter of the particle or the width of the columns; if there are multiple particles within this range, the new particle interacts with the highest one. If the bond does not occur, the new particle disappears. We have arbitrarily set $R = 0.5$ and $\Delta = 1$; these values are not critical to our general findings. At each column i , the front $h(x_i, t)$ is defined as the y -coordinate of the highest particle in this column, even if only part of it is there. Hereafter, the front position will be denoted as $h(x, t)$ for simplicity.

In every instance we opted for free boundary conditions (FBC) along the substrate direction. This decision was made instead of the more common periodic ones [11] due to the system morphological changes for $r_{AB} = 0$. When PBC are used the system grows indefinitely, which contradicts the expected behavior of the system eventually reaching a steady state at a finite time t , which will be discussed below. To maintain consistency, we also used FBC for nonzero r_{AB} values. In Sec. 5.3.9, we compare the outcomes obtained from both types of boundary conditions.

The conditions that were set for all the runs mentioned in this chapter can be found in Table 5.1.

5.3 Results

5.3.1 Aggregate morphology

The morphology of the colloidal aggregates varies with r_{AB} , as illustrated in Fig. 5.3 for values of r_{AB} equal to 1, 0.1, 0.01, and 0. The appearance is similar for $r_{AB} \geq 0.1$, featuring a disordered tangle of branches pointing in random directions. The cluster shapes for $r_{AB} = 1$ and $r_{AB} = 0.1$ are similar to experimental observations of closely-packed clusters of almost-spherical colloids ($\varepsilon \simeq 1.0 - 1.5$) [147]. These morphologies also resemble those produced by the simple off-lattice ballistic deposition model, known to exhibit KPZ scaling behavior [11, 149]. The density of secondary branches

Table 5.1: Parameter values for our numerical simulations.

L	r_{AB}	t_{max}	runs
128	1	100×10^3	200
	0.5	100×10^3	
	0.4	100×10^3	
	0.3	100×10^3	
	0.2	100×10^3	
	0.1	100×10^3	
	0.01	100×10^3	
	0.001	100×10^3	
	0.0001	100×10^3	
0	200×10^3		
512	1	30×10^3	200
	0.5	42×10^3	
	0.4	46×10^3	
	0.3	50×10^3	
	0.2	57×10^3	
	0.1	82×10^3	
	0.01	100×10^3	
	0.001	110×10^3	
	0.0001	300×10^3	
0	400×10^3		
2048	1	20×10^3	40
	0.5	20×10^3	
	0.4	20×10^3	
	0.3	20×10^3	
	0.2	20×10^3	
	0.1	30×10^3	
	0.01	70×10^3	
	0.001	100×10^3	
	0.0001	120×10^3	
0	130×10^3		
2048	BD	20×10^3	420

that grow from pre-existing ones (rather than from the surface) decreases as the probability of binding between the two types of particles (and thus r_{AB}) decreases, which is consistent with the experimental observation that loosely-packed aggregates form when the particles are highly elongated. In the limit of $r_{AB} = 0$, secondary branches are entirely suppressed, and the cluster grows only in certain directions determined by the initially deposited particles.

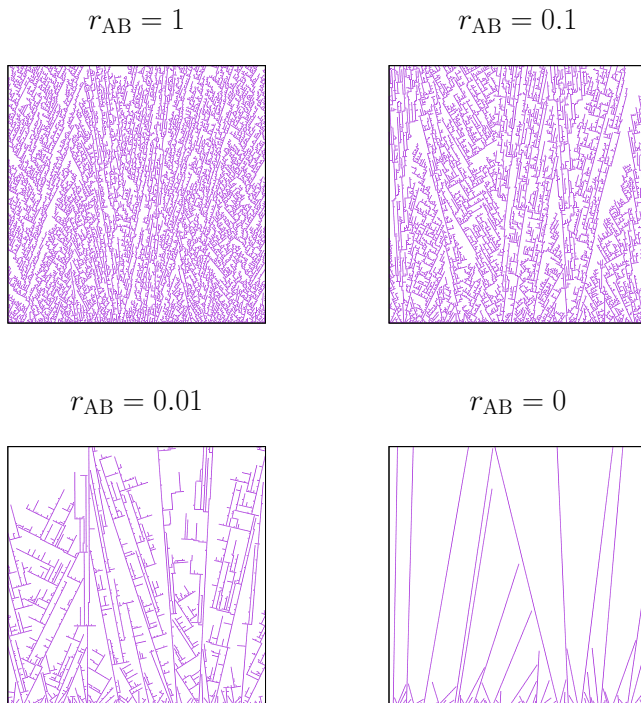


Figure 5.3: Morphologies of the colloidal aggregates calculated using different values of r_{AB} (approximately, inverse colloid eccentricities), as indicated on each panel. Individual colloid particles are represented as bullets. These snapshots were generated for a system size of $L = 256$ and until a time when the points of the morphologies vertically extend beyond the plot frames.

5.3.2 Front velocity

For all r_{AB} , the average front grows linearly over time as

$$\overline{\langle h(t) \rangle} = vt + a_0, \quad (5.3)$$

where the slope v defines the front velocity and a_0 is a constant which depends on r_{AB} . Fig. 5.4 displays the front velocity as a function of r_{AB} for different system sizes L . Two different regimes may be seen in this plot. For $0 < r_{AB} \lesssim 0.1$, the front velocity remains approximately r_{AB} -independent. For $r_{AB} > 0.1$, on the contrary, the velocity increases as r_{AB} does. In any case, the front is always moving, regardless of the value of r_{AB} . It is also worth noting that the size of the system, L , does not make much difference in how fast the front moves, except when r_{AB} is very small, in which case v increases slightly as L gets larger.

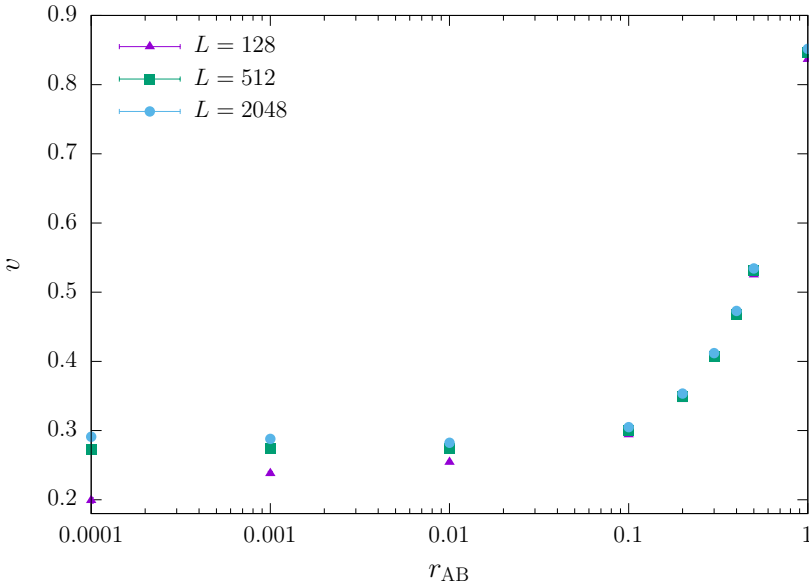


Figure 5.4: Front velocity v against r_{AB} for various lateral sizes $L = 128$, 256, and 2048. The error bars are smaller than the symbol size in all cases.

A more thorough study is needed for the case $r_{AB} = 0$ [148]. This condition implies that only AA bonds are formed, which leads to the growth of branches in only a few directions and the absence of secondary branches. Consequently, a small number of branches becomes dominant and reaches the system boundary, hindering the overall growth of the front. An example of this scenario is depicted in Fig. 5.5. As a result, the system becomes trapped at a steady state with average velocity $v = 0$. This observation is supported by Fig. 5.6, which displays the average front $\langle \overline{h(t)} \rangle$ as a function of time for $r_{AB} = 0$. For $L = 128$, the front grows linearly with time

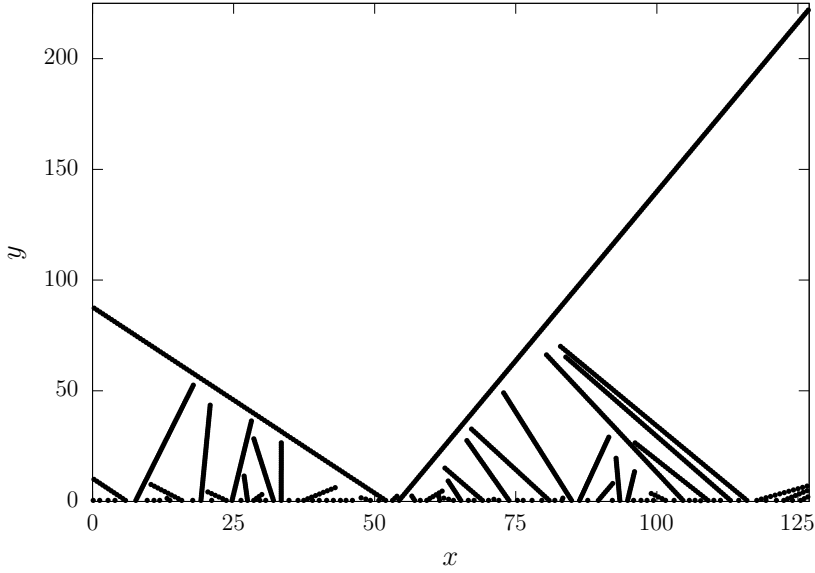


Figure 5.5: Front morphology for $r_{AB} = 0$, with $L = 128$ and at $t = 700$. Two branches of the system have grown and reached the boundary, preventing any further growth of the system front. Consequently, the system becomes frozen in a steady state.

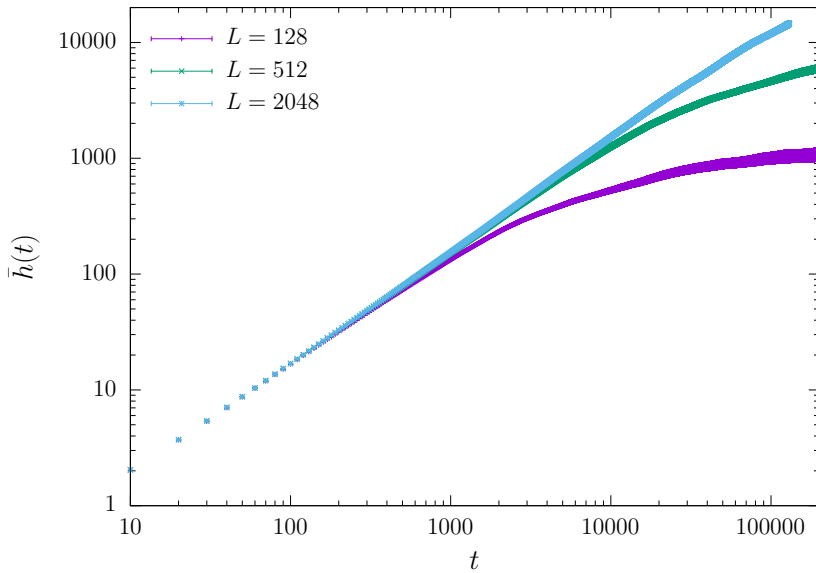


Figure 5.6: Mean front $\langle \bar{h}(t) \rangle$ as a function of time for $r_{AB} = 0$. The slopes of the curves decrease to zero as time increases.

for short periods, consistent with Eq. (5.3). However, the front velocity decreases monotonically for $t \gtrsim 1000$ until it eventually vanishes. The same trend is visible for larger lateral sizes, but the linear growth regime persists for longer times as L increases. Unfortunately, the required computation times for $L = 2048$ exceed our capabilities, and the anticipated plateau for this value of L is not observed.

When the size of the lattice increases, the velocity increases as well, except in unusual situations. This means that, for r_{AB} greater than zero, the velocity eventually reaches a non-zero value. The conclusion from this analysis is that there is a discontinuity in the front velocity v , indicating a first order transition: v is non-zero for $r_{AB} > 0$, but vanishes for $r_{AB} = 0$. The change in trend of the velocity around $r_{AB} \simeq 0.1$ (where its slope becomes flatter) is not a result of a new phase transition, but rather a crossover effect.

Apart from aggregate morphologies and front velocity, we have also observed differences in the front fluctuations, i.e., the kinetic roughening properties, between the cases $r_{AB} = 0$ and $r_{AB} > 0$. In the following sections, we present the results for both scenarios. All calculations were conducted for a system size of $L = 2048$ and time intervals of $t \lesssim 20000 - 130000$, unless otherwise mentioned. Previous simulations in Ref. [147] were carried out for smaller system sizes of $L \leq 512$ and shorter timescales of $t \lesssim 4000$, so that our values significantly extend these previous results.

5.3.3 Front roughness

Figure 5.7 shows the squared front roughness $w^2(t)$ computed for various values of r_{AB} . It is evident from the figure that, regardless of the value of r_{AB} , the front roughness increases with time. Furthermore, it is worth noting that the sizes of the systems employed in the analysis ensure that the interface does not reach a steady state for any r_{AB} . This is crucial, since it enables us to examine the most significant mechanisms that govern the system large-scale behavior, as discussed below in the context of the crossover phenomenon.

To perform a qualitative analysis, the curves shown in Fig. 5.7 were fitted to the FV scaling law (3.4) using two separate time intervals: intermediate

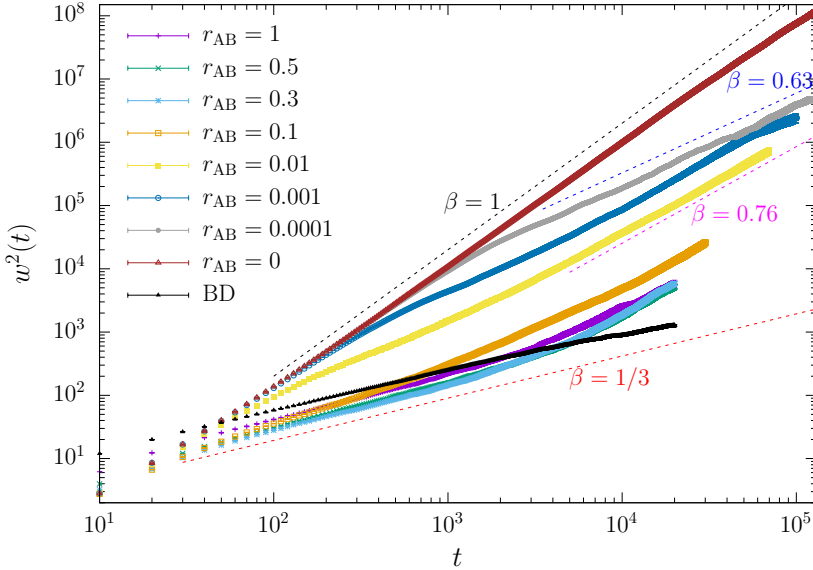


Figure 5.7: Squared front roughness vs. time for values of r_{AB} as indicated in the legend. Error bars are smaller than the symbol sizes.

times and long times. Any very short time periods were disregarded as transient. The results, presented in Table 5.2, exhibit two distinct regimes depending on time.

1. One observes a power-like trend for $t \lesssim 1000$ (intermediate times) and $r_{AB} \geq 0.3$, which is consistent with the $\beta = 1/3$ exponent for 1D-KPZ. On the other hand, for $r_{AB} = 0.01$ and 0.001 the growth exponent value seems consistent with the $\beta \simeq 0.63$ QKPZ value. According to this, the $r_{AB} = 0.1$ case may be consistently regarded as a crossover. Note that, for $r_{AB} \leq 0.01$, the w^2 -curves overlap the $r_{AB} = 0$ curve at short times (see Fig. 5.7).
2. For longer times, the curvatures increase regardless of r_{AB} , suggesting very high asymptotic values for β . For instance, $\beta \simeq 0.76$ for $r_{AB} = 0.01$ and $t \gtrsim 3000$. As an additional reference, we have run simulations of the simple off-lattice ballistic deposition (BD) model, see Sec. 5.3.10. The BD data are included in Fig. 5.7 and feature the expected KPZ scaling for all simulated times. In particular, the difference with the $r_{AB} = 1$ case becomes apparent for $t \gtrsim 3000$.

3. For $r_{AB} = 0$, the value of $\beta \approx 1$ is essentially time-independent.

Table 5.2: Growth exponent β for different values of r_{AB} computed for intermediate and long times.

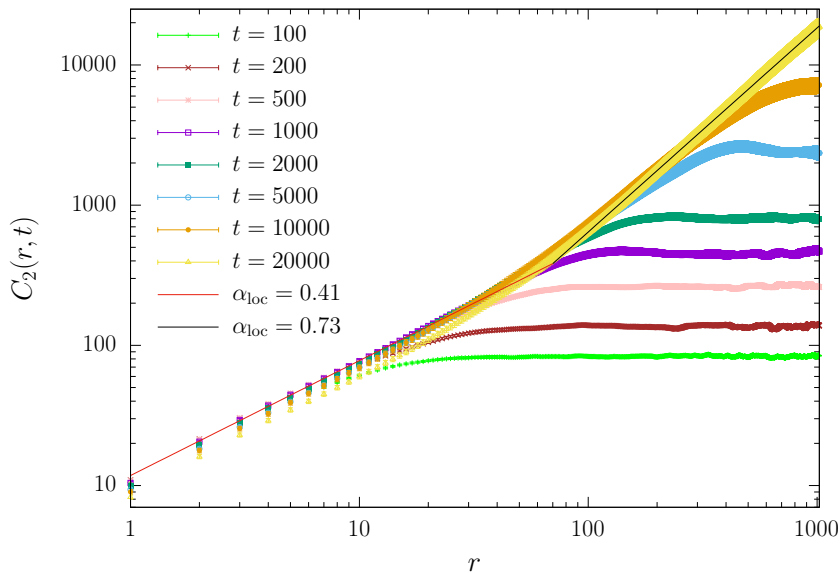
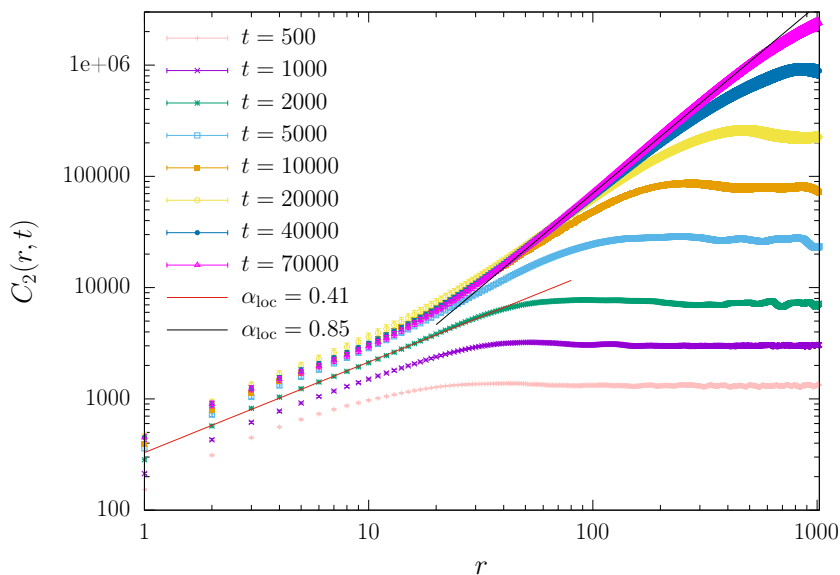
r_{AB}	intermediate t	β	long t	β
1	[40 : 800]	0.349(7)	[3000 : 20000]	0.62(4)
0.5	[100 : 1000]	0.352(2)	[5000 : 20000]	0.76(4)
0.3	[60 : 1000]	0.353(5)	[6000 : 20000]	0.81(3)
0.1	[100 : 1000]	0.462(6)	[15000 : 30000]	0.80(5) ^a
0.01	[350 : 2000]	0.603(7)	[5000 : 70000]	0.76(3)
0.001	[500 : 2000]	0.594(10)	[2500 : 40000]	0.73(2)
0.0001	[60 : 900]	0.920(2)	[2000 : 120000]	0.632(11)
0	[200 : 30000]	0.978(2)	[70000 : 130000]	0.87(6)

^aFor $r_{AB} = 0.1$ there exists another time interval between those shown, namely [1000 : 15000], with $\beta = 0.62(2)$.

5.3.4 Height-difference correlation function

The correlation function $C_2(r, t)$ has been calculated for r_{AB} values ranging from 0 to 1. The outcomes, at various times, are presented in Fig. 5.8. The behavior of the $C_2(r, t)$ function is quite intricate, and some of its features include:

- In general, for r_{AB} values except $r_{AB} = 0$, the power law $C_2(r, t) \sim r^{2\alpha_{loc}}$ applies to short distances relative to the correlation length ξ , while a plateau is observed at larger distances. However, for sufficiently long times and $r_{AB} \neq 0$, a second power law can be detected at large distances, with an α_{loc} exponent that is larger than that found at short distances. This effect is highlighted by straight lines with different slopes in Figs. 5.8. For instance, for $r_{AB} = 1$, the $C_2(r, t)$ curve shows $\alpha_{loc} = 0.41$ for $r \lesssim 100$, and the value of α_{loc} increases for larger r , reaching 0.73 for the longest time reached. Similarly, for $r_{AB} = 0.01$, the α_{loc} values can be as high as 0.85 at

(a) $C_2(r, t)$ for $r_{AB} = 1$.(b) $C_2(r, t)$ for $r_{AB} = 0.01$.

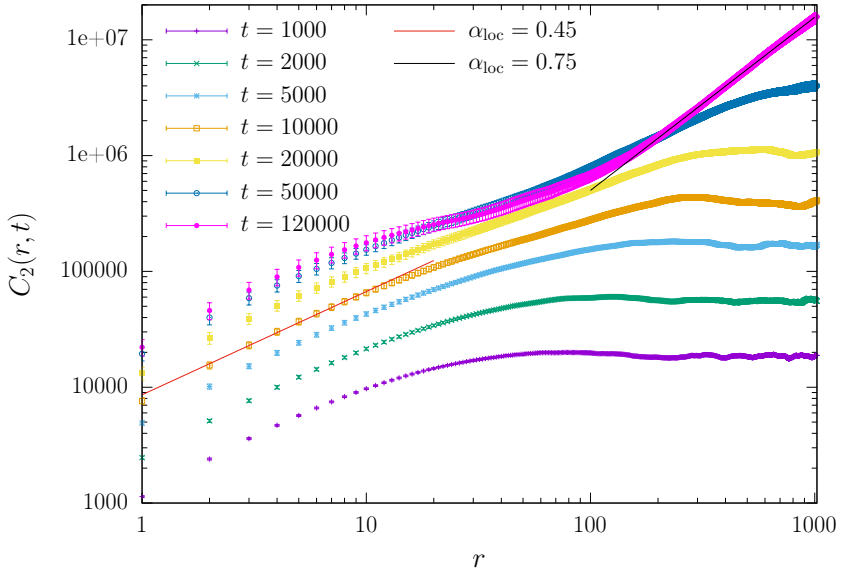
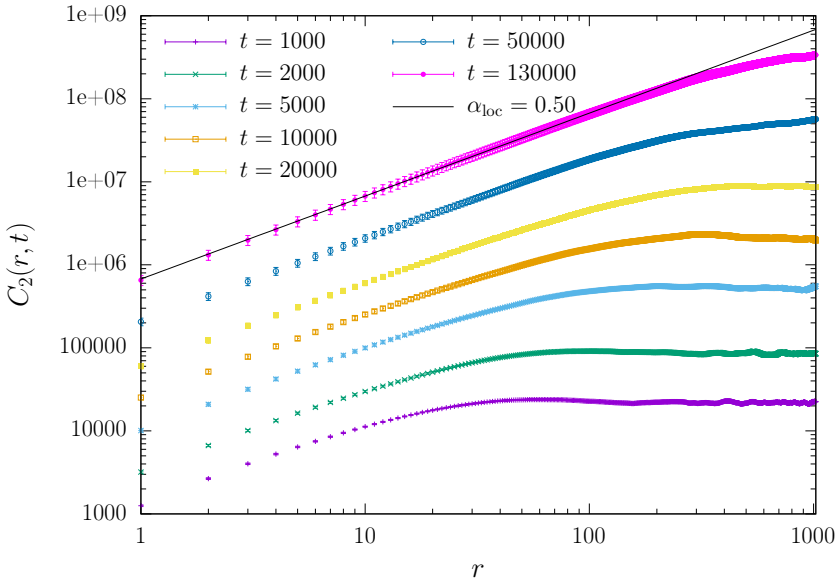
(c) $C_2(r, t)$ for $r_{AB} = 0.0001$.(d) $C_2(r, t)$ for $r_{AB} = 0$.

Figure 5.8: Correlation function $C_2(r, t)$ vs. r for various r_{AB} and times. The solid lines correspond to fits to the power law $r^{2\alpha_{loc}}$ within different r intervals.

large distances. By contrast, in off-lattice BD, $C_2(r, t)$ exhibits a single roughness exponent $\alpha_{\text{loc}} = \alpha = 1/2$ for all values of r and t , and one does not find two different scaling behaviors for small and large distances at long times. This effect is discussed in greater detail in Sec. 5.3.10.

- For extremely small r_{AB} , such as 0.0001 (see Fig. 5.8c), the behavior of the $C_2(r, t)$ curves is distinct at short and long distances for long times. In Sec. 5.3.7 below, further explanations regarding the possible cause of this unusual behavior will be provided.
- For each value of r_{AB} between 0 and 0.01, the $C_2(r, t)$ curves shift upward in a steady manner and do not overlap as time increases. This pattern continues until a second power-law regime emerges, at which point the curves begin to roughly overlap for small r . This behavior is a sign of anomalous kinetic roughening, which has been studied previously [88–90]. However, for $r_{\text{AB}} \geq 0.1$, there is no noticeable vertical shift in the curves over time, as seen in the case where $r_{\text{AB}} = 1$ in Fig. 5.8a. This can be explained by the fact that, for short times and large r_{AB} , the system belongs to the KPZ universality class, which does not display anomalous scaling. A more thorough discussion of anomalous scaling is provided in Sec. 5.3.6 below.

5.3.5 Correlation length

In Sec. 3.1 we explained how to determine the correlation length $\xi(t)$ from the height-difference correlation function. However, this method can only be used if the correlation function behaves in a certain way. Specifically, the correlation function must increase with distance until it reaches the correlation length, at which point it becomes constant. Note, however, that as time increases the correlation length increases as well, and the method described in Sec. 3.1 is no longer valid when the correlation length becomes comparable to the size of the system. Moreover, as we have already mentioned, at long times the $C_2(r, t)$ curves in this system do not exhibit standard behavior. As a consequence, the method described in Sec. 3.1 to compute $\xi(t)$ is valid only for a limited range of intermediate times.

Figure 5.9 displays the variation of the correlation length $\xi_{0.9}(t)$, ob-

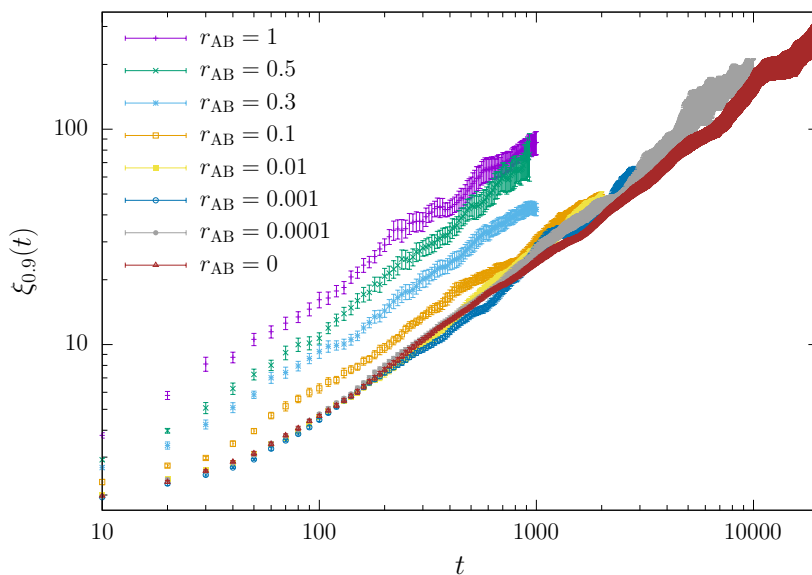


Figure 5.9: Correlation length vs. time for several values of r_{AB} , as indicated in the legend.

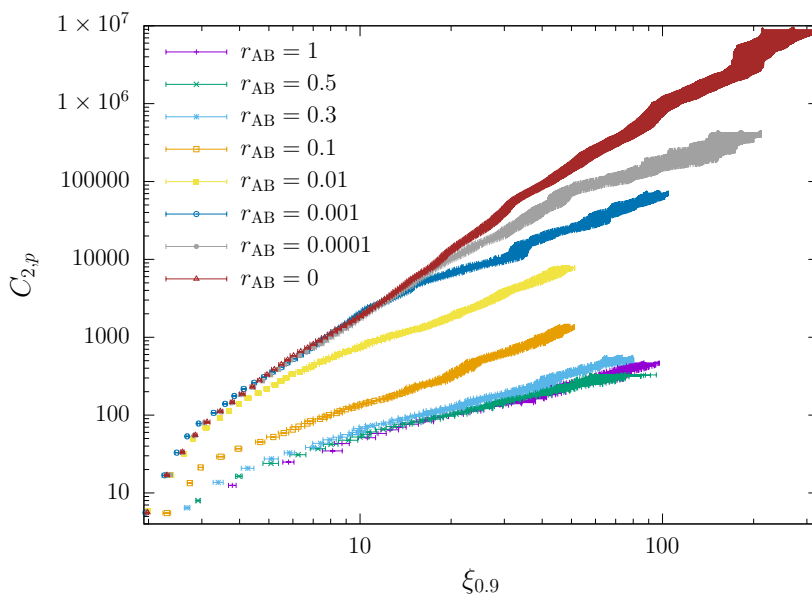


Figure 5.10: Plateau correlation value vs. correlation length for values of r_{AB} as indicated in the legend.

tained from Eq. (3.15) with a parameter value of $a = 0.9$, for different values of r_{AB} . By fitting the computed $\xi(t)$ curves to Eq. (3.6), we may estimate the dynamic exponent z for each r_{AB} . Our results, which are presented in Table 5.3, suggest that the dynamic exponent values for $r_{AB} \geq 0.1$ are consistent with the KPZ universality class ($z_{\text{KPZ}} = 3/2$), while for $0 < r_{AB} \leq 0.01$ the dynamic exponent is approximately 1, a value shared by the QKPZ and moving DPD phase universality classes. To the best of our knowledge, no previous studies have reported on the values of the dynamic exponent z for the patchy colloid model.

In addition to the dynamic exponent z , one may also compute the global roughness exponent α by plotting the plateau of the height-difference correlation function $C_{2,p}(t)$ against the correlation length $\xi_{0.9}(t)$ [see Eq. (3.14)]. Figure 5.10 shows these curves, and the computed α values are collected in Table 5.3. For $r_{AB} \geq 0.3$, the estimated roughness exponent values are consistent with the 1D KPZ universality class ($\alpha_{\text{KPZ}} = 1/2$). On the other hand, for $0 < r_{AB} \leq 0.1$, the roughness exponent value is compatible with the 1D DPD universality class in the moving phase. However, for $r_{AB} = 0$, both the roughness and dynamic exponents deviate from the previously estimated values, and are larger than one.

Since $\beta = \alpha/z$, we may compare the α/z ratio obtained from the data in Table 5.3 with the β values presented in Table 5.2, which were calculated directly from the front roughness. The results also appear in Table 5.3. The

Table 5.3: Critical exponents z and α for several values of r_{AB} .

r_{AB}	intermediate t	z	α	α/z
1	[10 : 1000]	1.44(6)	0.50(2)	0.35(2)
0.5	[100 : 1000]	1.20(11)	0.45(3)	0.37(4)
0.3	[20 : 1000]	1.46(5)	0.54(2)	0.37(2)
0.1	[30 : 2000]	1.47(4)	0.721(16)	0.489(18)
0.01	[200 : 1500]	1.22(5)	0.73(3)	0.60(3)
0.001	[2000 : 5000]	1.11(15)	0.77(7)	0.69(11)
0.0001	[3000 : 10000]	1.07(22)	0.71(14)	0.66(19)
0	[1400 : 20000]	1.18(8)	1.18(7)	1.00(9)

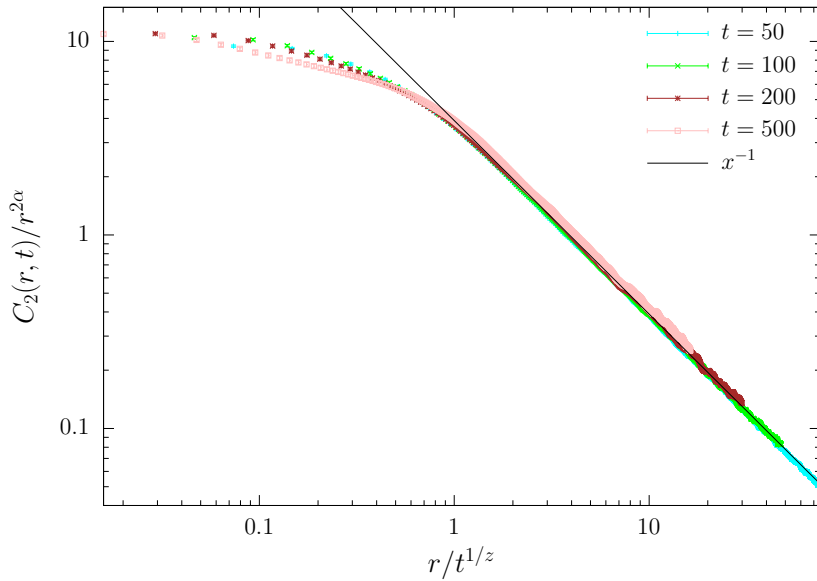
α/z ratios are consistent with the growth exponent measured at intermediate times, except for the cases $r_{AB} = 0.001$ and $r_{AB} = 0.0001$, for which the α/z values are closer to the β values obtained at long times. This observation suggests that for $r_{AB} > 0.001$ the system has not yet reached the asymptotic regime, and the growth regimes shown in Fig. 5.7 correspond instead to intermediate times.

5.3.6 Intrinsic anomalous scaling

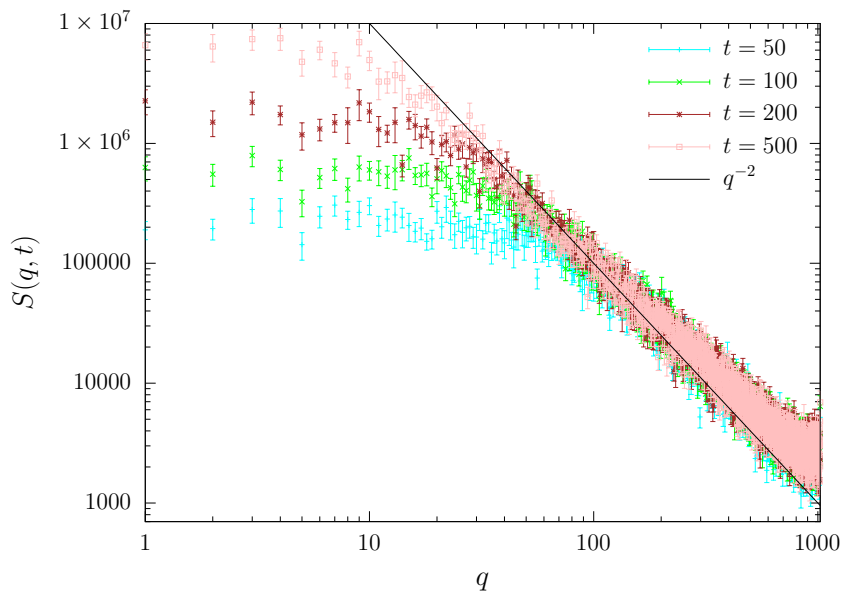
The gradual shift upward of the height-difference correlation function $C_2(r, t)$ curves with time is a sign of anomalous kinetic roughening [88–90], as explained in Sec. 3.1. In this system, this behavior is observed for $r_{AB} \leq 0.01$, as previously mentioned in Sec. 5.3.4.

In a system governed by the FV scaling Ansatz, the scaling function $g_{FV}(u)$ described in Eq. (3.13) remains independent of u for $u \ll 1$, as is the case with the KPZ equation [11, 150]. In the context of this model, we may observe the KPZ scaling exponents at intermediate times when r_{AB} is large. The question arises as to whether this regime follows a FV scaling Ansatz, as expected for the KPZ equation, or if it exhibits anomalous scaling. In order to answer this question we represent the intermediate time behavior of the scaled front height-difference correlation function, $C_2(r, t)/r^{2\alpha}$ versus $r/t^{1/z}$ for $r_{AB} = 1$ in Fig. 5.11a. We have also computed the structure factor $S(q, t)$ [see Eq. (3.17)], since this function provides information about the scaling, as explained in Sec. 3.1 [88]. Figure 5.11b plots $S(q, t)$ against the wave vector q for $r_{AB} = 1$ and the same times as in the previous plot, Fig. 5.11a. The behavior is largely consistent with a FV scaling Ansatz, indicating that scaling is not anomalous at intermediate times.

In contrast, data for $r_{AB} \leq 0.01$ fit a scaling function of the form $g(u) \sim u^{-2(\alpha - \alpha_{loc})}$, as described in Eq. (3.16), where $\alpha_{loc} \neq \alpha$. Figure 5.12a shows the collapsed $C_2(r, t)$ data for different times and $r_{AB} = 0.01$. Within the time range covered by the plot, our data align with the previously discussed values of $z = 1.22(5)$ and $\alpha = 0.73(3)$. Additionally, by fitting the $t = 1000$ curve to $u^{-2\alpha'}$ for $u \ll 1$, where $\alpha' = \alpha - \alpha_{loc}$, we obtain $\alpha' = 0.364(4)$, and therefore $\alpha_{loc} = 0.366(4) \neq \alpha$. This behavior suggests the existence of intrinsic anomalous scaling since $\alpha_{loc} < 1$ [88]. The front structure factor $S(q, t)$ for the same data is shown in Fig. 5.12b. We ob-

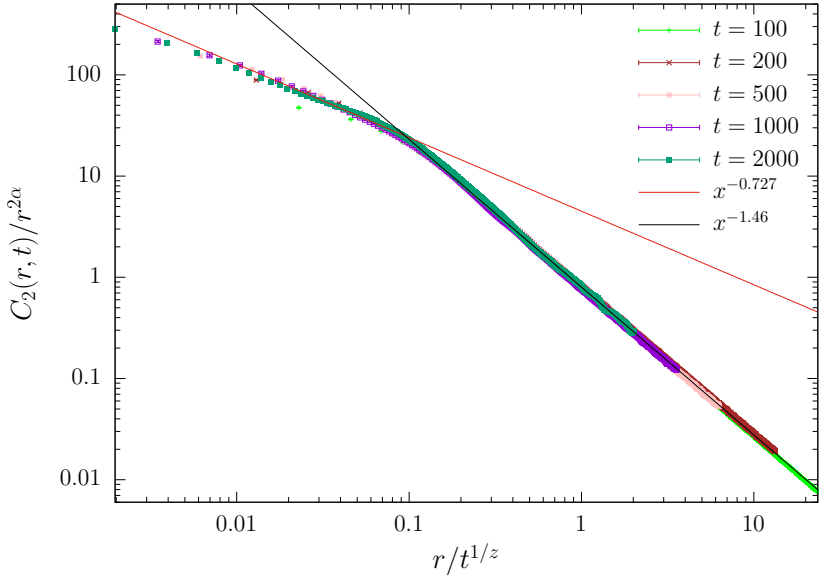


(a) Data collapse of $C_2(r, t)$ for intermediate times using KPZ exponents $z = 1.5$ and $\alpha = 0.5$. The solid line corresponds to the power law $g(x) \sim x^{-2\alpha}$ for $x > 1$, with $x = r/t^{1/z}$, Eq. (3.16).

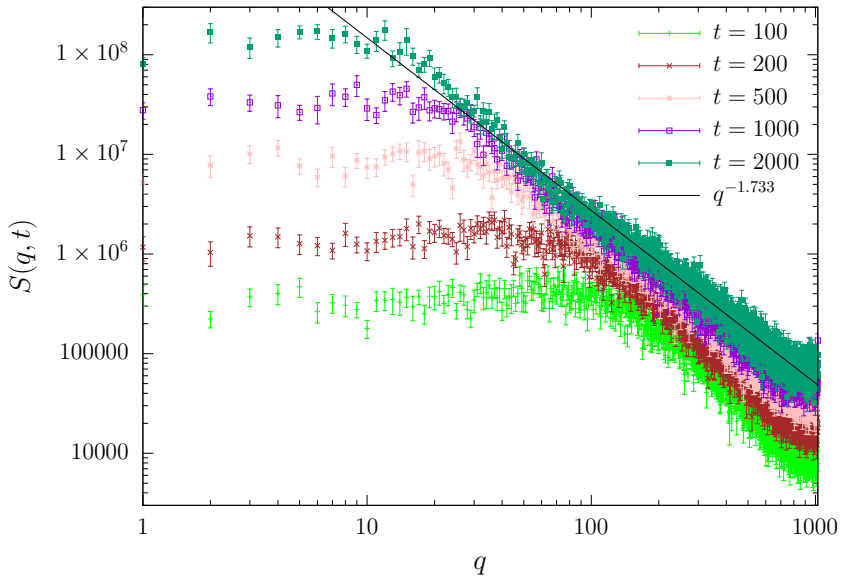


(b) Structure factor $S(q, t)$ for times indicated in the legend. The solid line corresponds to $q^{-(2\alpha+1)}$, Eq. (3.19).

Figure 5.11: Collapsed $C_2(r, t)$ and $S(q, t)$ for $r_{AB} = 1$.

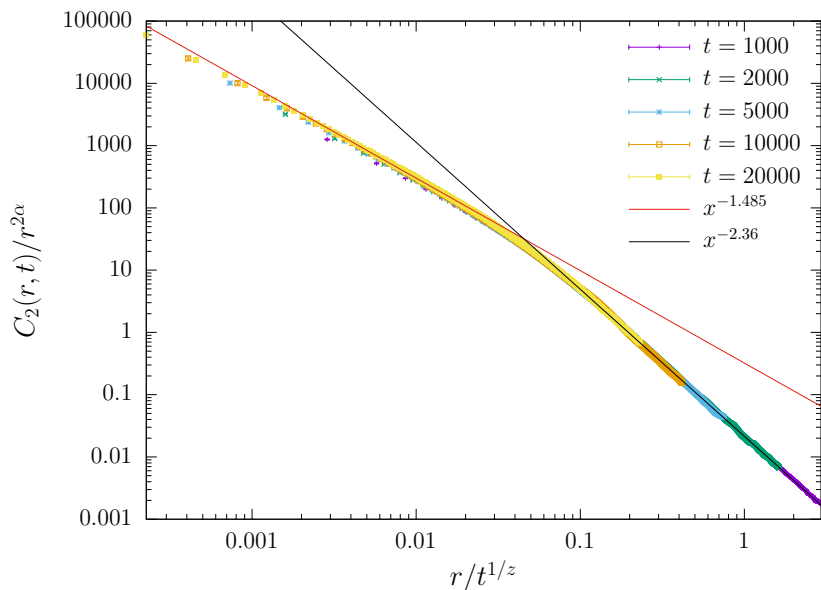


(a) Data collapse of $C_2(r, t)$ for intermediate times using the computed exponents $z = 1.22$ and $\alpha = 0.73$. The solid lines correspond to the power laws $g(x) \sim x^{-2\alpha'}$ (fitting to the $t = 1000$ curve for $x < 0.1$) and $g(x) \sim x^{-2\alpha}$, with $x = r/t^{1/z}$.

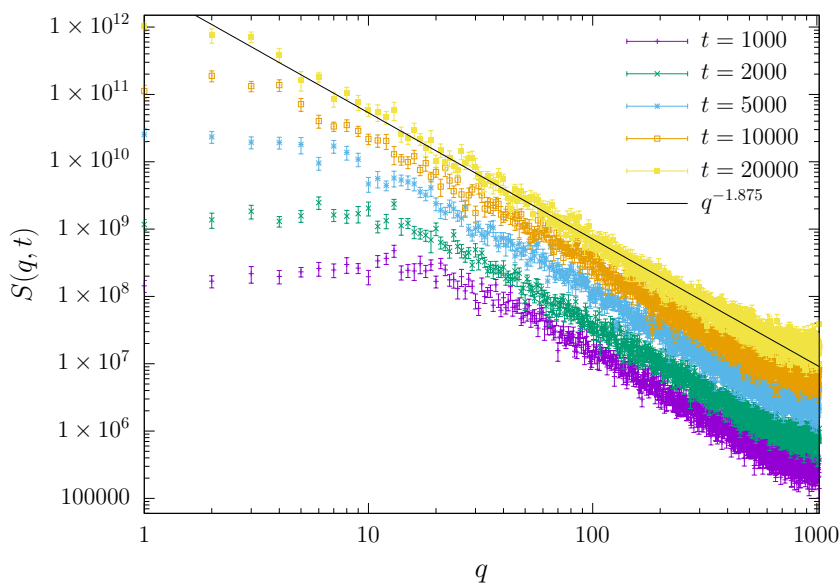


(b) Structure factor $S(q, t)$ for times indicated in the legend. The solid line corresponds to $q^{-(2\alpha_{\text{loc}}+1)}$ where $\alpha_{\text{loc}} = \alpha - \alpha' = 0.366(4)$ as obtained from the analysis of the data collapse for $C_2(r, t)$.

Figure 5.12: Collapsed $C_2(r, t)$ and $S(q, t)$ for $r_{\text{AB}} = 0.01$.



(a) Data collapse of $C_2(r, t)$ using the computed exponents $z = 1.18$ and $\alpha = 1.18$. The solid lines correspond to the power laws $g(x) \sim x^{-2\alpha'}$ (fitting to the $t = 20000$ data for $x < 0.03$) and $g(x) \sim x^{-2\alpha}$, with $x = r/t^{1/z}$.



(b) Structure factor $S(q, t)$ for times indicated in the legend. The solid line corresponds to $q^{-(2\alpha_{\text{loc}}+1)}$ where $\alpha_{\text{loc}} = \alpha - \alpha' = 0.437(9)$, as obtained from the analysis of the data collapse for $C_2(r, t)$.

Figure 5.13: Collapsed $C_2(r, t)$ and $S(q, t)$ for $r_{\text{AB}} = 0$.

serve that the time curves systematically shift upwards with increasing time, which is indeed indicative of the presence of intrinsic anomalous scaling behavior [88]. As noted in Sec. 3.1, when intrinsic anomalous scaling is present, the structure factor scales with the wave vector as $S(q, t) \sim q^{-(2\alpha_{\text{loc}}+1)}$ for large q , where α_{loc} is the local roughness exponent [see Eq. (3.19)]. The straight line in Fig. 5.12b corresponds to the value of α_{loc} obtained from the collapse of $C_2(r, t)$, which is consistent with our interpretation of the data as exhibiting intrinsic anomalous scaling.

We have also noticed intrinsic anomalous scaling for $r_{\text{AB}} = 0$, which is particularly interesting. Visual inspection of the uncollapsed $C_2(r, t)$ data in Fig. 5.8d indicates the presence of significant anomalous scaling. Our computation of the exponents [$z = 1.18(8)$ and $\alpha = 1.18(7)$] yields a consistent data collapse as shown in Fig. 5.13a. By fitting the scaling function for $t = 20000$, we obtain $\alpha' = 0.743(9)$, which leads to $\alpha_{\text{loc}} = 0.437(9) \neq \alpha$. To validate this result, we show the front structure factor $S(q, t)$ for $r_{\text{AB}} = 0$ in Fig. 5.13b, where the straight line corresponds to the expected $q^{-(2\alpha_{\text{loc}}+1)}$ behavior in this case, with the value of α_{loc} obtained from the analysis of $C_2(r, t)$.

5.3.7 Macroscopic shapes for $r_{\text{AB}} \neq 0$

In Sec. 5.3.4, we noted that the height-difference correlation functions for $r_{\text{AB}} \neq 0$ become more intricate as time increases. In Fig. 5.8, we may see that there are two distinct slopes, corresponding to small and large values of r . This suggests that two different local roughness exponents, α_{loc} , for each range of distances may be computed. Additionally, the exponent β obtained from measuring the width increases with time, as shown in Table 5.2.

An explanation for these changes may lie in the time evolution of the colloidal aggregates. At early stages, the aggregate fronts are morphologically isotropic for all values of r_{AB} , as may be observed in Fig. 5.3, and the aggregate fronts fluctuate at distances much smaller than the system size L . However, for longer times the aggregate “splits” into a few components of lateral sizes comparable to L , and the front displays macroscopic shapes. Some representative examples are shown in Fig. 5.14. Note, in particular, the development of large “facets” for $r_{\text{AB}} = 0.01$.

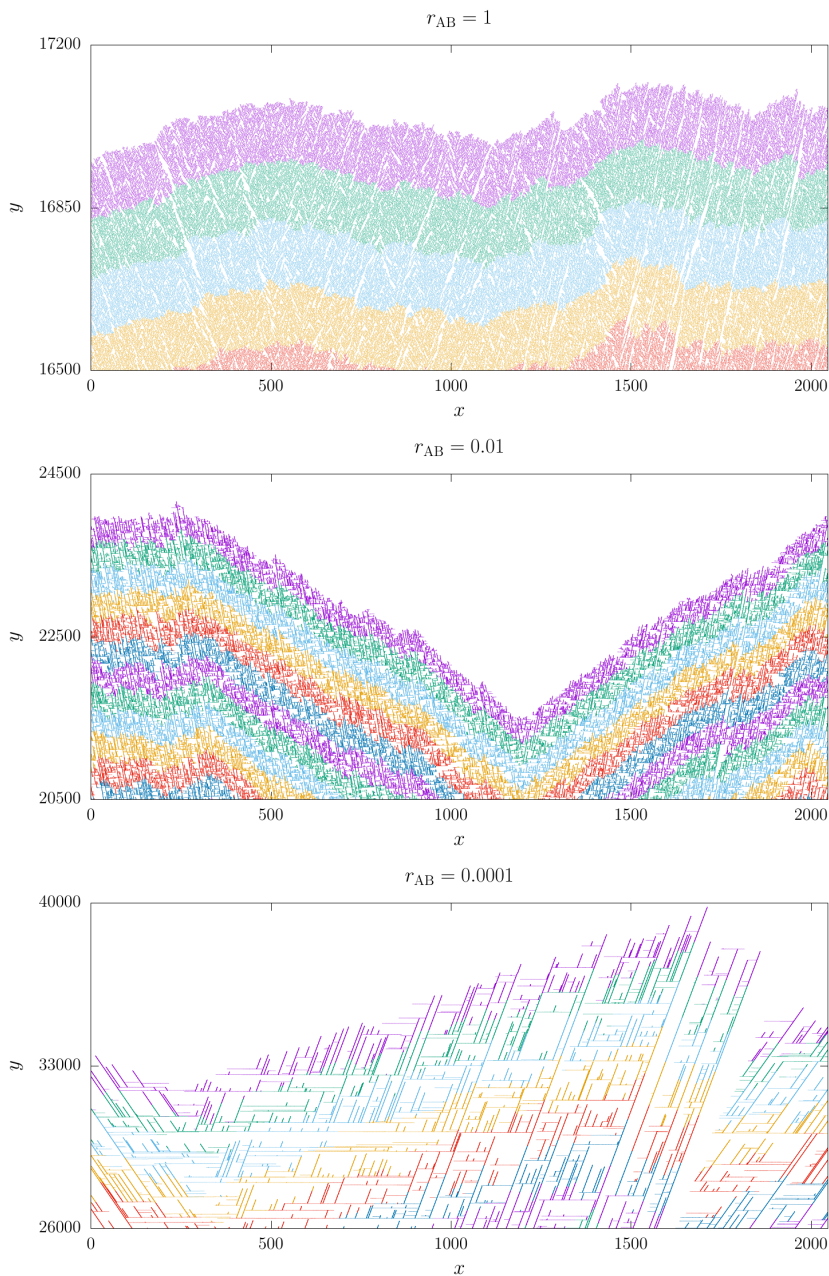


Figure 5.14: Morphologies of the colloidal aggregates at the final times, namely $t = 20000$, 70000 , and 120000 , for $r_{AB} = 1$, 0.01 , and 0.0001 , respectively. Each color shows the last hundred thousand particles to join the system.

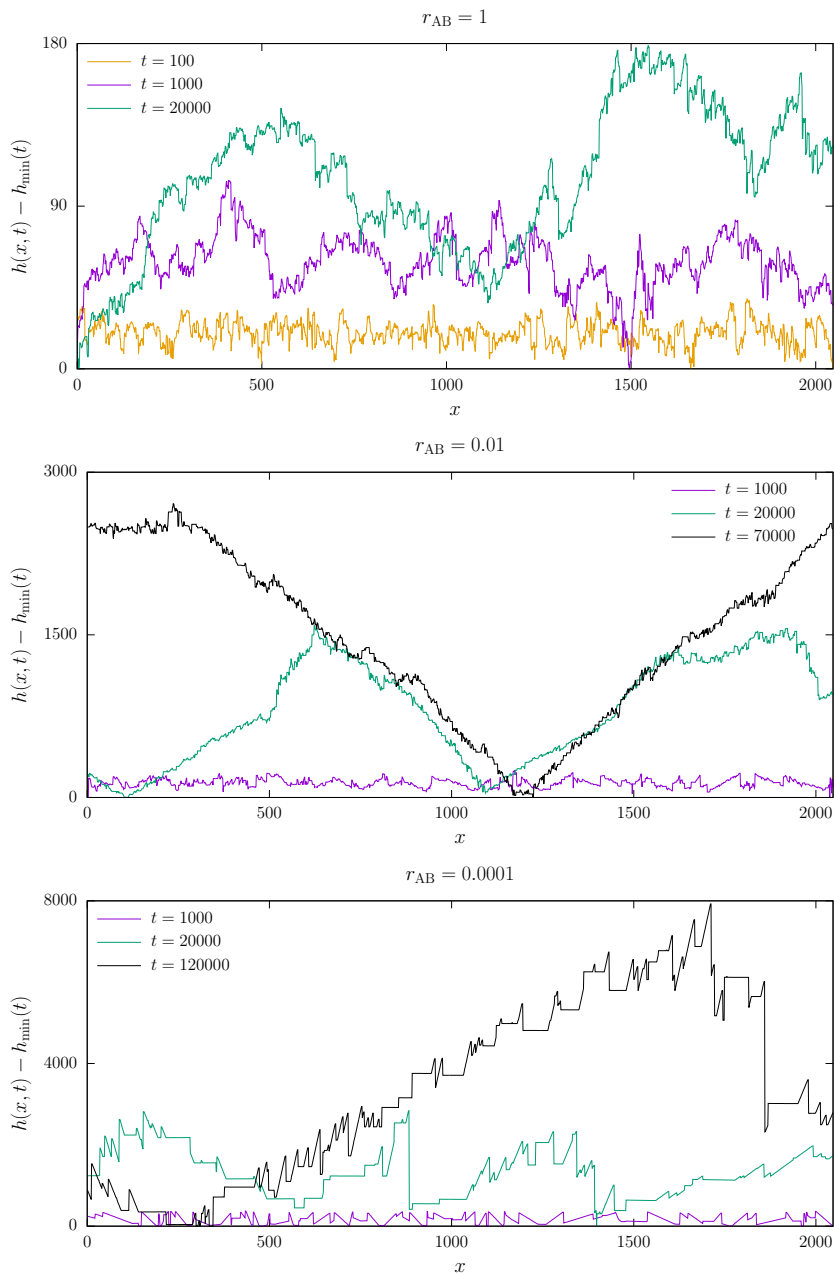


Figure 5.15: Temporal evolution of the height front $h(x, t)$ for $r_{AB} = 1$, 0.01, and 0.0001, top to bottom. The aggregates are the same as those in Fig. 5.14.

We have observed that significant jumps in front heights occur at times when the second slope of the $C_2(r, t)$ curves appears. This phenomenon is illustrated in Fig. 5.15, where we plot the time evolution of $h(x, t)$ under the same conditions (i.e., for the same r_{AB} values) as in Fig. 5.14. In this figure, we may observe that the front displays minor fluctuations at early times ($t \lesssim 1000$), none of them particularly noteworthy. At later times, on the contrary, these jumps occur, concurrent with the formation of macroscopic shapes. This effect is more pronounced when r_{AB} decreases, and is only apparent for sufficiently large values of L .

5.3.8 Front structure for $r_{AB} = 0$

As we have previously mentioned, the behavior of our model changes substantially for $r_{AB} = 0$. Firstly, the front velocity becomes zero for sufficiently long times under this parameter condition. Besides, prior to macroscopic pinning, the kinetic roughening of the front turns out to share many features with that of an unstable generalization of on-lattice ballistic deposition [151].

Indeed, for $r_{AB} = 0$, the front velocity drops to zero due to the selective growth of a few branches that span the entire lateral size of the system, which is unlike the behavior observed at long times for $r_{AB} > 0$. The unique structure of the particle aggregate for $r_{AB} = 0$ leads to a front with significantly large front derivative, or slope, at many locations. A similar morphology is observed for very small, but nonzero, r_{AB} values. An example of this phenomenon is shown in Fig. 5.16.

The growth model which generalizes on-lattice ballistic deposition [151] exhibits a pattern remarkably comparable to that observed in our own study for the $r_{AB} = 0$ situation. Specifically, while in standard BD particles are randomly deposited in a vertical direction at arbitrary locations, in Ref. [151] particles follow linear trajectories with a random inclination with respect to the x axis; this angle is chosen from a uniform distribution. Such a modification of BD is known to lead to a morphological instability [149, 152] inducing the formation of large columns. Indeed, in Ref. [151] the front exhibits numerous regions with high slopes, such that the probability distribution function for these slope values Δh , denoted as $P(\Delta h)$, decays

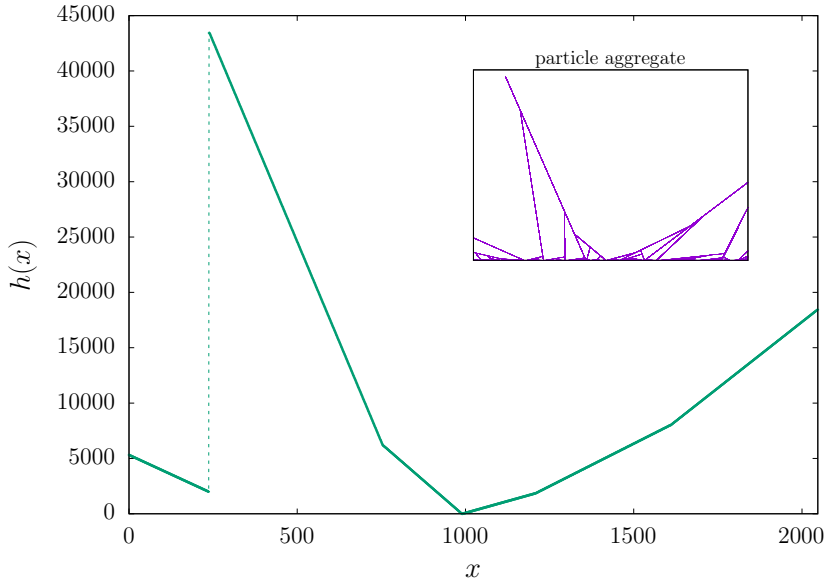


Figure 5.16: Sample front morphology obtained at $t = 130000$ for $r_{AB} = 0$. The main panel shows the front height $h(x, t)$ as points connected by a dashed line. Note the very different scales employed for the two axes. The corresponding particle aggregate is shown in the inset.

slowly as a power law. Specifically,

$$P(\Delta h) \sim 1/(\Delta h)^\gamma, \quad (5.4)$$

with an exponent γ that ranges between 1.6 and 2. For extremely large values of Δh , the distribution falls off significantly more quickly.

It was suggested that this behavior could be responsible for intrinsic anomalous scaling [151, 153]. Remarkably, the scaling exponents measured in Ref. [151] for this unstable BD model, namely, $\alpha \simeq 1.25$, $\alpha_{\text{loc}} \simeq 0.54$, $\beta \simeq 1$, and $z \simeq 1.25$, are close to those we presently obtain for the patchy colloid model for $r_{AB} = 0$ prior to pinning, namely, $\alpha \simeq 1.18$, $\alpha_{\text{loc}} \simeq 0.45$, $\beta \simeq 0.98$, and $z \simeq 1.18$. In view of this, we have computed the slope of the $P(\Delta h)$ histogram obtained herein for $r_{AB} = 0$; the results, shown in Fig. 5.17, are not so far from those reported in Ref. [151]. The same arguments presented in this reference may be then applied to account for the intrinsic anomalous scaling behavior observed for $r_{AB} = 0$. Quantitative differences with the unstable BD model [151] are probably induced by the

deviations of our slope histogram from the $P(\Delta h)$ function obtained for the latter, especially at the largest Δh values. Therefore, we conclude that this result may be indicative of a morphological instability analogous to that of oblique-incidence BD, to be responsible for the intrinsic anomalous scaling of the fronts of the colloidal aggregates formed for $r_{AB} = 0$.

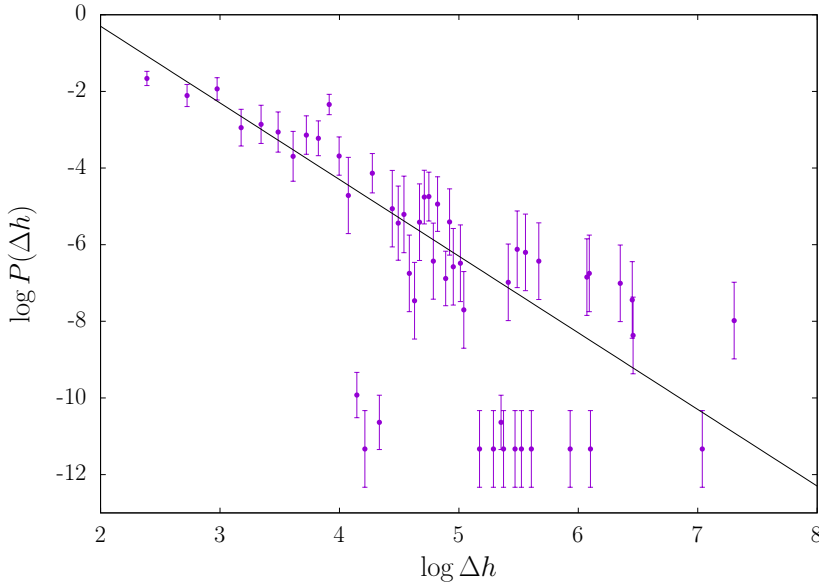
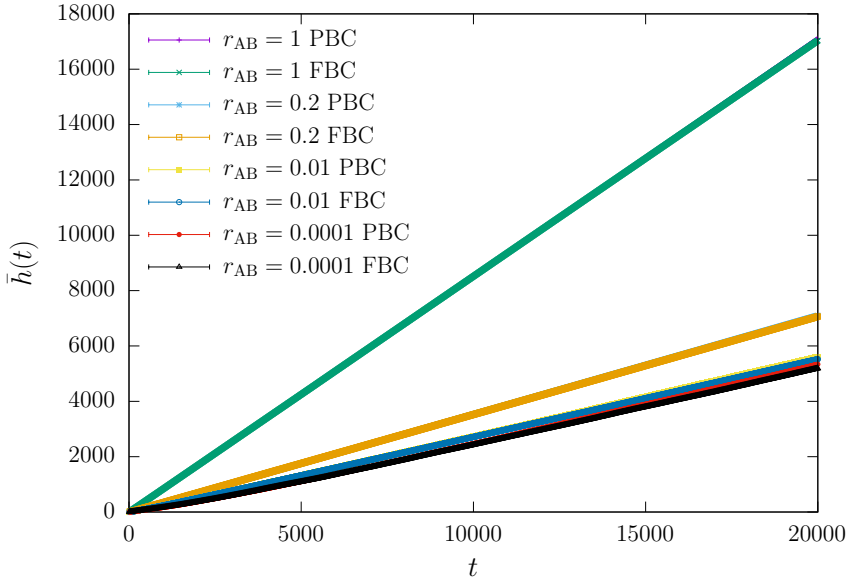


Figure 5.17: Slope histogram for the fronts obtained at $t = 130000$ for $r_{AB} = 0$. For comparison, the solid line corresponds to $P(\Delta h) \propto 1/(\Delta h)^2$.

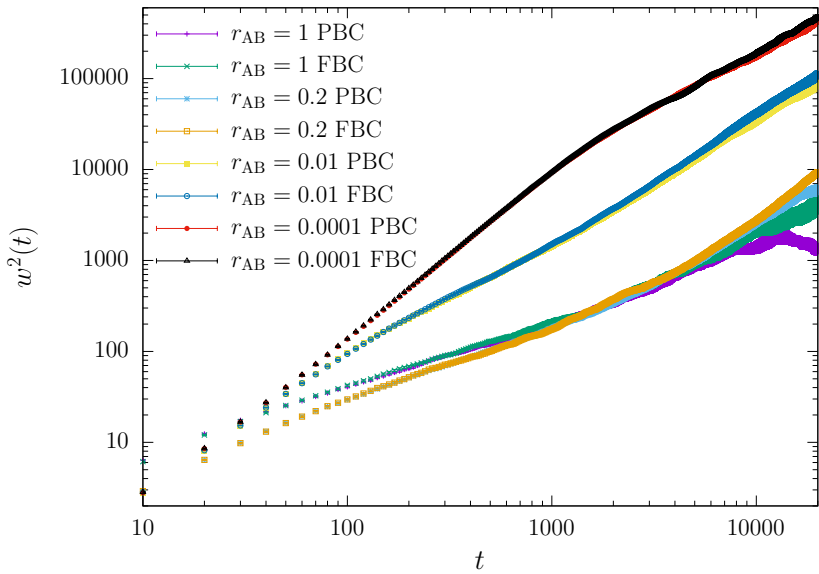
5.3.9 Free versus periodic boundary conditions

In order to examine how the boundary conditions affect the overall dynamic evolution of the system, we have calculated a range of quantities for various values of r_{AB} under identical conditions ($L = 2048$ and 20 iterations) using both FBC and PBC. The average front and the squared roughness as a function of time are shown in Figs. 5.18a and 5.18b, respectively.

The front evolution in PBC and FBC is almost the same, within error bars. However, the roughness curves exhibit variations at long times, which may result from greater front fluctuations at saturation under these circumstances. Nonetheless, the outcomes presented occur much earlier than those time intervals, so we do not anticipate any influence of the boundary conditions on our results.



(a) Mean front height vs. time.



(b) Squared roughness vs. time.

Figure 5.18: Mean front height and squared roughness as functions of time for values of r_{AB} as given in each legend, using FBC or PBC as indicated. For some sets of data, FBC data hide total or partially PBC results.

5.3.10 Off-lattice ballistic deposition

In Sec. 5.2, it was mentioned that the model described in Refs. [146, 147] should exhibit behavior similar to that of simple off-lattice ballistic deposition [149] in the $r_{AB} = 1$ limit, where the A and B poles become indistinguishable. However, due to the finite interaction range and alignment of particles after attachment, which are absent in off-lattice ballistic deposition, this model exhibits distinct behavior. This difference is evident in the front roughness of the patchy colloid model, as shown in Fig. 5.7. In this section we collect further results from numerical simulations carried out for off-lattice BD, in order to compare them with those presented for the patchy colloid model.

Figure 5.19 shows colloids aggregates for off-lattice BD and for patchy colloids model in the $r_{AB} = 1$ case, at the start of two simulations. By examining the figure, we can observe slight differences, including the existence of perpendicular branches generated by permissible directions in the $r_{AB} = 1$ scenario, resulting in a slightly less dense system.

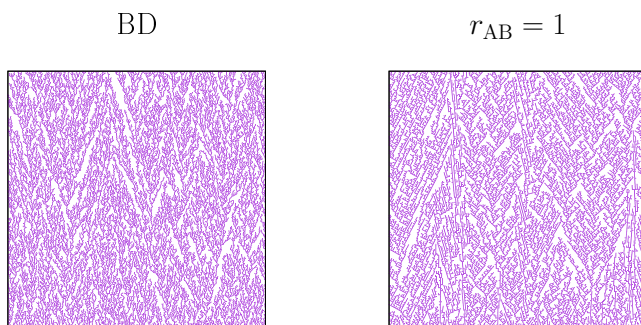


Figure 5.19: Morphologies of the colloidal aggregates for off-lattice BD model and patchy colloids model for $r_{AB} = 1$. The size of the simulations is $L = 2048$, but only the values of x within the range of 0 to 255 are displayed for easier viewing. Times range from the initial ones to final times for which the points of the morphologies fill the plots.

The correlation function $C_2(r, t)$ for off-lattice BD is shown in Fig. 5.20. In Sec. 5.3.4, it was noted that this function exhibits a standard scaling behavior that differs from the one displayed in Fig. 5.8a for the patchy colloids model for $r_{AB} = 1$. In line with this, the morphologies observed

after a long period of time (specifically, when $t = 20000$) in off-lattice BD show a smoother height front (see Fig. 5.21), in contrast to the $r_{AB} = 1$ case (see Fig. 5.14). For completeness, the scaling exponents computed for the off-lattice BD model are $z = 1.41(2)$ and $\alpha = 0.469(7)$, consistent with those reported elsewhere [149].

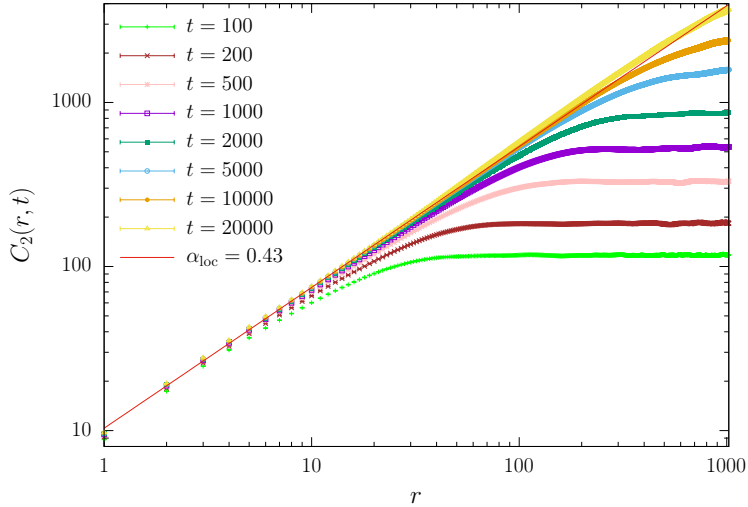


Figure 5.20: Front correlation function $C_2(r, t)$ vs. r for off-lattice BD. The solid line corresponds to fit to the power law $r^{2\alpha_{loc}}$ for $t = 20000$ and $r < 200$.

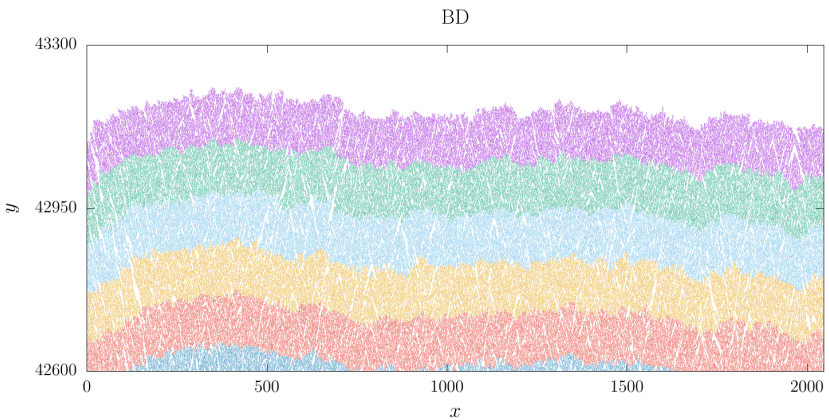


Figure 5.21: Morphology of a colloidal aggregate at the final time, $t = 20000$, for off-lattice BD. Each color shows the last hundred thousand particles to join the system.

5.4 Conclusions

We have revisited the model of “patchy” colloids for the coffee-ring effect developed by Dias *et al.* [145–147] through extensive numerical simulations extending their times, sizes, and values of r_{AB} . We have also used more realistic boundary conditions and an extended characterization in terms of correlation functions computed in the real and reciprocal spaces.

Firstly, the set of scaling exponents computed for each r_{AB} value are in fair agreement with those by Dias *et al.* for comparable simulation times and sizes. Deviations appear for longer times. Our findings support the observed KPZ kinetic roughening behavior for coffee-ring aggregates with large values of r_{AB} and intermediate times. By contrast, the α and β exponent values which were ascribed earlier to the QKPZ universality class are now seen to be crossover values limited to the intermediate-time evolution in a restricted range of r_{AB} values.

Taking into account our full set of results including very small $r_{AB} \geq 0$ and long times, the overall behavior seems already clear in Fig. 5.7. We can classify the behavior in terms of large or small r_{AB} , with an approximate boundary at $r_{AB} = 0.01$. For each value of this parameter, we have to distinguish between intermediate and long times.

For large $0.01 < r_{AB} \leq 1$ and intermediate times, exponent values are KPZ for $r_{AB} = 1$ and gradually increase (going through QKPZ values) for decreasing r_{AB} . However, at longer times β and α both increase substantially, even for the $r_{AB} = 1$ case, which hence differs from simple off-lattice BD.

For small $0 \leq r_{AB} \leq 0.01$, the intermediate times (recall Fig. 5.7) seem to be dominated by the scaling obtained for $r_{AB} = 0$, that has the largest value of β seen in our simulations. Note that the $r_{AB} = 0$ behavior is quite similar to that of unstable BD [151]. When the value of r_{AB} is small, the long time behavior shows smaller values of β (but still large) which are not far from those seen for large r_{AB} and long times.

The system intermediate dynamics vary depending on the value of r_{AB} . For $0 < r_{AB} \leq 0.01$, the system behaves similarly to the $r_{AB} = 0$ case, and this similarity persists for longer times as r_{AB} decreases. In this range of r_{AB} values (including $r_{AB} = 0$), we observed intrinsic anomalous scaling [88–90],

which is a more complex form of dynamic scaling compared to the simpler Family-Vicsek Ansatz [11, 51]. On the other hand, for $r_{AB} > 0.01$, the intermediate-time behavior is consistent with that of 1D KPZ and there is no evidence of intrinsic anomalous scaling. Within this range, the exponents are similar to those of QKPZ, as reported elsewhere [146, 147].

For long times and with large lattice sizes, we have found that macroscopic shapes significantly impact the system dynamics, including the corresponding scaling exponents, for all $0 < r_{AB} \leq 1$. Our results suggest that the critical behavior reported by Dias *et al.* [147], especially the 1D QKPZ exponents for lower values of r_{AB} , is influenced by the macroscopic shapes that ultimately form. The large values of β occur simultaneously with front morphologies that are characterized by significant slopes and large macroscopic shapes. This behavior is similar to a morphologically unstable behavior, which could be linked to the finite iteration range and colloid attachment rules.

Note that for models with time-dependent noise, like these for patchy colloids, a value of $\beta > 1/2$ typically implies a morphological instability, since $\beta = 1/2$ corresponds to purely random deposition of particles (see Sec. 1.3) [11, 149]. In some growth systems with time-dependent noise, there is a transition over time from, for instance, KPZ scaling behavior to a regime where much larger effective exponent values are observed. This crossover phenomenon has been observed in other systems, such as diffusion-limited growth systems [154].

For example, as it has been observed in recent experiments and models [155], bacterial colonies that grow in a certain parameter range known to exhibit KPZ-like (also called Eden-like) [149] behavior change over time from a compact state with relatively small fluctuations to a branched structure with very large slopes. During this process, the growth exponent increases from $\beta \simeq 0.47$ at early times to $\beta \simeq 0.93$ at long times [155], similar to the change observed for a value such as $r_{AB} \simeq 0.1$. This behavior is due to a morphological instability present in such diffusion-limited systems [154, 156], where protrusions on the front grow faster than depressions due to differences in exposure to diffusive fluxes. This instability can be triggered during the evolution of the system, resulting in a change in the scaling behavior as in Ref. [155].

In the patchy colloids model, transport is not constrained by diffusion. Nevertheless, the model incorporates an unstable mechanism due to the finite interaction range and the step of colloid alignment. This is evident when comparing the case where $r_{AB} = 1$ with off-lattice BD. This mechanism operates for all values of r_{AB} and can explain the scaling behavior as well as the macroscopic front shapes (which are not unlike morphologies seen for diffusion-limited systems) that occur over extended periods.

Our finding shows a discontinuous pinning-depinning phase transition at $r_{AB} = 0$. Particularly, there is a discontinuity in the velocity as $r_{AB} \rightarrow 0^+$, with $v(r_{AB} \rightarrow 0^+) \neq v(r_{AB}) = 0$. The choice of proper boundary conditions was found to be of paramount importance for $r_{AB} = 0$, as only the use of free boundary conditions allows us to elucidate the phase transition.

In numerical simulations [146, 147], Dias *et al.* observed a non-zero front velocity for all values of $0 < r_{AB} \leq 1$. However, they also noted that the aggregate interface was not well-defined for $r_{AB} = 0$. At intermediate values of r_{AB} , they reported a crossover between the KPZ and QKPZ regimes, which could be attributed to the competition between two mechanisms: decreasing r_{AB} hinders binding to B patches, favoring the growth of A-A chains and increasing the availability of B sites, which compensates for the decrease caused by the low r_{AB} value. Consequently, Dias *et al.* proposed that the pinning transition occurred not at a single critical value of $r_{AB,c}$, but within a finite range of r_{AB} values. This behavior differs from that of the QKPZ equation, in which the depinning transition occurs at a specific value of the control parameter and not over a complete range of values. Additionally, during this transition, the average velocity of the front remains at zero. By contrast, our simulations, which employ FBC, have enabled us to identify an abrupt pinning transition precisely at $r_{AB} = 0$. The scaling exponents of QKPZ are effective values in this case. Notably, the development of macroscopic shapes at long times is not reliant on the choice of boundary conditions.

The study of correlation functions, which expands previous numerical work on this model, enables us to better understand the occurrence of intrinsic anomalous scaling for small r_{AB} , as well as the existence of different scaling behaviors at small and large distances for long times, which correspond to the emergence of macroscopic shapes. Anomalous scaling is a

well-known phenomenon observed in various experimental systems, as well as in continuum and discrete models where morphological instabilities are present [89, 90]. This reinforces our interpretation that a morphological instability dominates the large behavior of the patchy colloid model, especially in the context of the colloidal Matthew effect, where quenched disorder is not relevant and the model mimics the same behavior when the r_{AB} decreases. This is consistent with the experiments of Yunker *et al.* [137, 140] and was to be expected, as the relevance of the colloidal Matthew effect increases with the colloid eccentricity.

Chapter 6

Contact process fronts

The results present presented in this chapter has been published as B. G. Barreales, J. J. Meléndez, R. Cuerno, and J. J. Ruiz-Lorenzo, Phys. Rev. E 108, 044801 (2023).

In this chapter we study the interface representation of the contact process at its directed-percolation critical point, where the scaling characteristics of the interface can be related to those of the original particle model. Notably, this behavior is intrinsically anomalous and more intricate than what is explained by the conventional Family-Vicsek dynamic scaling Ansatz for surface kinetic roughening. We expand on a previous numerical study by Dickman and Muñoz [157] to fully characterize the kinetic roughening universality class for interface dimensions $d = 1, 2$, and 3 . Beyond determining the values of scaling exponents, we provide a detailed characterization of the fluctuations in the interface through their probability density function and covariance. These fluctuations exhibit universal properties that bear a qualitative resemblance to those recently observed in other significant universality classes of kinetic roughening, such as the KPZ class. However, we find that, while the interface covariance for $d = 1$ appears to compare well with that of the 1D KPZ universality class, specifically the Airy_1 covariance, such agreement is not evident in terms of the fluctuation PDF or the scaling exponents.

6.1 Introduction

Directed percolation is one of the most studied and interesting non-equilibrium universality classes in critical phenomena [61, 62]. A wide range of physical systems, such as chemical reactions, the spread of epidemics, phase transitions in particle systems, and many others, exhibit behavior that falls within this universality class [58–60]. Further details are provided in Chapter 2.

A very interesting particle model in this context is the contact process (see Sec. 2.5), which hosts a phase transition to an absorbing state, with the transition being in the universality class of DP. The CP model was introduced to describe the spread of epidemics without immunization [73, 74]. Due to the existence of analytical results for this model (albeit in the absence of an exact solution for it), it is the most widely chosen realization to study and characterize DP.

A fruitful direct mapping can be established between the CP and an interface model, as elucidated in Ref. [157] and other works mentioned therein. This mapping is characterized by the fact that the absorbing state of the particle model, representing a complete absence of activity, concurs with the state of arrested overall motion of the corresponding interface, commonly known as pinning. Precisely, at the critical point, the scaling properties of the interface can be linked to those of the original particle model, offering insight into interface dynamics at an absorbing-state critical point.

This connection has been exploited by Dickman and Muñoz [157] to investigate the ensuing kinetic roughening properties of the CP for interface dimensions $d = 1, 2$, and 3 (that is, below the upper critical dimension $d_c = 4$), where nontrivial scaling is expected. Interestingly, the result of Ref. [157] is that intrinsic anomalous scaling occurs for all these values of d , and moreover that (some of) the kinetic roughening exponents are directly given by those describing the decay of the order parameter at the phase transition point.

In relation to kinetic roughening, while interface fluctuation statistics have been extensively studied for universality classes that satisfy the FV scaling (such as KPZ), there is a lack of research on systems that exhibit anomalous scaling asymptotically. To the best of our knowledge, there

are relatively few studies addressing fluctuation statistics in such systems [35, 158, 159], and none of them specifically investigates the d -dependent behavior of these fluctuations. It is important to note that the so-called intrinsic anomalous scaling has been argued (based on perturbative arguments) not to be asymptotic for systems with local interactions in absence of morphological instabilities and/or quenched noise [160]. Hence some additional conditions are expected for it to occur.

In this chapter, we revisit the work by Dickman and Muñoz [157] with several primary objectives. First, we want to investigate if the PDF and covariance of interface fluctuations, across the above-mentioned related to DP, remain universal for all $d < d_c$. The universality in the fluctuation statistics has been observed, for instance, in the KPZ class. It is noteworthy that our dynamic scaling assumption does not adhere to the FV condition and the behavior of intrinsic anomalous scaling with interface dimension has been very scarcely assessed in the literature (see, for example, Refs. [161, 162]). Therefore, in order to achieve the above objective, we conduct a comprehensive assessment of the dynamic scaling assumption and scaling exponents reported in Ref. [157]. We present more explicit data regarding the behavior of various observables under study, especially for dimensions $d \geq 2$. Moreover, we aim to assess possible connections between the thus determined fluctuation statistics and those of important reference cases like the 1D KPZ universality class. We will find both similarities and differences. At this, note also that DP and KPZ are two paradigmatic universality classes for non-equilibrium systems [61, 62] which feature a subtle interplay, as exemplified by the depinning transition of the KPZ equation with quenched disorder (see Sec. 1.4).

6.2 Model and simulation details

The contact process, introduced in Sec. 2.5, was originally defined as a particle model as follows: each site of a d -dimensional integer lattice \mathbb{Z}^d can either be empty or occupied by a particle. The dynamics consists of particles being created at empty sites at a rate proportional to the number of occupied nearest neighbors, and being annihilated at a constant rate normalized to 1. If we denote the creation rate by λ , a critical value λ_c exists

where a phase transition occurs to an empty absorbing state. This process can be interpreted as a model for the spread of an infection, where the occupied sites represent infected individuals and the empty sites represent healthy ones [61, 62, 73, 74].

The numerical simulations have been carried out on a lattice with size L^d where d is the dimension ($d = 1, 2$ or 3), using PBC. A binary variable called s was used to track the occupation (or activity) of a site of the lattice in such a way that, at time t , each site with a vector position $\mathbf{x} \in \mathbb{Z}^d$ may either have a particle on it [$s(\mathbf{x}, t) = 1$] or be empty [$s(\mathbf{x}, t) = 0$]. Initially, all sites are occupied. At each simulation step an occupied site is randomly chosen and two processes, namely creation and annihilation of a particle, are possible. Creation occurs with probability $p = \lambda/(1 + \lambda)$; in this case, one of the $2d$ nearest neighbors of the chosen site is selected and, if it is empty, a new particle is created in this position. On the other hand, annihilation occurs with probability $1 - p$; the particle of the chosen site being removed. The time increment at each step is $\Delta t = 1/N_{\text{occ}}$ where N_{occ} is the number of occupied sites.

As mentioned above, here will study the associated interface problem. To connect the particle model with an interface model, we define the front (or interface) at each lattice site at time t as

$$h(\mathbf{x}, t) = \int_0^t s(\mathbf{x}, t') dt'. \quad (6.1)$$

Therefore, the local height $h(\mathbf{x}, t)$ represents the interval of time up to t that the lattice site \mathbf{x} has been occupied; that is, the front quantifies the total activity at each node up to time t . Examples of fronts from our $d = 1$ simulations are shown in Fig. 6.1. Particularly, in this way, the absorbing state of the particle model, characterized by the global absence of activity, corresponds to an arrested or pinned interface.

We have carried out simulations for systems in one, two, and three dimensions; all of them were performed at the critical value of the parameter λ_c , whose values for each dimension are collected in Table 2.2. The parameters employed in our simulations are listed in Table 6.1. In each case, the maximum simulation time t_{max} was chosen in such a way that approximately half of the runs survived and had not entered the absorbing state before this time (note that, for a sufficiently large t , the system will have entered the

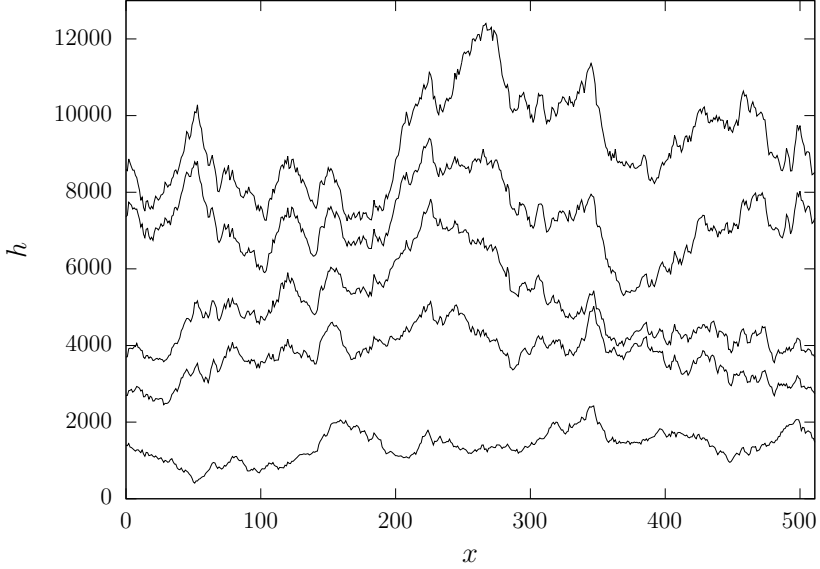


Figure 6.1: Local front or height profiles $h(x, t)$ from numerical simulations of a one-dimensional system with $L = 512$. Each line corresponds to a different time (bottom to top): $t = 5000, 15000, 25000, 35000,$ and 45000 . All units are arbitrary.

Table 6.1: Parameter values for CP numerical simulations.

d	L	t_{\max}	runs
1	512	60×10^3	2000
	1024	185×10^3	2000
	2048	530×10^3	2000
	4096	1600×10^3	2000
	8192	4000×10^3	2000
2	128	20×10^3	500
	256	50×10^3	500
	512	200×10^3	498
3	16	1×10^3	100
	32	3.5×10^3	100
	64	15×10^3	100
	128	40×10^3	20

steady state). For reference, one run in three dimensions and $L = 128$ takes approximately one month in one of our computer clusters (one node has 36 Intel Zeon Gold 6240 CPUs, each with 18 cores and operating at 2.60 GHz).

6.3 Results

To provide reference values for subsequent results, Table 6.2 presents the critical exponents of DP that will be relevant to our findings. These are the exponent α_ρ of Eq. (2.3) (which we will refer to as θ in this chapter) and z , which are listed in Table 2.1. Alongside these values, since we revisit the work of Dickmann and Muñoz [157], Table 6.2 shows the kinetic roughening exponents α , β , and α_{loc} as obtained therein, and the maximum value of L (L_{max}) employed.

Table 6.2: Critical exponents of the DP universality class from Table 2.1 where $\theta \equiv \alpha_\rho$, kinetic roughening exponents α , β , and α_{loc} as obtained in Ref. [157], and maximum value of L (L_{max}) employed in this reference, for the values of d considered in our work.

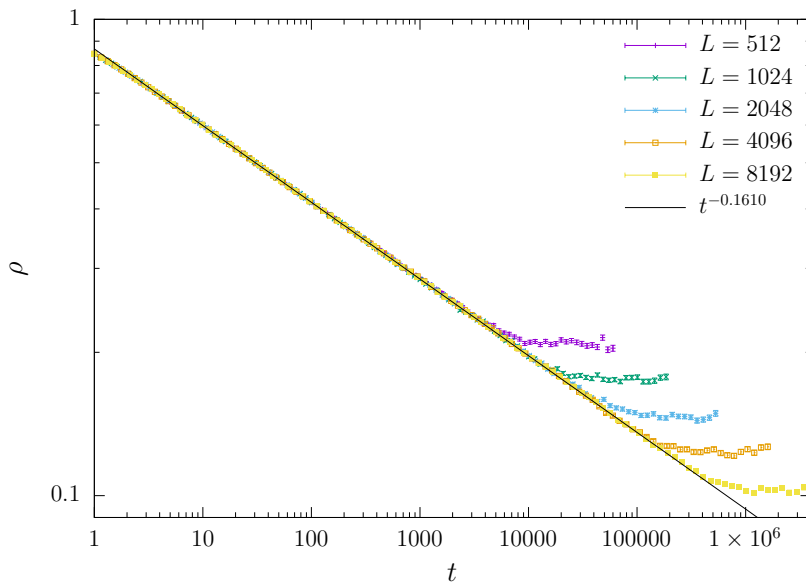
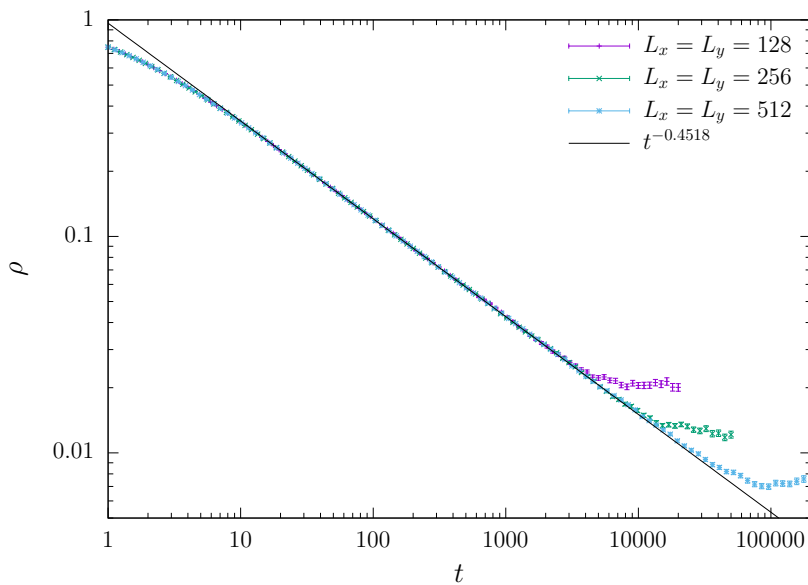
d	θ	z	α	β	α_{loc}	L_{max}
1	0.159464(6)	1.580745(10)	1.33(1)	0.839(1)	0.63(3)	5000
2	0.4505(10)	1.7660(16)	0.97(1)	0.550(5)	0.385(5)	256
3	0.732(4)	1.901(5)	0.51(1)	0.27(1)	0.09(2)	50

6.3.1 Density and roughness: exponents θ and β

The order parameter for the phase transition in the CP is the global particle density $\rho(t)$. At the critical point, this function decays as a power law

$$\rho(t) \sim t^{-\theta}, \quad (6.2)$$

with an universal d -dependent critical exponent θ (see Table 6.2). This behavior is the same one as reported in Eq. (2.3) in the context of DP, where $\alpha_\rho \equiv \theta$. The density $\rho(t)$ for systems of various sizes in one, two, and three dimensions are shown in Fig. 6.2. Fitting the data to Eq. (6.2) allows for the computation of the exponent θ , which is presented in Table 6.3.

(a) Particle density for $d = 1$.(b) Particle density for $d = 2$.

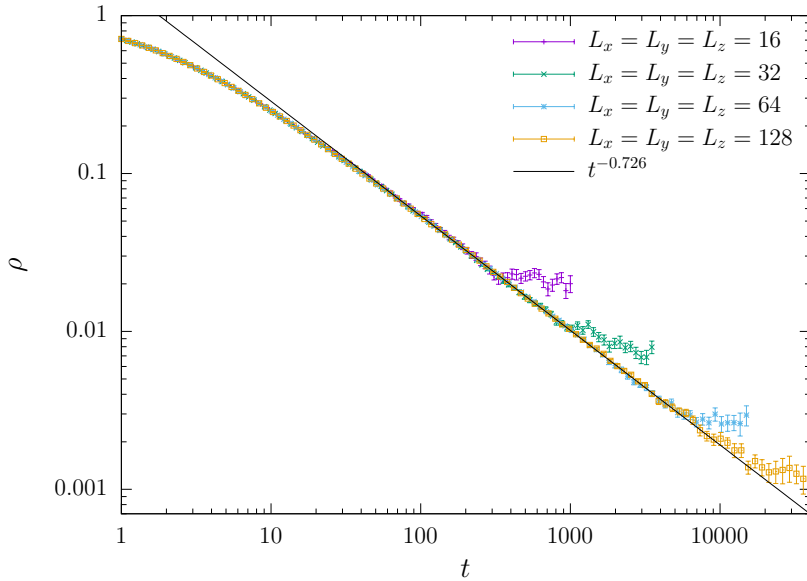
(c) Particle density for $d = 3$.

Figure 6.2: Particle density versus time for different dimensions. The solid lines represent the scaling law $t^{-\theta}$ for the largest size.

Table 6.3: Exponents θ , β , z , α , and α_{loc} for $d = 1, 2$ and 3 , as obtained in our simulations. The size of the system is L^d in each case.

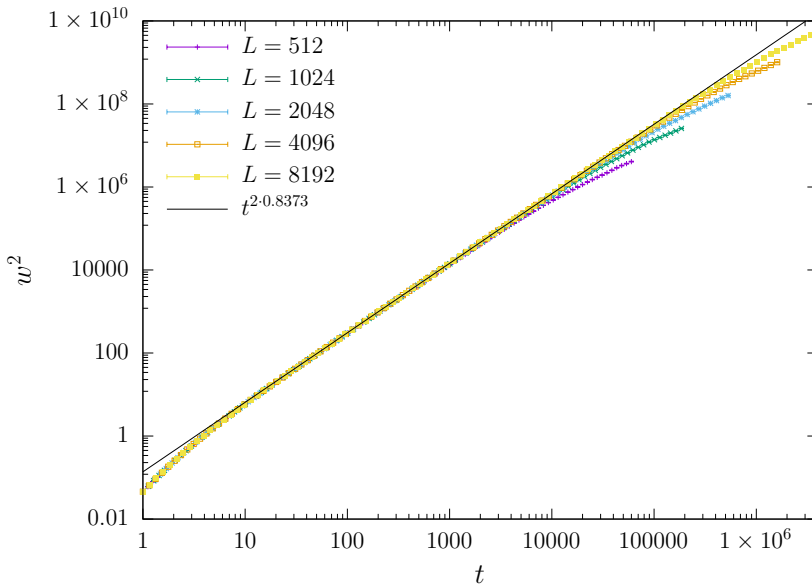
d	L	θ	β	z	α	α_{loc}
1	512	0.1595(6)	0.8195(18)	1.589(13)	1.341(8)	0.624(8)
	1024	0.1610(3)	0.825(2)	1.587(8)	1.336(6)	0.631(6)
	2048	0.1608(2)	0.8317(17)	1.608(10)	1.343(7)	0.636(8)
	4096	0.1607(3)	0.8354(7)	1.577(4)	1.328(3)	0.644(3)
	8192	0.1610(2)	0.8373(5)	1.573(3)	1.324(2)	0.644(2)
2	128	0.4489(4)	0.5440(13)	1.85(2)	1.026(9)	0.430(9)
	256	0.4515(7)	0.5452(14)	1.793(9)	0.988(6)	0.440(6)
	512	0.4518(4)	0.5461(6)	1.765(8)	0.970(7)	0.453(7)
3	64	0.714(4)	0.292(3)	2.20(5)	0.683(14)	0.188(15)
	128	0.726(4)	0.288(3)	2.12(14)	0.62(4)	0.17(4)

On the other hand, the interface of the particle system is defined by the height variable of Eq. (6.1), which measures the activity at each site until the given time. As an example, Fig. 6.1 shows the interface growing over time in a one-dimensional particle system. In order to characterize this interface, we compute the squared front roughness $w^2(t)$ for various sizes and dimensions, as shown in Fig. 6.3. The growth exponent β is then calculated from Eq. (3.4); these results are shown in Table 6.3. Note that Figs. 6.2 and 6.3 show a transient region in two and three dimensions, which essentially does not appear in one dimension.

Our results for θ and β are consistent with the values (see Table 6.2) and with the scaling relation $\beta = 1 - \theta$ reported in Ref. [157]. As argued therein, given Eq. (6.2) in CP, the mean height $\bar{h}(t)$ obeys

$$\bar{h} = \int dt \rho \sim \int dt t^{-\theta} \sim t^{1-\theta}. \quad (6.3)$$

The front roughness is defined as the standard deviation of the local height values, so that $w^2 \sim \bar{h}^2$; comparison with the kinetic roughening behavior of Eq. (3.4) implies $\beta = 1 - \theta$. Finally, note that our numerical results agree with improved consistency as L increases.



(a) Squared front roughness for $d = 1$.

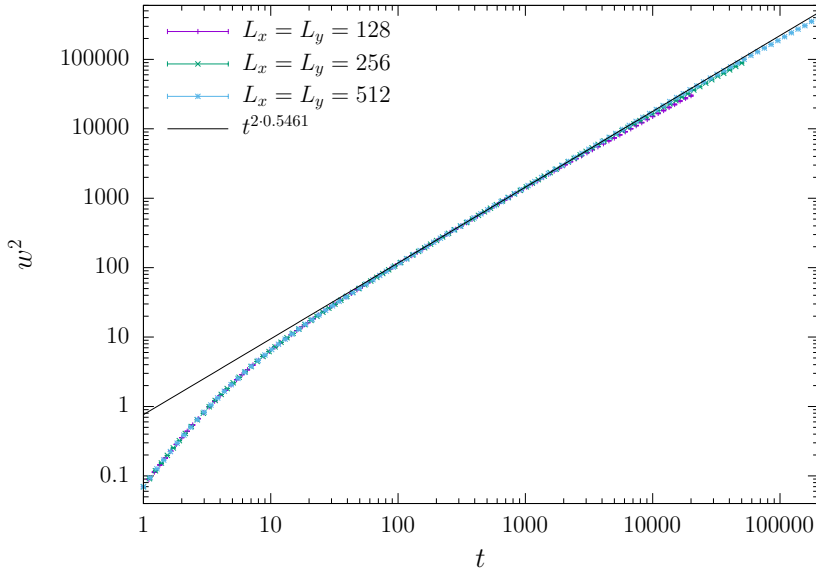
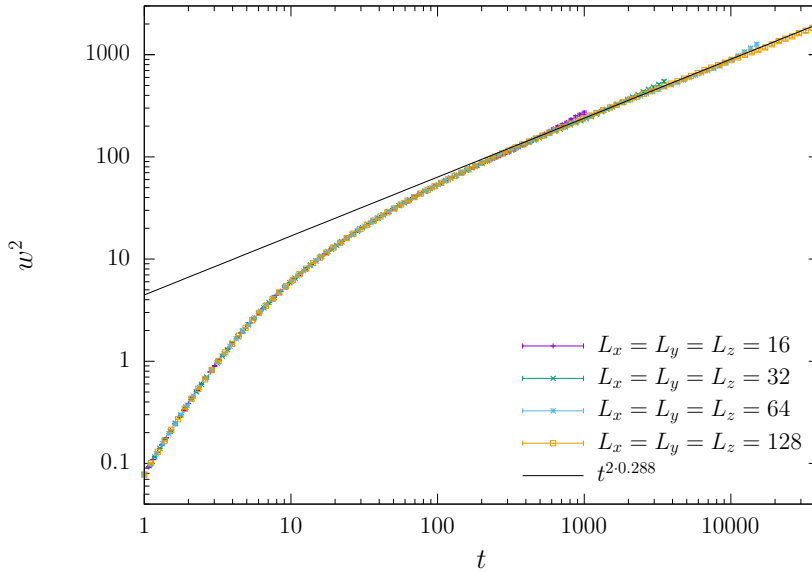
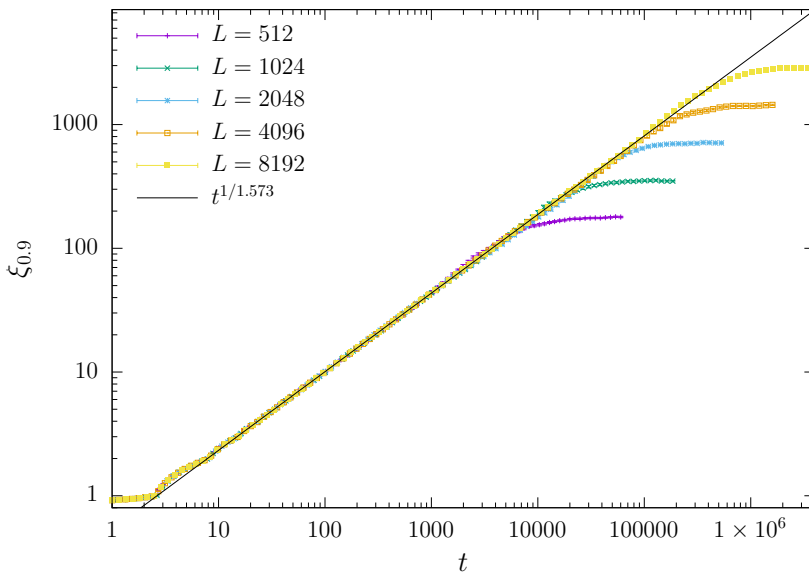
(b) Squared front roughness for $d = 2$.(c) Squared front roughness for $d = 3$.

Figure 6.3: Squared front roughness versus time for different dimensions. The solid lines represent the scaling law $t^{2\beta}$ for the largest size.

6.3.2 Front correlation length: exponents α and z

We next compute the correlation length $\xi_{0.9}(t)$ as the position r for which the correlation function $C_2(r, t)$ reaches 90% of its value at the plateau, as explained in Sec. 3.1. The correlation length can be plotted versus time (see Fig. 6.4), and fitted to Eq. (3.6) to obtain the dynamic exponent z . Likewise, Fig. 6.5 shows the height-difference correlation function at the plateau, $C_{2,p}(t)$, against the correlation length, in order to measure the exponent α according to Eq. (3.14). The resulting values of z and α are collected in Table 6.3.

To ensure the accuracy of our results, we can use the scaling relation that relates the exponents α , β , and z . Specifically, we can calculate β using $\beta = \alpha/z$. This value of β can then be compared with the growth exponent measured from the front roughness, denoted as β_w in this paragraph. Our results show that the values of β obtained for different dimensions d and system sizes L are consistent with β_w within the uncertainty intervals. For example, in the case of $d = 1$ and $L = 8192$, we obtain $\beta = \alpha/z = 0.842(2)$, which agrees with $\beta_w = 0.8273(5)$ within two standard deviations. Similarly, for $d = 2$ and $L = 512$, we get $\beta = \alpha/z = 0.550(5)$, which is consistent with



(a) Correlation length for $d = 1$.

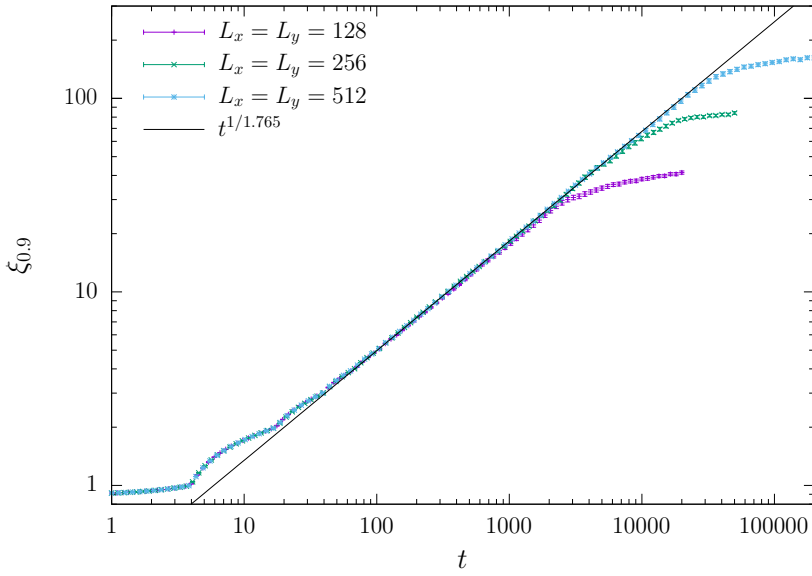
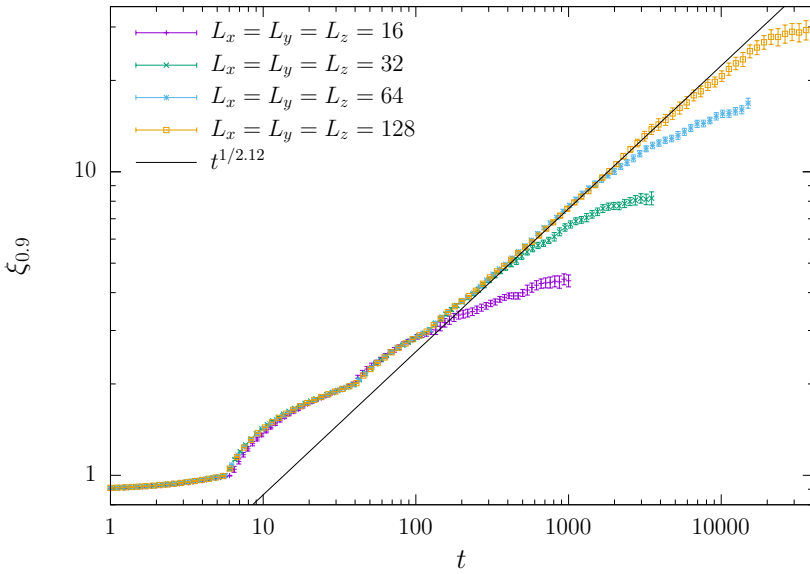
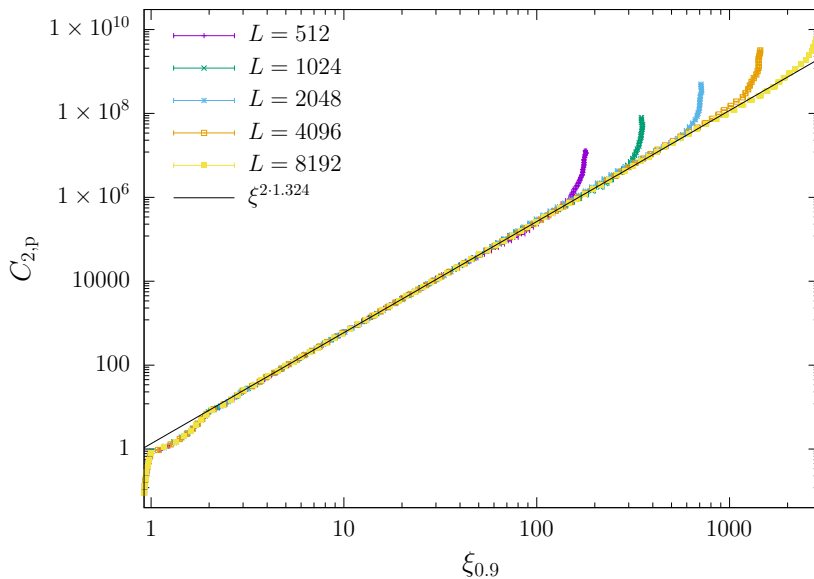
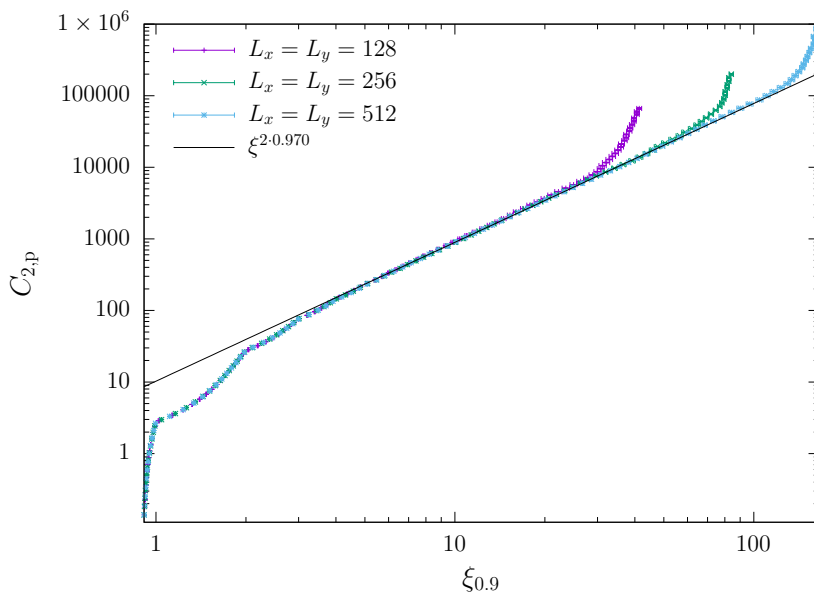
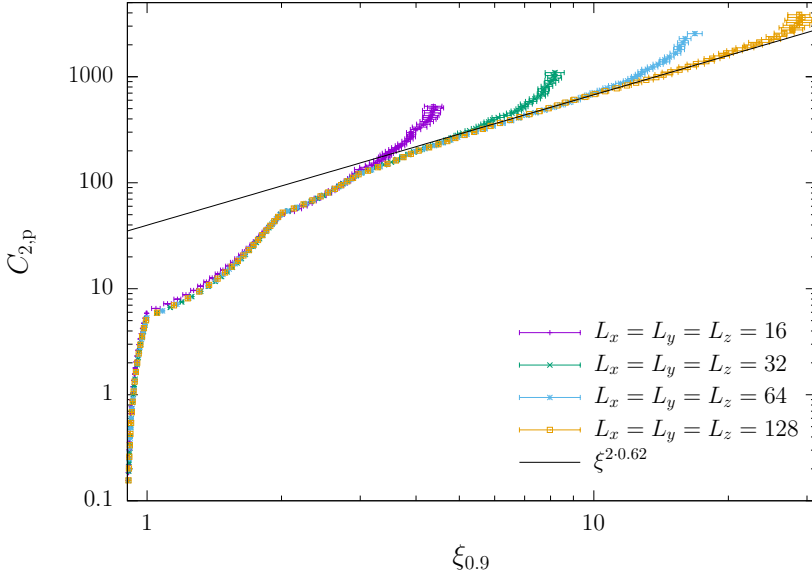
(b) Correlation length for $d = 2$.(c) Correlation length for $d = 3$.

Figure 6.4: Correlation length $\xi_{0.9}(t)$ versus t for $d = 1, 2$ and 3 from top to bottom. The solid lines correspond to the fit $t^{1/z}$ for the largest size in each case.

(a) $C_{2,p}(t)$ vs. $\xi_{0.9}(t)$ for $d = 1$.(b) $C_{2,p}(t)$ vs. $\xi_{0.9}(t)$ for $d = 2$.



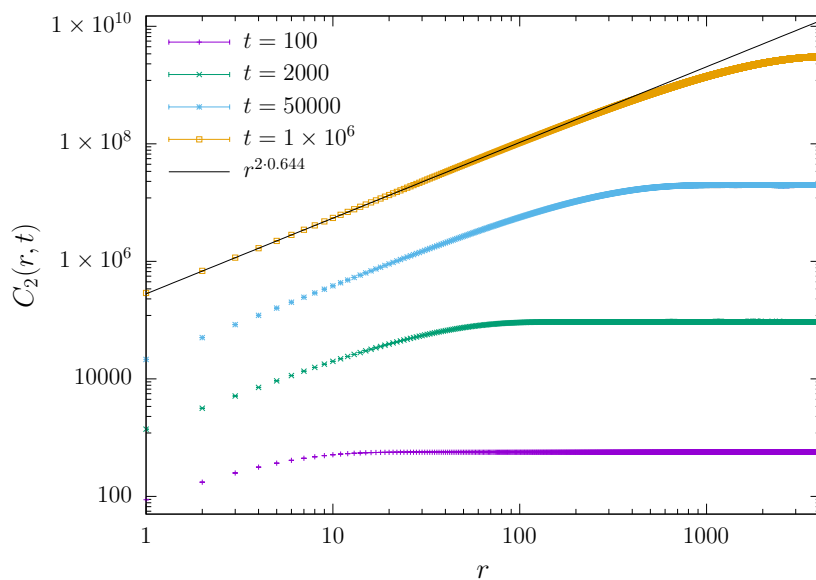
(c) $C_{2,p}(t)$ vs. $\xi_{0.9}(t)$ for $d = 3$.

Figure 6.5: Correlation function at the plateau, $C_{2,p}(t)$, vs. $\xi_{0.9}(t)$ for $d = 1, 2$ and 3 , top to bottom. The solid lines correspond to the fit $C_{2,p} \sim \xi_{0.9}^{2\alpha}$ for the largest size.

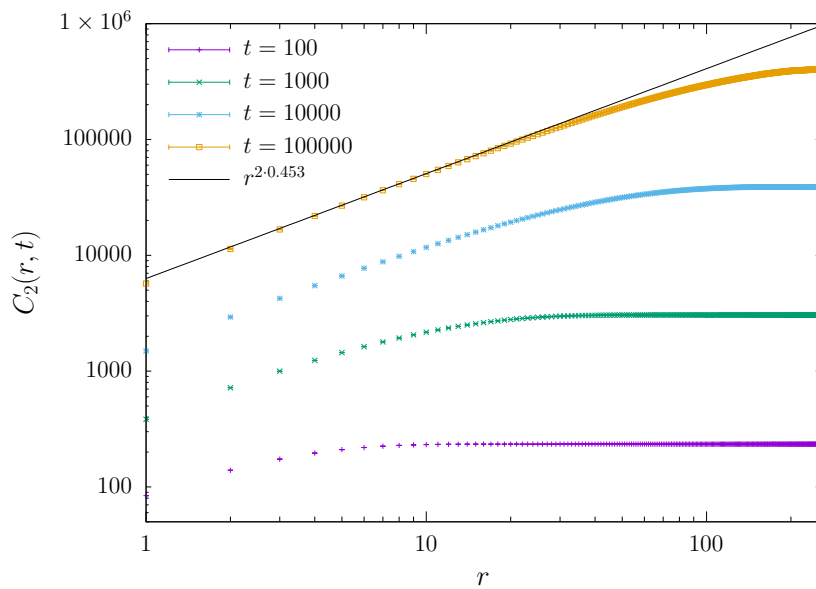
$\beta_w = 0.5461(6)$ within the uncertainty interval. Finally, for $d = 3$ and $L = 128$, we find $\beta = \alpha/z = 0.29(3)$, which agrees well with $\beta_w = 0.288(3)$. Our results are in line with those reported in Ref. [157], with the largest differences occurring for $d = 3$, where our values for α and z are 2.9 and 1.5 standard deviations away from those reported in that reference.

6.3.3 Height-difference correlation function

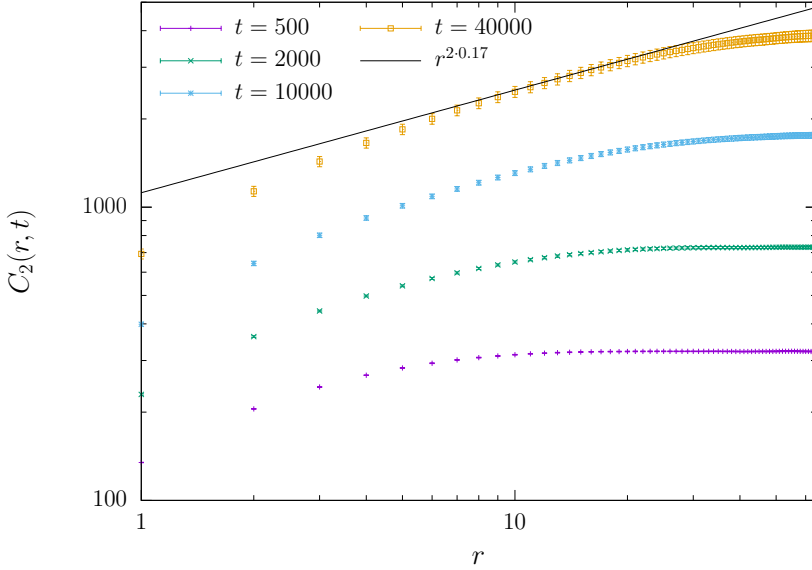
The height-difference correlation function $C_2(r, t)$, which provides information on the local behavior of the front scaling, is shown in Fig. 6.6 for $d = 1, 2$ and 3 and various times, with the largest system size L chosen for each dimension. We notice that, regardless of the dimension, the $C_2(r, t)$ curves for different times shift upwards systematically as time increases and do not overlap for any value of r . This is indicative of the occurrence of anomalous scaling, which may stem from various causes as reported in Sec. 3.1.



(a) Height-difference correlation function for $d = 1$ and $L = 8192$.



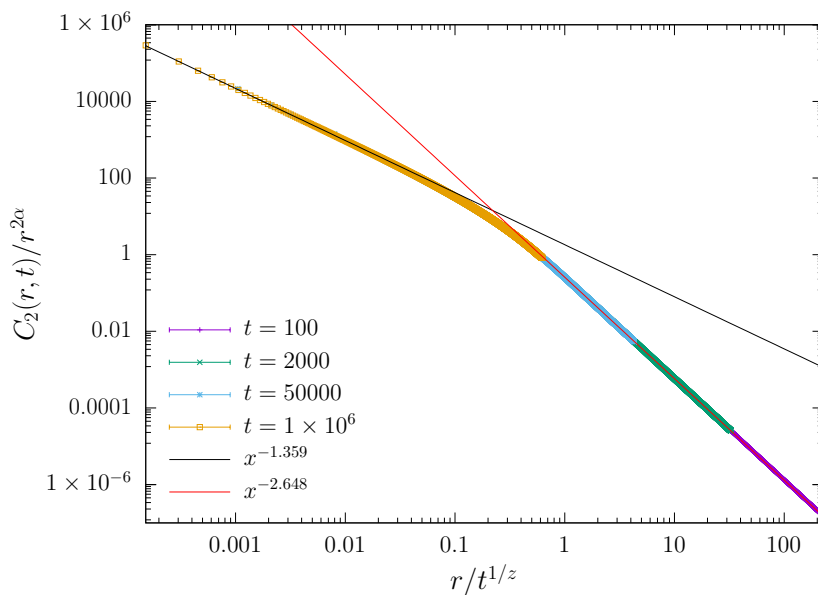
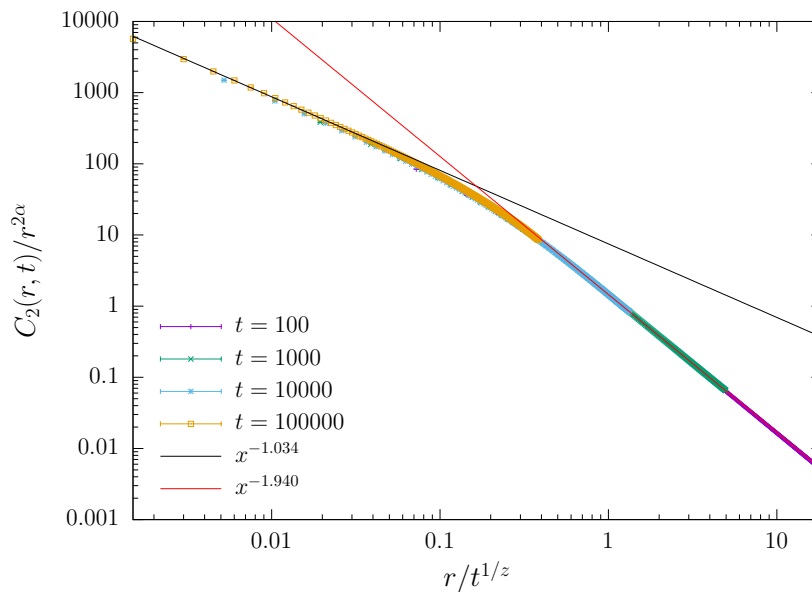
(b) Height-difference correlation function for $d = 2$ and $L = 512$.

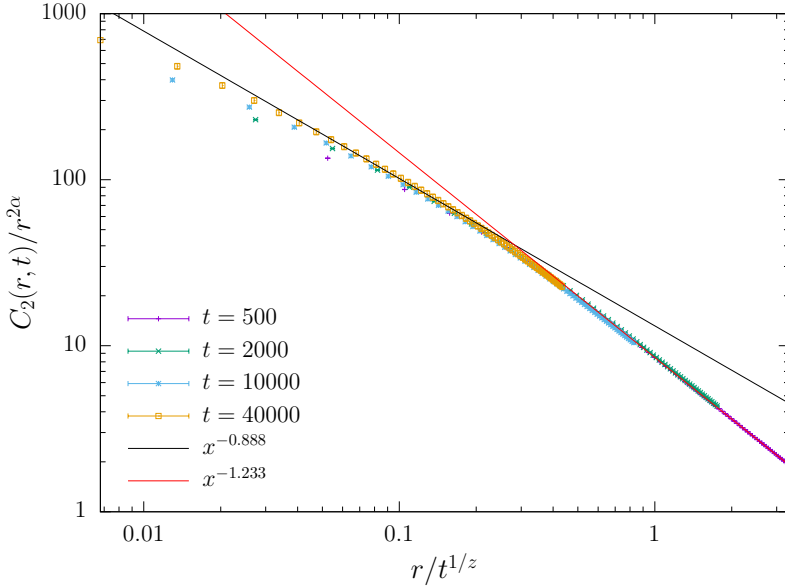


(c) Height-difference correlation function for $d = 3$ and $L = 128$.

Figure 6.6: $C_2(r, t)$ vs. r for different values of time, as indicated the legends, for different dimensions. The solid lines are proportional to $r^{2\alpha_{\text{loc}}}$.

If anomalous scaling occurs, one can calculate an additional roughness exponent, α_{loc} (see Eq. (3.16) and below). By using our estimates for α and z , we plot $C_2(r, t)/r^{2\alpha}$ against $r/t^{1/z}$ for each dimension in Fig. 6.7. According to Eq. (3.16), $\alpha' = \alpha - \alpha_{\text{loc}}$ can be estimated for small arguments of the scaling function, from which we obtain the value of α_{loc} shown in Table 6.3. The values of α_{loc} show slight variation when L is changed, but we attribute this difference to the limited size of our systems. The observed behavior is considered to be intrinsically anomalous scaling because $\alpha \neq \alpha_{\text{loc}}$ while $\alpha_{\text{loc}} < 1$ [88–90]. To reinforce this conclusion, we will study the structure factor and the gradient of the front in the following sections.

(a) Height-difference correlation function for $d = 1$ and $L = 8192$.(b) Height-difference correlation function for $d = 2$ and $L = 512$.



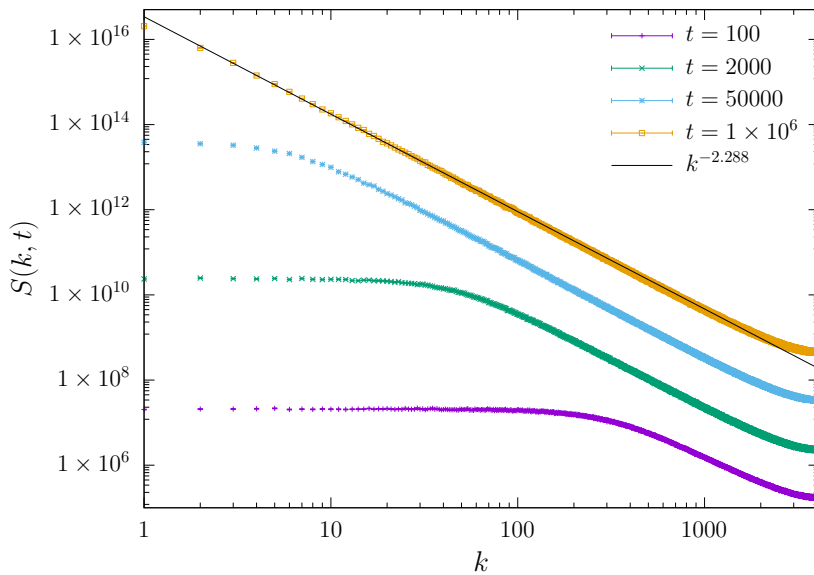
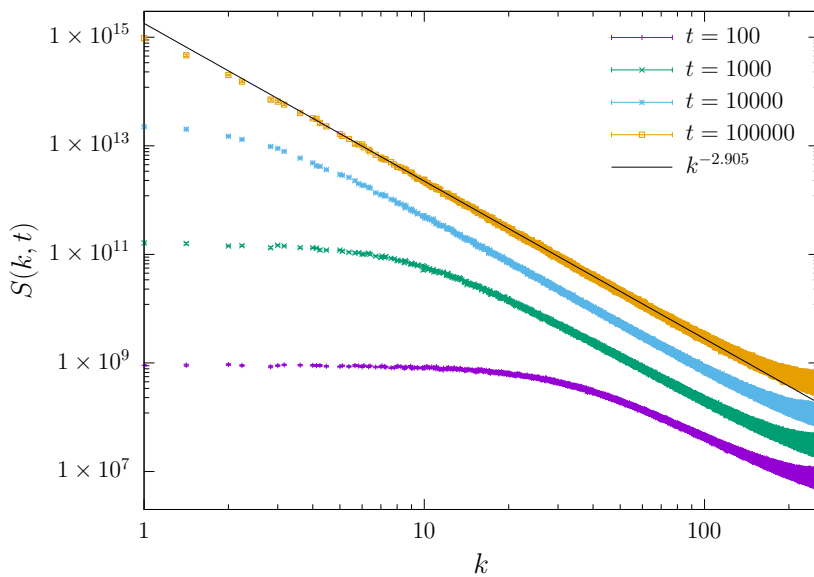
(c) Height-difference correlation function for $d = 3$ and $L = 128$.

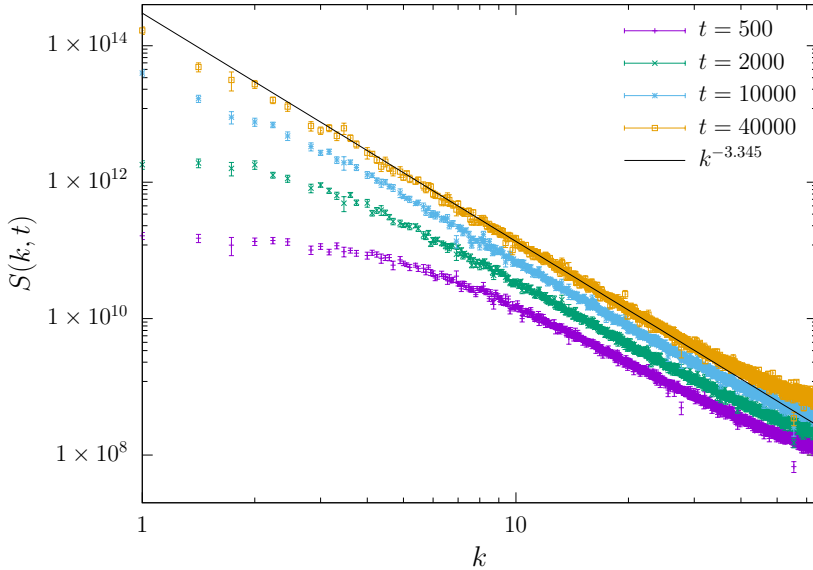
Figure 6.7: Data collapse of $C_2(r, t)$ for different dimensions and for different values of time, as indicated in each legend. The exponents α and z are those shown in Table 6.3. Solid lines are proportional to $x^{-2\alpha'}$ (left part) and $x^{-2\alpha}$ (right part).

6.3.4 Front structure factor

In the presence of anomalous scaling [88, 91] two-point correlations are frequently studied in Fourier space [163]. As mentioned in Sec. 3.1, the front structure factor $S(k, t)$ [see Eq.(3.17)] provides a complementary perspective on anomalous scaling, which is particularly useful in the context of crossover behavior [163] and/or large roughness exponent values [88–91]. Note that, in our system, α takes relatively large values for all d .

The curves in Fig. 6.8 show $S(k, t)$ as a function of the modulus of the wave vector k for different times for $d = 1, 2$, and 3. The time shift of the curves is noticeable for each dimension, and the high- k data agree well with the expected scaling law of Eq. (3.19), for which we have used the value of α_{loc} calculated previously (solid lines in the figure panels). Hence, the scaling behavior in Fourier space is consistent with that characterized in real space, as anticipated.

(a) Structure factor for $d = 1$ and $L = 8192$.(b) Structure factor for $d = 2$ and $L = 512$.



(c) Structure factor for $d = 3$ and $L = 128$.

Figure 6.8: Structure factor $S(k, t)$ for one, two, and three dimensions at several times. Solid lines correspond to $k^{-(2\alpha_{\text{loc}}+d)}$, where α_{loc} was computed from the scaling behavior found for $C_2(r, t)$, see Table 6.3.

Note that in the $d = 3$ case, in which our results differ more from those reported in Ref. [157], we have rescaled our $S(k, t)$ data (not shown), using both our values of α , α_{loc} , and z , as well as the ones provided in that reference; collapse is achieved in both cases within error bars.

6.3.5 Mean squared height gradient

The anomalous scaling behavior is associated with a non-trivial time evolution in the slope field $\nabla h(\mathbf{x}, t)$ [51, 164]. Indeed, the squared slope can be estimated by using the height-difference correlation function at a distance of one lattice spacing Δx , which yields

$$\langle (\nabla h)^2 \rangle \approx (\Delta x)^2 C_2(\Delta x, t). \quad (6.4)$$

Under the FV Ansatz, this value becomes time-independent already during the early stages of time evolution [11, 51]. However, in the presence of intrinsic anomalous scaling, this quantity only saturates at steady state

when $t = t_{\text{sat}} \sim L^z$. In this case, assuming that $\langle \overline{(\nabla h)^2} \rangle \sim t^{2\kappa}$, where κ is an exponent characterizing the anomalous increase in the average front slopes over time, then one expects the following scaling relation to hold [165]

$$\alpha_{\text{loc}} = \alpha - z\kappa. \quad (6.5)$$

This scaling law was confirmed by the simulation results presented in Ref. [157], and we consider it here in face of our numerical results. To address it, we need to compute the mean squared height gradient $\overline{(\nabla h)^2}$. In particular, the j -th component of the d -dimensional gradient of $h(\mathbf{x})$ may be approximated as

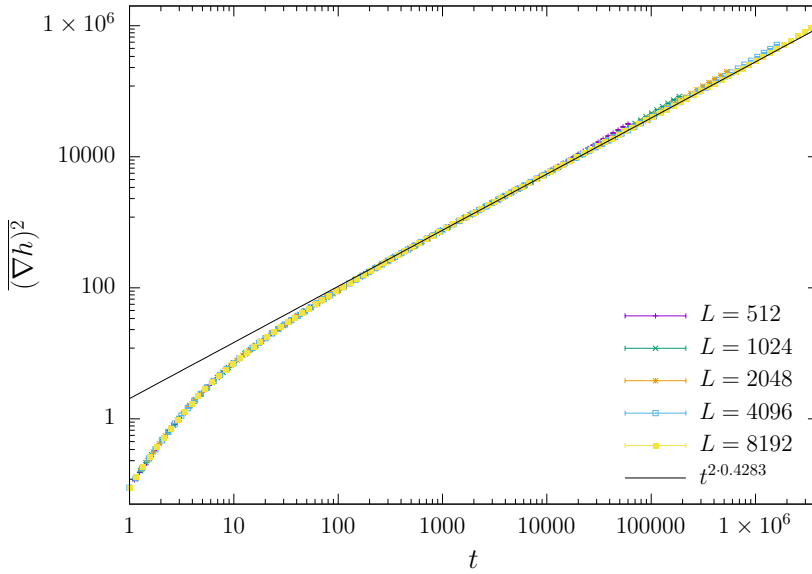
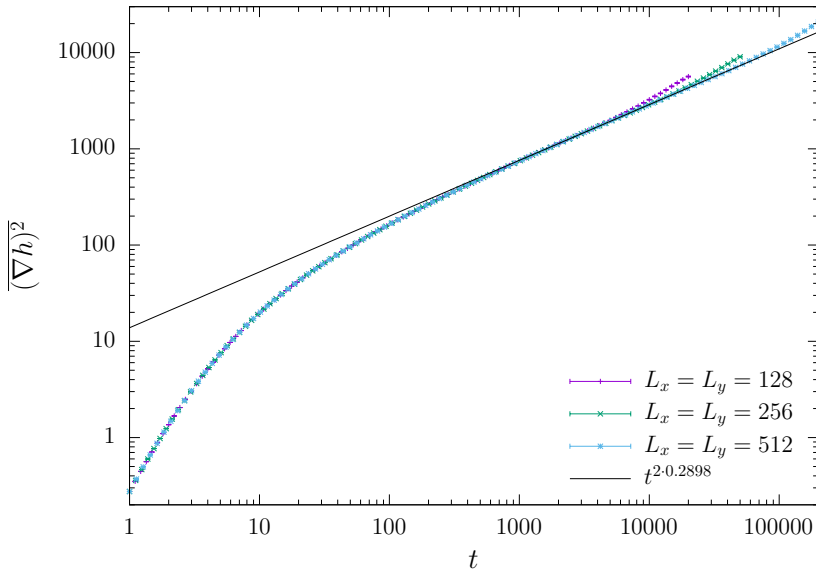
$$\partial h / \partial x_j \approx \frac{h(\mathbf{x} + (\Delta x)\mathbf{e}_j) - h(\mathbf{x})}{\Delta x}, \quad j = 1, \dots, d, \quad (6.6)$$

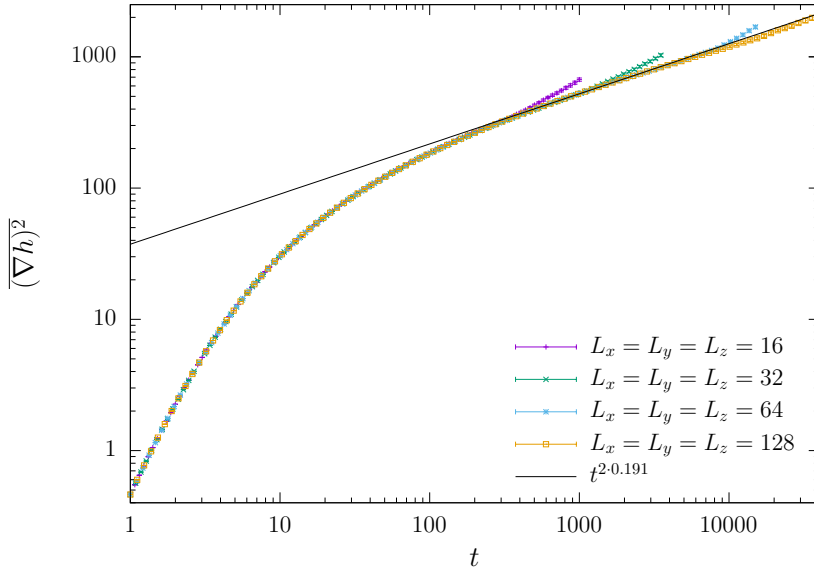
where \mathbf{e}_j is the j -th vector of the canonical basis in \mathbb{R}^d , and $\Delta x = 1$ in our lattice.

This analysis shows that $\langle \overline{(\nabla h)^2} \rangle$ grows with time as a power law for all values of d , as shown in Fig. 6.9. This relation is quantified by the exponent κ , whose values are listed in Table 6.4. By using these values of κ , along with our previously determined values of z and α , we have estimated a new value

Table 6.4: Exponents κ and α_{loc} obtained from Eq. (6.5) for different dimensions and system sizes.

d	L	κ	α_{loc}
1	512	0.4396(11)	0.643(10)
	1024	0.4329(9)	0.649(7)
	2048	0.4297(7)	0.652(9)
	4096	0.4258(6)	0.657(4)
	8192	0.4283(18)	0.650(4)
2	128	0.304(3)	0.466(12)
	256	0.2955(13)	0.458(7)
	512	0.2898(10)	0.458(7)
3	64	0.2018(18)	0.240(18)
	128	0.191(2)	0.21(4)

(a) Mean squared height gradient for $d = 1$.(b) Mean squared height gradient for $d = 2$.



(c) Mean squared height gradient for $d = 3$.

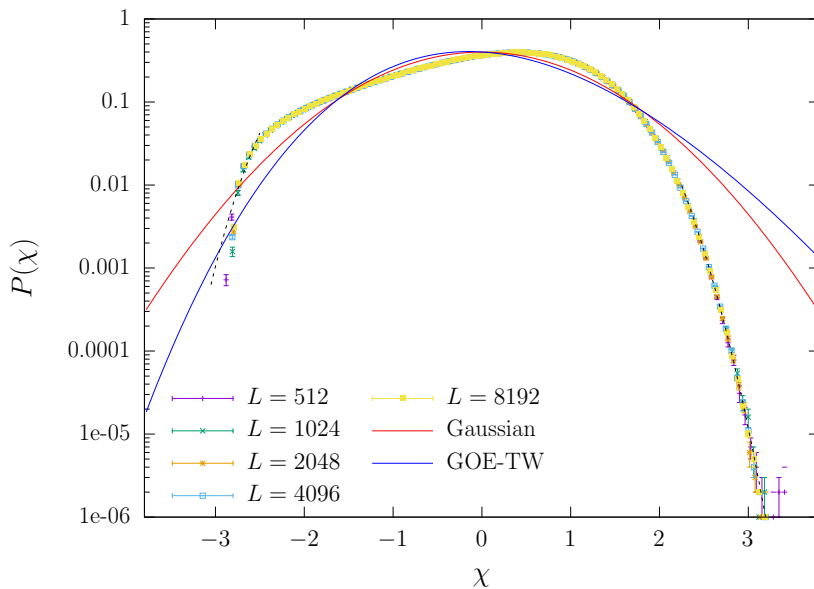
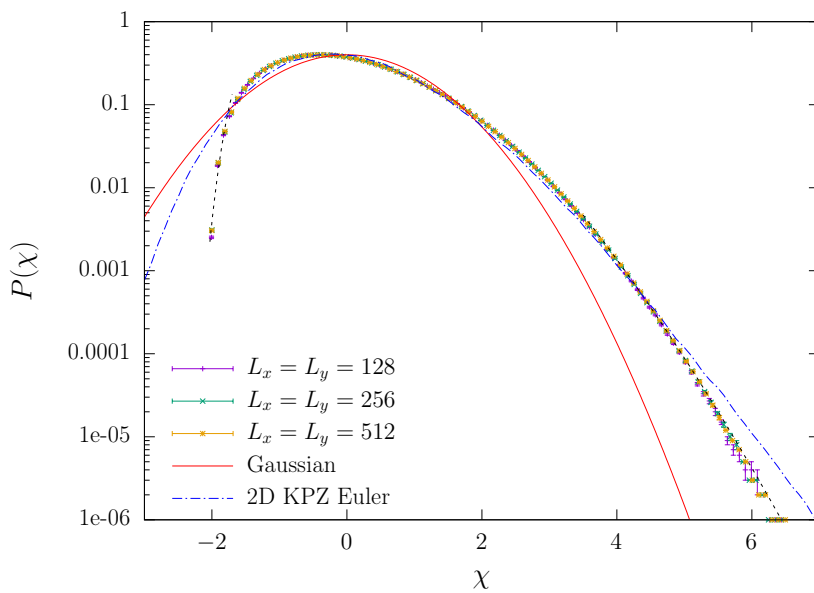
Figure 6.9: Mean squared height gradient for different dimensions and different sizes L . Solid lines show the best fit to the data for the largest L .

of α_{loc} , also listed in Table 6.4. These findings are consistent (especially for the largest system sizes) with the values of α_{loc} directly measured from $C_2(r, t)$ in Sec. 6.3.3, as summarized in Table 6.3.

6.3.6 PDF of front fluctuations

Besides examining the values of the scaling exponent, we also analyze next the statistical properties of the front fluctuations with the aim of identifying universal properties. Specifically, we have calculated the rescaled front fluctuations, $\chi(t)$, defined in Eq. (3.7), where the exponent β we have used is obtained from the front roughness in Sec. 6.3.1 (see Table 6.3). Only the time interval during which the roughness scales according to Eq. (3.4) with the chosen β has been considered.

In Fig. 6.10 we plot the PDF, $P(\chi)$, of the front fluctuation for $d = 1, 2$, and 3. It is interesting to note that $P(\chi)$ is not affected by the size of the system, L , at least within the statistical precision for all cases. Note that we have normalized our data to zero mean and unit variance. For comparison,

(a) PDF of front fluctuations for $d = 1$.(b) PDF of front fluctuations for $d = 2$.

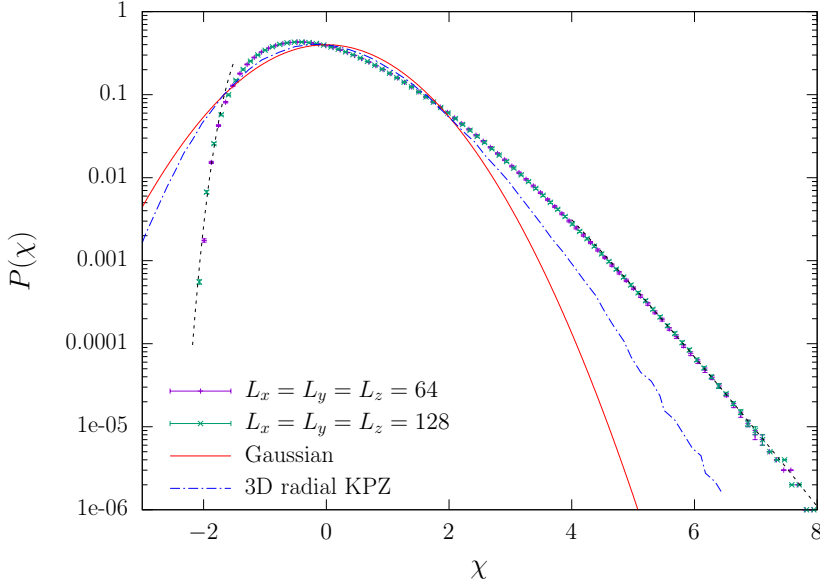
(c) PDF of front fluctuations for $d = 3$.

Figure 6.10: PDF of front height fluctuations for $d = 1, 2$, and 3 , and sizes indicated in each legend. For comparison, the solid lines correspond to the exact Gaussian distribution, the GOE-TW distribution, the 2D KPZ fluctuation distribution (Euler integration [36]) and the 3D KPZ fluctuation distribution (radial KPZ class [39]), as described in the legends. The dashed black lines correspond to the tail functions (left) $e^{-c|x|^{x_-}}$ and (right) $e^{-x^{x_+}}$, with η_- and η_+ exponent values as reported in Table 6.5.

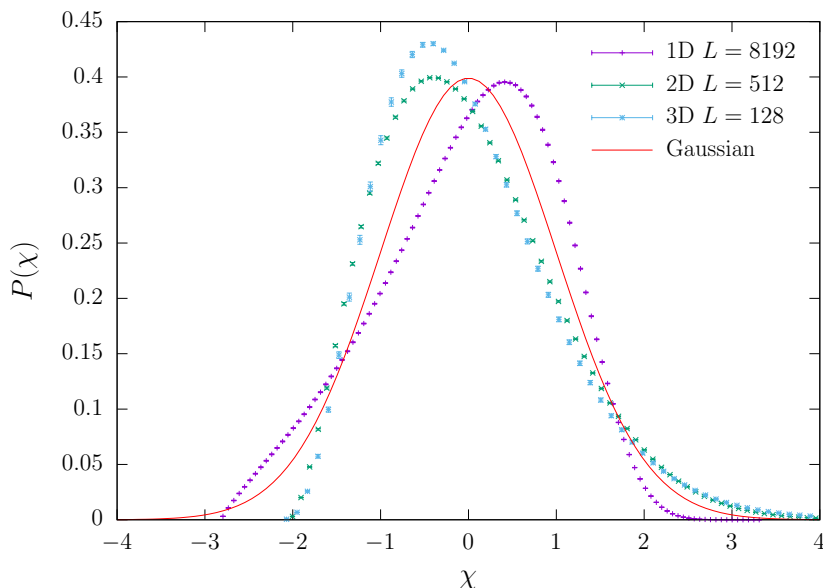
the figure shows the exact PDF for the Gaussian case, which is found for linear models of kinetically rough interfaces such as the EW equation with time-dependent noise [11, 34, 51], and the PDF for the KPZ universality class, which is dimension-dependent. In $d = 1$, the fluctuation PDF for rough interfaces in the 1D KPZ universality class using periodic boundary conditions is provided by the GOE-TW [12, 13] (see Sec. 1.3.3). For $d > 2$, distributions other than TW play analogous roles to the latter for the KPZ universality class [36, 39]. Particularly, for $d = 2$, we show in Fig. 6.10 the distribution obtained for an Euler integration of the KPZ equation and reported in Ref. [36]. Finally, for $d = 3$ we show the fluctuation PDF for the 3D radial KPZ class from the DPRM/SHE data collapse performed in Ref. [39].

Although the numerical PDFs that we obtain for the CP are definitely non-symmetric (with non-zero skewness, as in the KPZ case) for all the simulated dimensions, they are significantly different from the latter distributions. Moreover, they exhibit a strong dependence with the dimensionality of the system. In Fig. 6.11 we have represented the CP distributions for each of the simulated dimensions together; the plotted data are available in Zenodo open access repository [166]. The corresponding skewness s and excess kurtosis k values for the largest systems are collected in Table 6.5. Notably, the signs of s and k for $d = 1$ differ from their values for $d = 2$ and 3 , again at variance with the KPZ universality class. However, the magnitudes of s and k do increase with d , as is the case also for KPZ systems [36, 39, 167].

Let us now focus on the tails of the PDFs. These tails are asymmetric and non-Gaussian, and are expected to follow exponential functions for many random systems in their disorder-dominated phases [168] as

$$P(x) \approx \begin{cases} e^{-c|x|^{\eta_-}}, & x \rightarrow -\infty \\ e^{-dx^{\eta_+}}, & x \rightarrow +\infty, \end{cases} \quad (6.7)$$

where c and d are constants and η_- and η_+ are characteristic so-called tail exponents [22, 168]. We have fitted the distributions computed herein to functions (6.7) (dashed lines in Fig. 6.10) to estimate the η_- and η_+ exponents; the results are collected in Table 6.5. The tail exponents for the Tracy-Widom distribution have been studied in detail [22, 169]. For the $d = 1$ KPZ universality class, the exponent of the Airy tail (that is, right tail in the GOE-TW representation of Fig. 6.10) is $\eta_+ = 3/2$, whereas for the left tail one has $\eta_- = 3$ [169, 170]. In addition, for KPZ the left and right tail exponents are related to each other as $\eta_- = (d+1)\eta_+$, and also to the growth exponent through $\eta_+ = 1/(1-\beta)$ [22, 169]. Note, however, that although the fits are reasonable (specially for η_+) and such that $\eta_- > \eta_+ > 1$ for all d , as implied by the KPZ formulas, our data do not suggest any simple connection between the right and left tail exponents, or between them and β . Departure from the $\eta_+ = 1/(1-\beta)$ relation can also be found elsewhere, e.g., for synchronized oscillator lattices [35], for which the PDF is GOE-TW in spite of the fact that the kinetic roughening exponents (β , in particular) do not take their 1D KPZ values.



(a) PDFs of front fluctuations in linear scale.

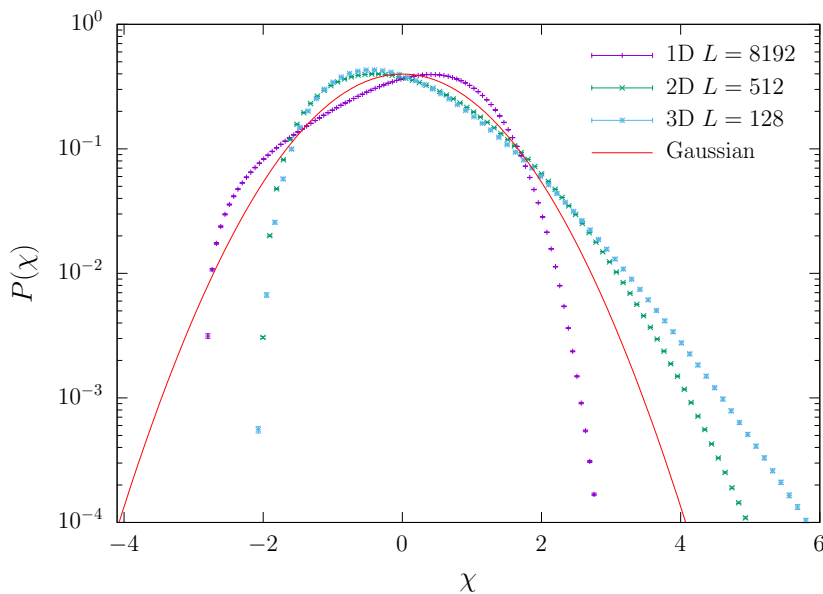
(b) Same data with logarithmic scale in y -axis. We represent probabilities $P > 10^{-4}$ for improved visibility and a better comparison between the different dimensions.

Figure 6.11: Histograms of front fluctuations in different dimensions. The solid line show the exact Gaussian distribution. The numerical data for this figure are openly available at Ref. [166].

Table 6.5: Skewness s , excess kurtosis k , and tail exponents η_- , η_+ for the front fluctuation distributions in different dimensions, as obtained in our simulations for the largest value of L in each case.

d	L	s	k	η_-	η_+
1	8192	-0.3677(15)	-0.421(3)	4.05(3)	3.12(2)
2	512	0.6246(18)	0.233(3)	6.261(15)	1.559(6)
3	128	0.848(5)	0.987(17)	5.12(2)	1.251(13)

6.3.7 Front covariance

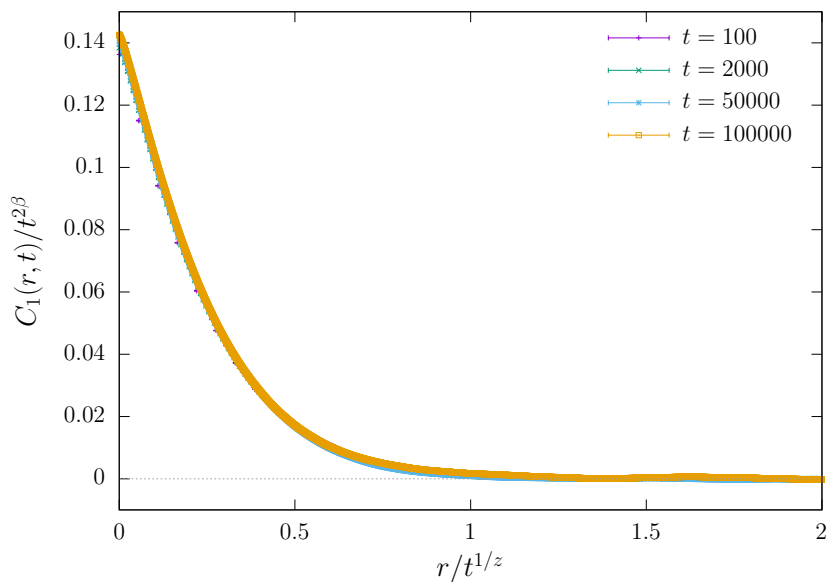
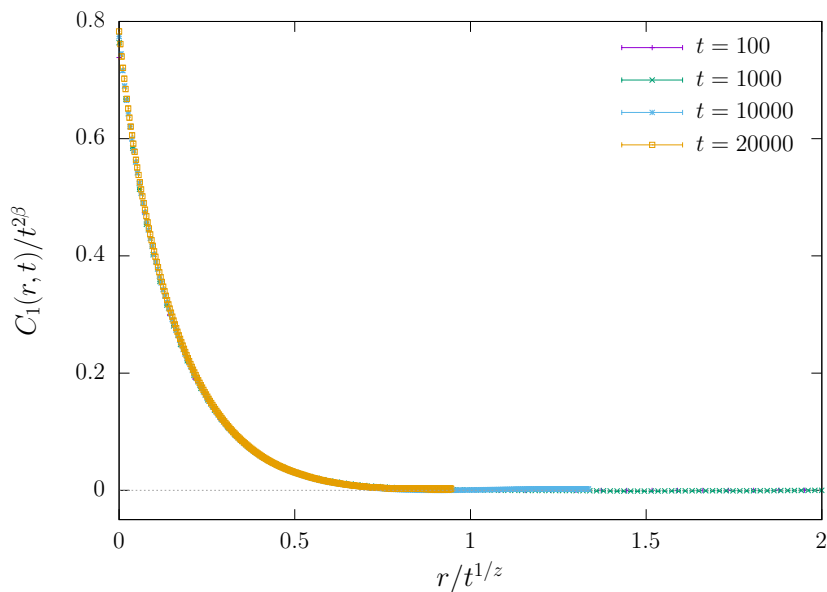
As noted in Sec. 3.1, the front covariance correlation function $C_1(\mathbf{r}, t)$, defined as Eq. (3.8), is expected to behave for kinetic roughening systems as

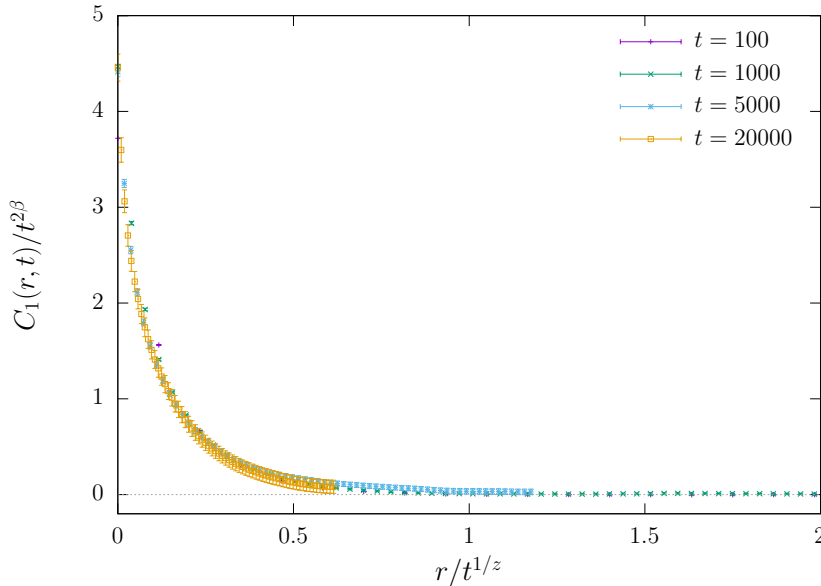
$$C_1(\mathbf{r}, t) = t^{2\beta} F(r/t^{1/z}), \quad (6.8)$$

where $F(u)$ is a universal function which becomes an additional (albeit nonexclusive) trait of the universality class. In the 1D KPZ scenario, this function is the Airy $_i$ covariance function with $i = 1$ or 2, depending on the boundary conditions; see the discussion in Sec. 1.3.3.

In this section, we examine the front covariance, represented by Eq. (6.8), and its scaling for dimensions $d = 1, 2$, and 3. We use our estimated values for β and z to express this scaling assumption in each case. The results for the largest size for $d = 1$ ($L = 8192$), $d = 2$ ($L = 512$), and $d = 3$ ($L = 128$) are presented in Fig. 6.12. As anticipated, we observe that the rescaled curves for different times do overlap. This behavior is also observed when curves for different system sizes are compared. Furthermore, we note that the exponents governing this collapse (β and z) are global ones, even when the scaling is intrinsically anomalous, that is, non-FV. While there exists a maximum time for each system size above which curves for different times do not overlap, this is a finite-size effect, and this maximum time increases systematically with L .

The quantitative characteristics of the CP scaling function vary depending on the value of d , but its fundamental properties remain the same. It is especially important to examine the $d = 1$ scenario closely. As previously stated, the behavior of the height covariance $C_1(r, t)$ in systems belonging

(a) Scaled covariance for $d = 1$ and $L = 8192$.(b) Scaled covariance for $d = 2$ and $L = 512$.



(c) Scaled covariance $d = 3$ and $L = 128$.

Figure 6.12: Scaled front covariance $C_1(r, t)$ for different dimensions at times as given in the legends. The exponents β and z are those shown in Table 6.3. In each case, times larger than those shown do not scale properly. The numerical data for this figure are openly available at Ref. [171].

to the 1D KPZ class can be described by Eq. (3.10). In the case of periodic boundary conditions, $A_i(u)$ denotes the covariance of the Airy_1 process [13, 22, 33], and a_1 and a_2 are fitting constants. The function $C_1(r, t)$ for $d = 1$ appears to align with Eq. (3.10), which is demonstrated in Fig. 6.13. Although there are slight variations in values when $r/t^{1/z}$ is small (as shown in the inset of Fig. 6.13), the difference between the theoretical and numerical curves in this range is no more than 3%.

We observe that our numerical data for $C_1(\mathbf{r}, t)$ in two and three dimensions do not follow the same scaling behavior as $\text{Airy}_1(u)$ (not shown). This is not surprising because, unlike the one-dimensional case, the Airy_i behavior appears to be specific to the 1D KPZ class. Our data for 2D (not shown) do not seem to agree with the 2D KPZ universality class either, whose covariance is numerically well-characterized [38, 57]. The CP front covariances for each dimension are also available as open data from Ref. [171].

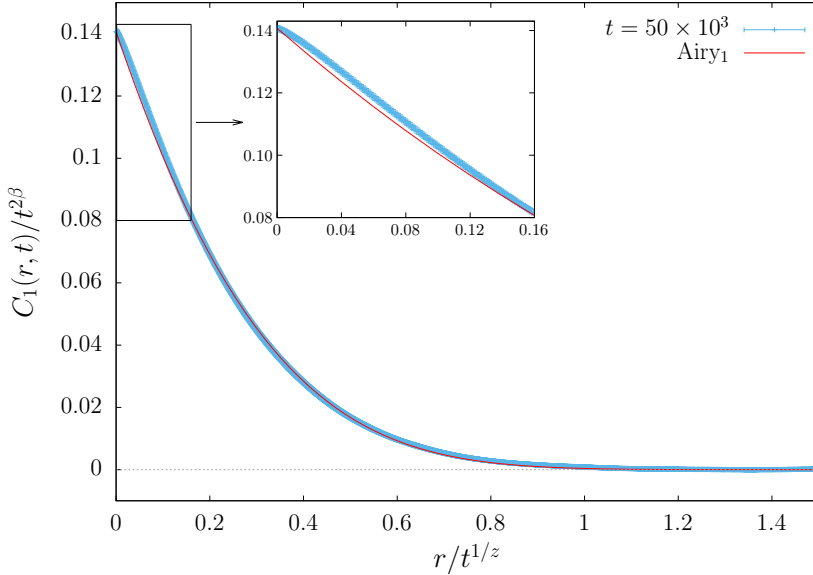


Figure 6.13: Scaled CP front covariance $C_1(r, t)$ for $d = 1$ and $L = 8192$ at $t = 5 \times 10^4$. The solid line shows a function proportional to the covariance of the Airy_1 process. Inset: Zoom of the boxed small-argument region in the main panel.

6.4 Conclusions

We found out that, when working at the absorbing state phase transition, the interface problem linked with the CP exhibits all the features of a kinetic roughening universality class. This includes well-defined scaling exponents, a fluctuation probability density function, and covariance, all of which depend on the substrate dimension. Moreover, an intrinsically anomalous dynamical scaling is observed in a consistent manner.

We have studied the interface representation of the CP particle model in one, two, and three dimensions by numerical simulations. To characterize the universality behavior of the interface we calculated the set of critical exponents (θ , α , α_{loc} , β , and z). We have explicitly shown the behavior of the associated scaling observables for the three simulated dimensions. Overall, we have found a good agreement with the exponents previously reported in the literature [157]. Specifically, we have estimated the dynamic critical exponent z by computing directly the correlation length via the analysis of

the height-difference correlation function C_2 in real space. Focusing on this exponent, our numerical values do increase with increasing d towards the diffusive $z = 2$ value expected [157] at and above d_c , with some overshoot in the 3D case. The latter fact could be a size effect. Indeed, Table 6.3 exhibits a dependence of all exponents on the system size, which is particularly noticeable for $d = 3$. In this sense, we cannot guarantee that our values for $L = 128$ may be considered as asymptotic, especially for exponents z and α . Note that exponents θ and β for $d = 3$ are in good agreement with theoretical predictions, though.

As previously stated, relying solely on critical exponents is insufficient to fully characterize a universality class. Instead, it is crucial to analyze the local statistical properties of the front, namely the probability distribution function (PDF) of the rescaled height fluctuations (χ) and the scaling of the C_1 correlation function, which depicts the front covariance. Therefore, we have conducted a thorough analysis of both for $d < d_c = 4$, obtained herein for the first time.

We have found that the PDF of the local fluctuations of the front does not conform to any previously reported behavior (e.g., GOE-TW or Gaussian). Instead, it exhibits a strong dependence to the dimensionality of the system. In particular, there is an unexpected change of shape between the distribution for $d = 1$ and those for $d = 2$ and 3 , with a change of sign of both skewness and kurtosis. The overall behavior of the front covariance remains consistent as the system dimensions change, but its quantitative behavior varies greatly depending on the dimensionality. We observe that the 1D front covariance closely resembles that of the Airy_1 process, with an accuracy of approximately 3%. However, we could not find any existing analytical functions that match the front covariance curves in the other simulated dimensions.

It is worth noting that the universal fluctuation PDF and covariance have pronounced non-Gaussian characteristics for all the dimensions under consideration. In the context of kinetic roughening systems, nowadays such a behavior has been reported either for the KPZ universality class [12, 13], or for other classes somehow related with it (some of which feature anomalous scaling), like those of the conserved KPZ equation [132], the tensionless KPZ equation [158], precursor spreading [159], or systems related

to the KPZ equation with columnar disorder [35]. From this perspective, the CP appears innovative due to its provision of alternative options for non-Gaussian interfacial behavior. Moreover, the 1D CP represents another noteworthy system exhibiting Airy behavior in spite of not having KPZ exponents, in addition to previously reported cases [34, 159].

For the CP we obtain a consistent intrinsic anomalous scaling Ansatz for $d < d_c$. This anomalous scaling has been thoroughly studied through the correlation function C_2 , but also computing the structure factor. Additionally, we calculate the mean square height gradient, which allows us to compute the local roughness exponent by a different way. For increasing d , both α and α_{loc} decrease, as expected [11]. However, the relative difference $(\alpha - \alpha_{\text{loc}})/\alpha$ does not become particularly reduced with increasing d , so that the intrinsic anomaly in the scaling persists somehow all the way up to the upper critical dimension $d_c = 4$.

It would be of interest to examine the emergence of intrinsic anomalous scaling in a hypothetical continuum description of the interface problem related to CP. Recall that intrinsic anomalous scaling has been conjectured not to be asymptotic for systems with local interactions, in which neither morphological instabilities nor quenched disorder occur [160]. Various discrete models are known to exhibit intrinsic anomalous scaling while their continuum limits do not (see for instance Ref. [159]). However, there are methods to overcome this prediction, as for the tensionless KPZ equation [158].

Note that the continuum description of the CP as a particle model is provided by the phenomenological Langevin equation [Eq. (2.15)], which, rescaling the noise term $\eta(t, \mathbf{x})$ in order to be a zero-average Gaussian noise of unit variance, corresponds to the following reaction-diffusion equation for a local density field $\rho(\mathbf{x}, t)$ [61],

$$\partial_t \rho = D \nabla^2 \rho + \rho - \rho^2 + \sqrt{C} \rho \eta(\mathbf{x}, t), \quad (6.9)$$

where $D, C > 0$ are constants. Note the absorbing nature of the $\rho = 0$ state, which suppresses both dynamics and fluctuations. We find it interesting that the kinetic roughening universality class of the (interface representation of the) CP turns out to be very different compared with that of systems described by the (deceivably) similar stochastic Fisher-Kolmogorov-Petrovsky-Piscounov (sFKPP) equation [Eq. (4.2)], where $\eta(\mathbf{r}, t)$ is the same noise as in Eq. (6.9). As seen in Chapter 4, Eq. (4.2) provides a coarse-

grained description for the $A + A \leftrightarrow A$ reaction-diffusion particle model [117–119], but remarkably, in this case the kinetic roughening behavior of the corresponding moving front problem is in the standard KPZ universality class [115, 172]. Quite possibly the DP behavior at the absorbing phase transition in the CP [61, 62] is at the core of this stark difference between Eqs. (6.9) and (4.2), and likewise for their corresponding particle models. From this point of view, the existence of absorbing states in particle models may play a similar role in the (anomalous) kinetic roughening scaling Ansatz of interface systems they map into to that played by morphological instabilities and/or quenched disorder [160].

Nevertheless, it is interesting to note that, at least in the one-dimensional scenario, the universality classes of CP and standard KPZ appear to share exactly the same Airy_1 covariance. Another intriguing similarity of the interface representation of the CP remains in the Mullins-Herring equation with quenched disorder [173]. Indeed, this model has been seen not only to feature anomalous scaling [174], but its scaling exponents (including those characterizing the pinning transition seen to occur) are numerically quite close to those of CP/DP, at least for $d = 1$ and 2 [175]. It is remarkable that DP is also known to control the interface scaling at depinning for other well known interfacial systems, such as the QKPZ equation discussed in Sec. 2.6. Regarding the behavior of anomalous kinetic roughening with dimension, it is worth noting that new findings have shown its occurrence in the synchronization of oscillator lattices [35], which makes it more interesting for potential applications in synchronization phenomena [176, 177].

Finally, we consider that, with the numerical characterization of the statistical fluctuation properties of the front in one, two, and three dimensions, we have provided important pieces of information which were lacking, needed to fully characterize the kinetic roughening behavior of one of the most important non-equilibrium universality classes, that of the directed percolation.

Chapter 7

Thesis summary and future work

The main purpose of the thesis is the study of various growth fronts through the point of view of kinetic roughening, specifically within non-equilibrium systems where one can define a surface and analyze its dynamics by applying scaling hypotheses. The significance of this research stems from the emergence of universality classes, which group together a range of properties, such as scaling exponents and statistical functions, that are shared by vastly different systems, regardless of their intrinsic characteristics. Throughout this study, we consistently worked with systems characterized by randomness: particles assume random positions or orientations. Surprisingly, these systems have revealed universal characteristics that transcend their microscopic differences. These features, potentially counter-intuitive to those non-experts in statistical physics, are what render this work truly exciting.

Three research papers underpin this thesis. In the first of these, encapsulated in Chapter 4: Reaction-diffusion fronts, we study a two-dimensional system wherein particles interact through diffusion, creation, and annihilation processes. As a consequence, the system grows in a certain direction and we measure the front (which in this case is one-dimensional) as the interface that separates the region filled with particles from the empty one. In this chapter, we have systematically quantified the critical exponents, namely β , α , and z , and consistently computed universal functions characterizing front, including the PDF of the fluctuation and the height covariance. Our

comprehensive analysis consistently provides strong evidence for a robust alignment with the 1D KPZ universal class, corroborating the findings of prior research, particularly the seminal work of Moro in Ref. [98] revisited herein.

Chronologically in the development of the PhD, this work marks the first publication. It served as the foundation for establishing a standardized methodology for front measurement, one that could be applied to any height function to extract its statistical measures, and especially, critical exponents and correlation functions. Additionally, we introduced an innovative approach that facilitates the direct measurement of the exponent z . Specifically, we proposed and used a novel method to compute the correlation length from the height-difference correlation function, in real space, in its saturation state. This analysis has been replicated in subsequent works (and chapters of this thesis), enabling a comparative analysis of this exponent with earlier findings, where it was estimated by other alternative methods.

Furthermore, we opted to calculate the statistical errors for all the observables presented in this initial work (and in those that follow) employing the jackknife method to handle the highly correlated data. This method is recommended for simulation work involving random sampling. Unlike this methodology, the standard fit procedures (based in a diagonal χ^2 analysis, i.e., neglecting completely the correlation among the data) underestimate the statistical errors, for example, in the critical exponents, by more than a factor 10.

The second research system is featured in Chapter 5: Coffee-rings fronts. The application of surface kinetic roughening to something as commonplace as a coffee droplet was conducted by Yunker *et al.* in experimental research published in the journals Nature [137] and Phys. Rev. Lett. [140], where supplementary information includes excellent videos. In our study, we employed the patchy colloids model to simulate the behavior of the coffee droplet, following the previous studies developed by Dias, Araújo, and Telo da Gama in Refs. [145–147]. The results of our simulations were overwhelming, since we were unable to identify the previously mentioned universality classes, specifically KPZ and QKPZ, in the asymptotic regime within this system. We finally managed to discern that this was due to the emergence

of macroscopic shapes in the evolution of colloid aggregates, which was reflected in the critical exponent values.

Nevertheless, we were able to characterize the front dynamics before the emergence of these macroscopic shapes. To achieve this, we examined the system with respect to the sticking parameter r_{AB} which provides the probability of one type of bond formation in the aggregates (being favored over another). Initially, we found that the system undergoes a phase transition for $r_{AB} = 0$, where only long branched formations occur due to colloids restricting their orientation during bonding. Our analysis of critical exponent values led us to conclude that there exists a range of values ($r_{AB} > 0.01$) in which the scaling behavior aligns with that of the 1D KPZ universality class. However, we observed a crossover phenomenon for small values of r_{AB} ($r_{AB} \leq 0.01$), since the behavior for $r_{AB} = 0$ begins to dominate. In addition to the critical exponents, we examined the correlation function, which exhibited anomalous scaling for $r_{AB} < 0.01$. Calculating the structure factor allowed us to determine that the system displayed intrinsically anomalous scaling, differing from the standard scaling (i.e., as that of KPZ). This provides novel insights into this system and in kinetic roughening behavior.

The third study encompassed within this thesis is detailed in Chapter 6: Contact process fronts. In this case, we study a “fictional” front, one that does not describe the particle advance but rather measures the particle occupation at each point within the system, which can be interpreted as its activity. The intriguing aspect of this study lies in the fact that the microscopic CP model, belonging to the DP universality class, undergoes a transition into an absorbing phase (where the system is emptied of particles). We investigated the CP model precisely at the critical point because, at this point, the scaling properties of the interface can be related to those of the original particle model, thus providing insights into the DP/CP universality class. Numerous results were presented as we conducted the study in one, two, and three-dimensional systems, exploring various sizes in each case, as usual. We thus extended the previous work of Ref. [157], obtaining critical exponents consistent with those of DP. Moreover, we enriched the analysis by calculating other universal functions such as the PDF of fluctuations and the covariance of the front. This contribution is highly significant and innovative, as it introduces universal functions not previously

measured for the DP/CP class. Additionally, we found that this system exhibits intrinsically anomalous scaling, in accord with Ref. [157].

Regarding open issues, there are several avenues for further exploration within the presented systems. For instance, it would be intriguing to characterize reaction-diffusion fronts in higher dimensions, potentially even reaching their upper critical dimension if it exists (which is not guaranteed, as for KPZ). Furthermore, concerning the CP system in three dimensions, achieving a more robust statistical dataset would have been desirable, involving additional runs and larger system sizes. However, this presents a challenge due to the significant simulation time required.

As additional future work, our most immediate objective is to publish the initial findings obtained in collaboration with the Dias, Araújo, and Telo de Gama research group. Upon revisiting the work by Dias *et al.* [145–147], it was determined that a three-month research visit to their group would be highly beneficial. During this visit, we engaged in discussions concerning the novel findings in the context of coffee-ring phenomena. Additionally, this collaboration led to the initiation of a new research direction, focusing on the topic of active matter and non-equilibrium phase transitions. Specifically, simulations to investigate the transition between phase-separated states when local active currents were introduced, disrupting the system equilibrium, are being conducted.

In conclusion, it is our hope that this thesis serves as a resource to help future researchers who choose to delve into and work on surface kinetic roughening. It establishes a theoretical framework, offers a simple but clear methodology, and presents systems that exemplify some of the interesting and complex behaviors one may encounter in this field.

Appendices

A Relation between α and z in the KPZ equation

We start from the KPZ equation [Eq. (1.14)]. The effect of a small fluctuation $\delta\eta$ results in the formation of a bump or hole with length ξ and height δh . Considering these as perturbations, we can rewrite the equation as

$$\frac{\delta h}{t} \approx \nu \frac{\delta h}{\xi^2} + \frac{\lambda}{2} \frac{(\delta h)^2}{\xi^2}. \quad (\text{A.1})$$

Assuming the scaling of the width, Eq. (1.1): $w \sim \langle \delta h \rangle \sim L^\alpha$, and the scaling of the correlation length, Eq. (1.4): $L \sim \xi \sim t^{1/z}$, we obtain that

$$t^{\frac{\alpha}{z}-1} \sim \nu t^{\frac{\alpha}{z}-\frac{2}{z}} + \frac{\lambda}{2} t^{\frac{2\alpha}{z}-\frac{2}{z}}. \quad (\text{A.2})$$

Since $\alpha/z > 0$, the term proportional to λ dominates: $\frac{2\alpha}{z} - \frac{2}{z} > \frac{\alpha}{z} - \frac{2}{z}$, then, $t^{\frac{2\alpha}{z}-\frac{2}{z}} \gg t^{\frac{\alpha}{z}-\frac{2}{z}}$. Note that, when λ is absent, the universality class is EW. We can equal the exponent on the left hand side of Eq. (A.2) with the one in the term carrying lambda resulting in $\alpha + z = 2$, as in Eq. (1.15).

B The coefficient λ of the nonlinear term

In many situations, it is difficult to compute reliable scaling exponents, due to complicated crossover behavior and/or to finite-size effects. In these cases, an alternative method for identifying universality classes is to obtain direct evidence of the presence of different terms in the growth equation, such as the nonlinear term $\lambda(\nabla h)^2$ which distinguishes the KPZ universality class from that of EW.

The most straightforward way to determine the parameter λ is based on the fact that the average interface velocity v depends on the interface tilt m [11, 178]. Indeed, the mean velocity of the interface is

$$v \equiv \int d^d \mathbf{x} \left\langle \frac{\partial h}{\partial t} \right\rangle. \quad (\text{B.3})$$

If one calculates v from Eq. (B.3) using the EW equation [Eq. (1.10)], the result is zero. The reasons are that the contribution from the Laplacian term is zero due to the periodic boundary conditions and that the noise has zero average. However, in the presence of a nonlinear term, as in the KPZ equation [Eq. (1.14)], the mean velocity is

$$v = \frac{\lambda}{2} \int d^d \mathbf{x} \langle (\nabla h)^2 \rangle \neq 0. \quad (\text{B.4})$$

In general, the graph of the interface position vs. time has a zero average slope. However, in computational models, one may generate an overall slope $m^2 = \langle (\nabla h)^2 \rangle$ of the interface. An useful way to introduce this slope, or tilt, in discrete models is by using helicoidal boundary conditions such as $x(L) = x(0) - Lm$. Hence, the average velocity changes with the tilt m as

$$v(m) = v(0) + \frac{\lambda}{2} m^2. \quad (\text{B.5})$$

Plotting the velocity against the slope, one expects to find a parabola from which one may compute the value of the nonlinear coefficient λ .

C From the microscopic $A + A \leftrightarrow A$ model to the FKPP equation

The model chosen to simulate the $A + A \leftrightarrow A$ process in Chapter 4 is ruled by creation, destruction, and diffusion processes. An (adjacent) site with which the chosen particle interacts is selected with a probability D . Once the site is chosen we distinguish between the cases in which it is occupied or empty; we call this probability of occupation P_{oc} . Hence, the reaction process occurs with probability $D(1 - P_{\text{oc}})\mu$ and the destruction process occurs with probability DP_{oc} . Then, if N denotes the number of particles of the system, the following balance equation is satisfied,

$$N(t+1) = N(t) + N(1 - P_{\text{oc}})\nu - N(P_{\text{oc}})D, \quad (\text{C.6})$$

where $\nu = \mu D$ is the probability of creation. Switching to the density $\rho = N/V$, where V is the volume of the system and taking into account that $P_{oc} = \rho$, the equation reads

$$\rho(t+1) - \rho(t) = \rho(1 - \rho)\nu - D\rho^2. \quad (\text{C.7})$$

Assuming $\rho(t+1) - \rho(t) \approx \frac{d\rho}{dt}$ and adding the spatial variation $D\nabla^2\rho$, we obtain the FKPP equation,

$$\frac{d\rho}{dt} = D\nabla^2\rho + \nu\rho - (\nu + D)\rho^2. \quad (\text{C.8})$$

Comparing with Eq. (4.1), we find that $\nu = R$ and $\nu + D = R/K$, which yields

$$K = \frac{\nu}{\nu + D} = \frac{\mu}{\mu + 1}. \quad (\text{C.9})$$

At steady state (i.e., $\frac{d\rho}{dt} = 0$), Eq. (C.8) yields the equilibrium density

$$\rho_{eq} = \frac{\nu}{\nu + D} = \frac{\mu}{\mu + 1}, \quad (\text{C.10})$$

where we have used that $\nu = \mu D$. In the model, ρ_{eq} is the density of our system at $t = 0$.

Bibliography

- [1] A. S. Mori, *Ecosystem management based on natural disturbances: hierarchical context and non-equilibrium paradigm*, J. Appl. Ecol. **48**, 280 (2011).
- [2] E. V. Albano, *Critical behaviour of a forest fire model with immune trees*, J. Phys. A: Math. Gen. **27**, L881 (1994).
- [3] W. B. Arthur, *Complexity and the Economy*, Science **284**, 107 (1999).
- [4] R. Hilfer, T. Rage, and B. Virgin, *Local percolation probabilities for a natural sandstone*, Physica A **241**, 105 (1997).
- [5] M. Ohring, *Materials Science of Thin Films* (Academic Press, San Diego, 2002).
- [6] S. Ramaswamy, *The mechanics and statistics of active matter*, Annu. Rev. Condens. Matter Phys. **1**, 323 (2010).
- [7] M. C. Marchetti, J. F. Joanny, S. Ramaswamy, T. B. Liverpool, J. Prost, M. Rao, and R. A. Simha, *Hydrodynamics of soft active matter*, Rev. Mod. Phys. **85**, 1143 (2013).
- [8] A. Polkovnikov, K. Sengupta, A. Silva, and M. Vengalattore, *Colloquium: Nonequilibrium dynamics of closed interacting quantum systems*, Rev. Mod. Phys. **83**, 863 (2011).
- [9] H. Weimer, A. Kshetrimayum, and R. Orús, *Simulation methods for open quantum many-body systems*, Rev. Mod. Phys. **93**, 015008 (2021).

-
- [10] U. C. Täuber, *Critical Dynamics: A Field Theory Approach to Equilibrium and Non-Equilibrium Scaling Behavior* (Cambridge University Press, Cambridge, 2014).
- [11] A.-L. Barabási and H. E. Stanley, *Fractal Concepts in Surface Growth* (Cambridge University Press, Cambridge, 1995).
- [12] T. Kriecherbauer and J. Krug, *A pedestrian's view on interacting particle systems, KPZ universality and random matrices*, J. Phys. A: Math. Theor. **43**, 403001 (2010).
- [13] K. A. Takeuchi, *An appetizer to modern developments on the Kardar-Parisi-Zhang universality class*, Physica A **504**, 77 (2018).
- [14] J. Yeomans, *Statistical Mechanics of Phase Transitions* (Clarendon Press, 1992).
- [15] K. G. Wilson and J. Kogut, *The renormalization group and the ϵ expansion*, Phys. Rep. **12**, 75 (1974).
- [16] J. Sethna, *Statistical Mechanics: Entropy, Order Parameters and Complexity*, Oxford Master Series in Physics (Oxford University Press, 2006).
- [17] S. Dattagupta, *Nonequilibrium phase transitions*, Bull. Mater. Sci. **1**, 227 (1979).
- [18] K. Christensen and N. R. Moloney, *Complexity and Criticality* (Imperial College Press, 2005).
- [19] R. Baiod, D. Kessler, P. Ramanlal, L. Sander, and R. Savit, *Dynamical scaling of the surface of finite-density ballistic aggregation*, Phys. Rev. A **38**, 3672 (1988).
- [20] P. Meakin, P. Ramanlal, L. M. Sander, and R. C. Ball, *Ballistic deposition on surfaces*, Phys. Rev. A **34**, 5091 (1986).
- [21] M. Kardar, G. Parisi, and Y.-C. Zhang, *Dynamic scaling of growing interfaces*, Phys. Rev. Lett. **56**, 889 (1986).
- [22] T. Halpin-Healy and K. A. Takeuchi, *A KPZ cocktail-shaken, not stirred... Toasting 30 years of kinetically roughened surfaces*, J. Stat. Phys. **160**, 794 (2015).

-
- [23] T. J. Oliveira, *Kardar-Parisi-Zhang universality class in $(d + 1)$ -dimensions*, Phys. Rev. E **106**, L062103 (2022).
- [24] G. W. Anderson, A. Guionnet, and O. Zeitouni, *An Introduction to Random Matrices* (Cambridge University Press, 2009).
- [25] C. A. Tracy and H. Widom, *Level-spacing distributions and the Airy kernel*, Commun. Math. Phys. **159**, 151 (1994).
- [26] C. A. Tracy and H. Widom, *On orthogonal and symplectic matrix ensembles*, Commun. Math. Phys. **177**, 727 (1996).
- [27] K. A. Takeuchi and M. Sano, *Evidence for geometry-dependent universal fluctuations of the Kardar-Parisi-Zhang interfaces in liquid-crystal turbulence*, J. Stat. Phys. **147**, 853 (2012).
- [28] A. Borodin, P. L. Ferrari, and T. Sasamoto, *Large time asymptotics of growth models on space-like paths II: PNG and parallel TASEP*, Commun. Math. Phys. **283**, 417 (2008).
- [29] T. Sasamoto, *Spatial correlations of the 1D KPZ surface on a flat substrate*, J. Phys. A: Math. Gen. **38**, L549 (2005).
- [30] M. Prähofer and H. Spohn, *Scale invariance of the PNG droplet and the airy process*, J. Stat. Phys. **108**, 1071 (2002).
- [31] S. Prolhac and H. Spohn, *Height distribution of the Kardar-Parisi-Zhang equation with sharp-wedge initial condition: Numerical evaluations*, Phys. Rev. E **84**, 011119 (2011).
- [32] F. Bornemann, P. L. Ferrari, and M. Prähofer, *The Airy₁ process is not the limit of the largest eigenvalue in GOE matrix diffusion*, J. Stat. Phys. **133**, 405 (2008).
- [33] F. Bornemann, *On the numerical evaluation of Fredholm determinants*, Math. Comp. **79**, 871 (2010).
- [34] I. S. Carrasco and T. J. Oliveira, *Geometry dependence in linear interface growth*, Phys. Rev. E **100**, 042107 (2019).
- [35] R. Gutiérrez and R. Cuerno, *Nonequilibrium criticality driven by Kardar-Parisi-Zhang fluctuations in the synchronization of oscillator lattices*, Phys. Rev. Res. **5**, 023047 (2023).

- [36] T. Halpin-Healy, *(2+1)-dimensional directed polymer in a random medium: scaling phenomena and universal distributions*, Phys. Rev. Lett. **109**, 170602 (2012).
- [37] T. J. Oliveira, S. G. Alves, and S. C. Ferreira, *Kardar-Parisi-Zhang universality class in (2+1) dimensions: Universal geometry-dependent distributions and finite-time corrections*, Phys. Rev. E **87**, 040102 (2013).
- [38] T. Halpin-Healy and G. Palasantzas, *Universal correlators and distributions as experimental signatures of (2 + 1)-dimensional Kardar-Parisi-Zhang growth*, EPL **105**, 50001 (2014).
- [39] T. Halpin-Healy, *Extremal paths, the stochastic heat equation, and the three-dimensional Kardar-Parisi-Zhang universality class*, Phys. Rev. E **88**, 042118 (2013).
- [40] J. Burgers, *A Mathematical Model Illustrating the Theory of Turbulence* (Elsevier, 1948) pp. 171–199.
- [41] H. A. Makse and L. A. Amaral, *Scaling behavior of driven interfaces above the depinning transition.*, EPL **31**, 379 (1995).
- [42] J. M. Kim and H. Choi, *Depinning transition of the quenched Edwards-Wilkinson equation*, J. Korean Phy. Soc. **48**, 241 (2006).
- [43] L. A. N. Amaral, A.-L. Barabási, H. A. Makse, and H. E. Stanley, *Scaling properties of driven interfaces in disordered media*, Phys. Rev. E **52**, 4 (1995).
- [44] S. Galluccio and Y.-C. Zhang, *Driven interfaces in quenched disorder at critical depinning*, Phys. Rev. E **51**, 1686 (1995).
- [45] S. Stepanow, *Dynamics of growing interfaces in disordered medium: The effect of lateral growth*, J. Phys. II France **5**, 11 (1995).
- [46] H. Leschhorn, *Anisotropic interface depinning: Numerical results*, Phys. Rev. E **54**, 1313 (1996).
- [47] L.-H. Tang, M. Kardar, and D. Dharg, *Driven depinning in anisotropic media*, Phys. Rev. Lett. **74**, 920 (1995).

- [48] H. Jeong, B. Kahng, and D. Kim, *Anisotropic surface growth model in disordered media*, Phys. Rev. Lett. **77**, 5094 (1996).
- [49] H. Jeong, B. Kahng, and D. Kim, *Facet formation in the negative quenched Kardar-Parisi-Zhang equation*, Phys. Rev. E **59**, 1570 (1999).
- [50] S. Atis, A. K. Dubey, D. Salin, L. Talon, P. Le Doussal, and K. J. Wiese, *Experimental evidence for three universality classes for reaction fronts in disordered flows*, Phys. Rev. Lett. **114**, 234502 (2015).
- [51] J. Krug, *Origins of scale invariance in growth processes*, Adv. Phys. **46**, 139 (1997).
- [52] M. A. C. Huergo, M. A. Pasquale, P. H. González, A. E. Bolzán, and A. J. Arvia, *Growth dynamics of cancer cell colonies and their comparison with noncancerous cells*, Phys. Rev. E **85**, 11918 (2012).
- [53] J. Zhang, Y. C. Zhang, P. Alstrøm, and M. T. Levinsen, *Modeling forest fire by a paper-burning experiment, a realization of the interface growth mechanism*, Physica A **189**, 383 (1992).
- [54] M. Myllys, J. Maunuksela, M. Alava, T. Ala-Nissila, J. Merikoski, and J. Timonen, *Kinetic roughening in slow combustion of paper*, Phys. Rev. E **64**, 12 (2001).
- [55] P. A. Orrillo, S. N. Santalla, R. Cuerno, L. Vázquez, S. B. Ribotta, L. M. Gassa, F. J. Mompean, R. C. Salvarezza, and M. E. Vela, *Morphological stabilization and KPZ scaling by electrochemically induced co-deposition of nanostructured NiW alloy films*, Sci. Rep. **7**, 17997 (2017).
- [56] S. Vézian, F. Natali, F. Semond, and J. Massies, *From spiral growth to kinetic roughening in molecular-beam epitaxy of GaN(0001)*, Phys. Rev. B **69**, 125329 (2004).
- [57] R. A. L. Almeida, S. O. Ferreira, T. J. Oliveira, and F. D. A. A. Reis, *Universal fluctuations in the growth of semiconductor thin films*, Phys. Rev. B **89**, 045309 (2014).

- [58] S. R. Broadbent and J. M. Hammersley, *Percolation processes: I. Crystals and mazes*, Math. Proc. Camb. Philos. Soc. **53**, 629–641 (1957).
- [59] M. Sahimi, *Applications Of Percolation Theory* (CRC Press, London, 1994).
- [60] H. Hinrichsen, *Non-equilibrium critical phenomena and phase transitions into absorbing states*, Adv. Phys. **49**, 815 (2000).
- [61] M. Henkel, H. Hinrichsen, and S. Lübeck, *Non-equilibrium phase transitions. Vol. 1: Absorbing phase transitions* (Springer Science + Business Media B.V., Dordrecht, 2008).
- [62] G. Ódor, *Universality classes in nonequilibrium lattice systems*, Rev. Mod. Phys. **76**, 663 (2004).
- [63] I. Jensen, *Low-density series expansions for directed percolation: III. Some two-dimensional lattices*, J. Phys. A: Math. Gen. **37**, 6899 (2004).
- [64] H. K. Janssen, *On the nonequilibrium phase transition in reaction-diffusion systems with an absorbing stationary state*, Z. Phys. B **42**, 151 (1981).
- [65] P. Grassberger, *On phase transitions in Schlögl's second model*, Z. Phys. B **47**, 365 (1982).
- [66] M. A. Muñoz, G. Grinstein, R. Dickman, and R. Livi, *Critical behavior of systems with many absorbing states*, Phys. Rev. Lett. **76**, 451 (1996).
- [67] M. A. Muñoz, G. Grinstein, and R. Dickman, *Phase structure of systems with infinite numbers of absorbing states*, J. Stat. Phys. **91**, 541 (1998).
- [68] I. Jensen, *Low-density series expansions for directed percolation on square and triangular lattices*, J. Phys. A: Math. Gen. **29**, 7013 (1996).
- [69] I. Jensen, *Low-density series expansions for directed percolation: I. A new efficient algorithm with applications to the square lattice*, J. Phys. A: Math. Gen. **32**, 5233 (1999).

- [70] P. Grassberger and Yi-Cheng Zhang, “*Self-organized*” formulation of standard percolation phenomena, *Physica A* **224**, 169 (1996).
- [71] C. A. Voigt and R. M. Ziff, *Epidemic analysis of the second-order transition in the Ziff-Gulari-Barshad surface-reaction model*, *Phys. Rev. E* **56**, R6241 (1997).
- [72] I. Jensen, *Critical behavior of the three-dimensional contact process*, *Phys. Rev. A* **45**, R563 (1992).
- [73] T. E. Harris, *Contact interactions on a lattice*, *Ann. Probab.* **2**, 969 (1974).
- [74] T. M. Liggett, *Interacting Particle Systems* (Springer-Verlag, New York, 1985).
- [75] T. B. dos Santos, C. I. Sampaio Filho, N. A. Araújo, C. L. Oliveira, and A. A. Moreira, *Crossover from mean-field to 2d Directed Percolation in the contact process*, *Physica A* **512**, 352 (2018).
- [76] M. M. de Oliveira and R. Dickman, *How to simulate the quasistationary state*, *Phys. Rev. E* **71**, 016129 (2005).
- [77] R. Dickman, *Reweighting in nonequilibrium simulations*, *Phys. Rev. E* **60**, R2441 (1999).
- [78] S. Lübeck and R. D. Willmann, *Universal scaling behavior of directed percolation around the upper critical dimension*, *J. Stat. Phys.* **115**, 1231 (2004).
- [79] W. Kinzel, *Directed Percolation*, in *Percolation Structures and Processes*, edited by G. Deutscher, R. Zallen, and J. Adler (A. Hilger, Bristol, 1983).
- [80] A. Bunde and S. Havlin, *Fractals and Disordered Systems* (Springer Berlin, Heidelberg, 1991).
- [81] K. A. Takeuchi, M. Kuroda, H. Chaté, and M. Sano, *Directed percolation criticality in turbulent liquid crystals*, *Phys. Rev. Lett.* **99**, 234503 (2007).

- [82] P. Rupp, R. Richter, and I. Rehberg, *Critical exponents of directed percolation measured in spatiotemporal intermittency*, Phys. Rev. E **67**, 036209 (2003).
- [83] K. A. Takeuchi, M. Kuroda, H. Chaté, and M. Sano, *Experimental realization of directed percolation criticality in turbulent liquid crystals*, Phys. Rev. E **80**, 051116 (2009).
- [84] G. Lemoult, L. Shi, K. Avila, S. V. Jalikop, M. Avila, and B. Hof, *Directed percolation phase transition to sustained turbulence in Couette flow*, Nat. Phys. **12**, 254 (2016).
- [85] S. G. Alves, T. J. Oliveira, and S. C. Ferreira, *Universal fluctuations in radial growth models belonging to the KPZ universality class*, EPL **96**, 48003 (2011).
- [86] T. J. Oliveira, S. C. Ferreira, and S. G. Alves, *Universal fluctuations in Kardar-Parisi-Zhang growth on one-dimensional flat substrates*, Phys. Rev. E **85**, 040102(R) (2012).
- [87] M. Nicoli, R. Cuerno, and M. Castro, *Dimensional fragility of the Kardar-Parisi-Zhang universality class*, J. Stat. Mech. **2013**, P11001 (2013).
- [88] J. M. López, M. A. Rodríguez, and R. Cuerno, *Superroughening versus intrinsic anomalous scaling of surfaces*, Phys. Rev. E **56**, 3993 (1997).
- [89] J. J. Ramasco, J. M. Lopez, and M. A. Rodriguez, *Generic dynamic scaling in kinetic roughening*, Phys. Rev. Lett. **84**, 2199 (2000).
- [90] R. Cuerno and L. Vázquez, *Universality issues in surface kinetic roughening of thin solid films*, in *Advances in Condensed Matter and Statistical Physics*, edited by E. Korutcheva and R. Cuerno (Nova Science Publishers, New York, 2004).
- [91] J. M. López, M. A. Rodríguez, and R. Cuerno, *Power spectrum scaling in anomalous kinetic roughening of surfaces*, Physica A **246**, 329 (1997).
- [92] D. Yllanes, *Rugged Free-Energy Landscapes in Disordered Spin Systems*, Ph.D. thesis, Universidad Complutense de Madrid (2011).

- [93] C. Michael, *Fitting correlated data*, Phys. Rev. D **49**, 2616 (1994).
- [94] M. Lulli, G. Parisi, and A. Pelissetto, *Out-of-equilibrium finite-size method for critical behavior analyses*, Phys. Rev. E **93**, 032126 (2016).
- [95] D. Seibert, *Undesirable effects of covariance matrix techniques for error analysis*, Phys. Rev. D **49**, 6240 (1994).
- [96] P. Young, *Everything You Wanted to Know About Data Analysis and Fitting but Were Afraid to Ask* (Springer, London, 2015).
- [97] B. Efron, *The Jackknife, the Bootstrap and Other Resampling Plans* (Society for Industrial and Applied Mathematics, 1982).
- [98] E. Moro, *Internal fluctuations effects on fisher waves*, Phys. Rev. Lett. **87**, 238303 (2001).
- [99] M. Cross and H. Greenside, *Pattern Formation and Dynamics in Nonequilibrium Systems* (Cambridge University Press, Cambridge, 2009).
- [100] I. R. Epstein and J. A. Pojman, *An Introduction to Nonlinear Chemical Dynamics: Oscillations, Waves, Patterns, and Chaos* (Oxford University Press, 1998).
- [101] L. S. Tsimring, *Noise in biology*, Rep. Prog. Phys. **77**, 026601 (2014).
- [102] R. Pastor-Satorras, C. Castellano, P. Van Mieghem, and A. Vespignani, *Epidemic processes in complex networks*, Rev. Mod. Phys. **87**, 925 (2015).
- [103] G. Boffetta and A. Mazzino, *Incompressible Rayleigh–Taylor Turbulence*, Annu. Rev. Fluid Mech. **49**, 119 (2017).
- [104] R. A. Fisher, *The wave of advance of advantageous genes*, Ann. Eugenics **7**, 355 (1937).
- [105] A. Kolmogorov, I. Petrosvsky, and N. Piscounov, *A study of the diffusion equation with increase in the amount of substance, and its application to a biological problem*, Bull. Moscow Univ. Math. Mech. **1**, 1 (1937).

-
- [106] J. D. Murray, *Mathematical Biology: I. An Introduction* (Springer-Verlag, New York, 2002).
- [107] W. van Saarloos, *Front propagation into unstable states*, Phys. Rep. **386**, 29 (2003).
- [108] A. S. Zadorin, Y. Rondelez, J.-C. Galas, and A. Estevez-Torres, *Synthesis of programmable reaction-diffusion fronts using DNA catalyzers*, Phys. Rev. Lett. **114**, 068301 (2015).
- [109] H. Tanaka, Z. Zeravcic, and M. P. Brenner, *Mutation at expanding front of self-replicating colloidal clusters*, Phys. Rev. Lett. **117**, 238004 (2016).
- [110] A. S. Zadorin, Y. Rondelez, G. Gines, V. Dilhas, G. Urtel, A. Zambrano, J. C. Galas, and A. Estevez-Torres, *Synthesis and materialization of a reaction-diffusion French flag pattern*, Nature Chem. **9**, 990 (2017).
- [111] G. Q. Sun, M. Jusup, Z. Jin, Y. Wang, and Z. Wang, *Pattern transitions in spatial epidemics: Mechanisms and emergent properties*, Phys. Life Rev. **19**, 43 (2016).
- [112] C. Hui and D. M. Richardson, *Invasion dynamics* (Oxford University Press, Oxford, 2017).
- [113] F. Sagués, J. M. Sancho, and J. García-Ojalvo, *Spatiotemporal order out of noise*, Rev. Mod. Phys. **79**, 829 (2007).
- [114] O. Hallatschek, *The noisy edge of traveling waves*, Proc. Natl. Acad. Sci. USA **108**, 1783 (2011).
- [115] S. Nestic, R. Cuerno, and E. Moro, *Macroscopic response to microscopic intrinsic noise in three-dimensional fisher fronts*, Phys. Rev. Lett. **113**, 180602 (2014).
- [116] D. Panja, *Effects of fluctuations on propagating fronts*, Phys. Rep. **393**, 87 (2004).

- [117] D. Ben-Avraham, M. A. Burschka, and C. R. Doering, *Statics and dynamics of a diffusion-limited reaction: Anomalous kinetics, nonequilibrium self-ordering, and a dynamic transition*, J. Stat. Phys. **60**, 695 (1990).
- [118] L. Pechenik and H. Levine, *Interfacial velocity corrections due to multiplicative noise*, Phys. Rev. E **59**, 3893 (1999).
- [119] C. R. Doering, C. Mueller, and P. Smereka, *Interacting particles, the stochastic Fisher-Kolmogorov-Petrovsky-Piscounov equation, and duality*, Physica A **325**, 243 (2003).
- [120] E. Moro, *Numerical schemes for continuum models of reaction-diffusion systems subject to internal noise*, Phys. Rev. E **70**, 045102(R) (2004).
- [121] J. Riordan, C. R. Doering, and D. Ben-Avraham, *Fluctuations and stability of fisher waves*, Phys. Rev. Lett. **75**, 565 (1995).
- [122] G. Tripathy and W. Van Saarloos, *Fluctuation and relaxation properties of pulled fronts: a scenario for nonstandard Kardar-Parisi-Zhang scaling*, Phys. Rev. Lett. **85**, 3556 (2000).
- [123] G. Tripathy, A. Rocco, J. Casademunt, and W. van Saarloos, *Universality Class of Fluctuating Pulled Fronts*, Phys. Rev. Lett. **86**, 5215 (2001).
- [124] E. Moro, *Hybrid method for simulating front propagation in reaction-diffusion systems*, Phys. Rev. E **69**, 060101(R) (2004).
- [125] P. Córdoba-Torres, S. N. Santalla, R. Cuerno, and J. Rodríguez-Laguna, *Kardar-Parisi-Zhang universality in first-passage percolation: the role of geodesic degeneracy*, J. Stat. Mech. **2018**, 063212 (2018).
- [126] Y. Saito, M. Dufay, and O. Pierre-Louis, *Nonequilibrium cluster diffusion during growth and evaporation in two dimensions*, Phys. Rev. Lett. **108**, 8522 (2012).
- [127] D. Scalise and R. Schulman, *Controlling matter at the molecular scale with DNA circuits*, Ann. Rev. Biomed. Eng. **21**, 469 (2019).

- [128] J. Zenk, D. Scalise, K. Wang, P. Dorsey, J. Fern, A. Cruz, and R. Schulman, *Stable DNA-based reaction-diffusion patterns*, RSC Adv. **7**, 18032 (2017).
- [129] M. Lovrak, W. E. Hendriksen, M. T. Kreutzer, V. Van Steijn, R. Eelkema, and J. H. Van Esch, *Control over the formation of supramolecular material objects using reaction-diffusion*, Soft Matter **15**, 4276 (2019).
- [130] T. Chou, K. Mallick, and R. K. P. Zia, *Non-equilibrium statistical mechanics: from a paradigmatic model to biological transport*, Rep. Prog. Phys. **74**, 116601 (2011).
- [131] F. Bornemann, *On the numerical evaluation of distributions in random matrix theory: A review*, Markov Process. Relat. Fields **16**, 803 (2010).
- [132] I. S. S. Carrasco and T. J. Oliveira, *Universality and geometry dependence in the class of the nonlinear molecular beam epitaxy equation*, Phys. Rev. E **94**, 050801(R) (2016).
- [133] E. Rodríguez-Fernández and R. Cuerno, *Gaussian statistics as an emergent symmetry of the stochastic scalar Burgers equation*, Phys. Rev. E **99**, 042108 (2019).
- [134] P. Laden, ed., *Chemistry and Technology of Water Based Inks* (Blackie Academic and Professional, London, 1997).
- [135] R. D. Deegan, O. Bakajin, T. F. Dupont, G. Huber, S. R. Nagel, and T. A. Witten, *Capillary flow as the cause of ring stains from dried liquid drops*, Nature **389**, 827 (1997).
- [136] R. D. Deegan, O. Bakajin, T. F. Dupont, G. Huber, S. R. Nagel, and T. A. Witten, *Contact line deposits in an evaporating drop*, Phys. Rev. E **62**, 756 (2000).
- [137] P. J. Yunker, T. Still, M. A. Lohr, and A. G. Yodh, *Suppression of the coffee-ring effect by shape-dependent capillary interactions*, Nature **476**, 308 (2011).

- [138] J. C. Loudet, A. M. Alsayer, J. Zhang, and A. G. Yodh, *Capillary interactions between anisotropic colloidal particles*, Phys. Rev. Lett. **94**, 018301 (2005).
- [139] B. J. Park and E. M. Furst, *Attractive interactions between colloids at the oil–water interface*, Soft Matter **7**, 7676 (2011).
- [140] P. J. Yunker, M. A. Lohr, T. Still, A. Borodin, D. J. Durian, and A. G. Yodh, *Effects of particle shape on growth dynamics at edges of evaporating drops of colloidal suspensions*, Phys. Rev. Lett. **110**, 035501 (2013).
- [141] P. J. Yunker, M. A. Lohr, T. Still, A. Borodin, D. J. Durian, and A. G. Yodh, *Yunker et al. Reply*, Phys. Rev. Lett. **111**, 209602 (2013).
- [142] R. K. Merton, *The Matthew effect in Science: The reward and communication systems of science are considered*, Science **159**, 55 (1968).
- [143] T. J. Oliveira and F. D. A. Aarão Reis, *Simulating the initial growth of a deposit from colloidal suspensions*, J. Stat. Mech. **2014**, P09006 (2014).
- [144] D. Rodríguez-Pérez, J. L. Castillo, and J. Carlos Antoranz, *Relationship between particle deposit characteristics and the mechanism of particle arrival*, Phys. Rev. E **72**, 021403 (2005).
- [145] C. S. Dias, N. A. M. Araújo, and M. M. Telo Da Gama, *Nonequilibrium growth of patchy-colloid networks on substrates*, Phys. Rev. E **87**, 032308 (2013).
- [146] C. S. Dias, N. A. Araújo, and M. M. Telo Da Gama, *Kinetic roughening of aggregates of patchy colloids with strong and weak bonds*, EPL **107**, 56002 (2014).
- [147] C. S. Dias, P. J. Yunker, A. G. Yodh, N. A. Araújo, and M. M. Telo Da Gama, *Interaction anisotropy and the KPZ to KPZQ transition in particle deposition at the edges of drying drops*, Soft Matter **14**, 1903 (2018).
- [148] V. Orozco-Gómez and R. Cuerno, *Depinning Transition Phenomena in Evaporating Drops of Colloidal Suspensions*, Master thesis, Universidad Carlos III de Madrid (2019).

-
- [149] P. Meakin, *Fractals, Scaling and Growth Far from Equilibrium* (Cambridge University Press, Cambridge, 1998).
- [150] J. Krug and P. Meakin, *Microstructure and surface scaling in ballistic deposition at oblique incidence*, Phys. Rev. A **40**, 2064 (1989).
- [151] J. Asikainen, S. Majaniemi, M. Dubé, J. Heinonen, and T. Ala-Nissila, *Dynamical scaling and kinetic roughening of single valued fronts propagating in fractal media*, Eur. Phys. J. B **30**, 253 (2002).
- [152] G. S. Bales, R. Bruinsma, E. a. Eklund, R. P. Karunasiri, J. Rudnick, and A. Zangwill, *Growth and erosion of thin solid films*, Science **249**, 264 (1990).
- [153] J. Asikainen, S. Majaniemi, M. Dubé, and T. Ala-Nissila, *Interface dynamics and kinetic roughening in fractals*, Phys. Rev. E **65**, 052104 (2002).
- [154] M. Nicoli, M. Castro, and R. Cuerno, *Kinetic roughening in a realistic model of non-conserved interface growth*, J. Stat. Mech. **2009**, P02036 (2009).
- [155] S. N. Santalla, J. Rodríguez-Laguna, J. P. Abad, I. Marín, M. d. M. Espinosa, J. Muñoz-García, L. Vázquez, and R. Cuerno, *Non-universality of front fluctuations for compact colonies of non-motile bacteria*, Phys. Rev. E **98**, 012407 (2018).
- [156] R. Cuerno and M. Castro, *Transients due to instabilities hinder Kardar-Parisi-Zhang scaling: A Unified Derivation for Surface growth by electrochemical and chemical vapor deposition*, Phys. Rev. Lett. **87**, 236103 (2001).
- [157] R. Dickman and M. A. Muñoz, *Interface scaling in the contact process*, Phys. Rev. E **62**, 7632 (2000).
- [158] E. Rodriguez-Fernandez, S. N. Santalla, M. Castro, and R. Cuerno, *Anomalous ballistic scaling in the tensionless or inviscid Kardar-Parisi-Zhang equation*, Phys. Rev. E **106**, 024802 (2022).

- [159] J. M. Marcos, P. Rodríguez-López, J. J. Meléndez, R. Cuerno, and J. J. Ruiz-Lorenzo, *Spreading fronts of wetting liquid droplets: Microscopic simulations and universal fluctuations*, Phys. Rev. E **105**, 1 (2022).
- [160] J. López, M. Castro, and R. Gallego, *Scaling of local slopes, conservation laws, and anomalous roughening in surface growth*, Phys. Rev. Lett. **94**, 166103 (2005).
- [161] I. G. Szendro, J. M. López, and M. A. Rodríguez, *Localization in disordered media, anomalous roughening, and coarsening dynamics of faceted surfaces*, Phys. Rev. E **76**, 011603 (2007).
- [162] T. Song and H. Xia, *Kinetic roughening and nontrivial scaling in the Kardar-Parisi-Zhang growth with long-range temporal correlations*, J. Stat. Mech. **2021**, 073203 (2021).
- [163] M. Siegert, *Determining exponents in models of kinetic surface roughening*, Phys. Rev. E **53**, 3209 (1996).
- [164] M. Schroeder and M. Siegert, *Scaling of growing surfaces with large local slopes*, EPL **24**, 563 (1993).
- [165] J. M. López, *Scaling Approach to Calculate Critical Exponents in Anomalous Surface Roughening*, Phys. Rev. Lett. **83**, 4594 (1999).
- [166] B. G. Barreales, J. J. Meléndez, R. Cuerno, and J. J. Ruiz-Lorenzo, *PDF of rescaled front fluctuations in Contact Process (DATASET)*, 10.5281/zenodo.7794480 (2023).
- [167] S. G. Alves, T. J. Oliveira, and S. C. Ferreira, *Universality of fluctuations in the Kardar-Parisi-Zhang class in high dimensions and its upper critical dimension*, Phys. Rev. E **90**, 020103(R) (2014).
- [168] C. Monthus and T. Garel, *Disorder-dominated phases of random systems: relations between the tail exponents and scaling exponents*, J. Stat. Mech. **2008**, P01008 (2008).
- [169] S. N. Majumdar and G. Schehr, *Top eigenvalue of a random matrix: large deviations and third order phase transition*, J. Stat. Mech. **2014**, P01012 (2014).

-
- [170] J. M. Kim, M. A. Moore, and A. J. Bray, *Zero-temperature directed polymers in a random potential*, Phys. Rev. A **44**, 2345 (1991).
- [171] B. G. Barreales, J. J. Meléndez, R. Cuerno, and J. J. Ruiz-Lorenzo, *Height covariance correlation function in Contact Process (DATASET)*, 10.5281/zenodo.7788436 (2023).
- [172] B. G. Barreales, J. J. Meléndez, R. Cuerno, and J. J. Ruiz-Lorenzo, *Kardar-Parisi-Zhang universality class for the critical dynamics of reaction-diffusion fronts*, J. Stat. Mech. **2020**, 023203 (2020).
- [173] H. S. Song and J. M. Kim, *Depinning transition of the quenched Mullins-Herring equation*, J. Korean Phys. Soc. **49**, 1520 (2006).
- [174] H. S. Song and J. M. Kim, *Height-difference correlation function of the quenched Mullins-herring equation*, J. Korean Phys. Soc. **52**, 166 (2008).
- [175] H. S. Song and J. M. Kim, *A discrete interface growth model for quenched impurities in $d = 2 + 1$ dimensions*, J. Stat. Mech. , P09021 (2011).
- [176] A. Pikovsky, M. Rosenblum, and J. Kurths, *Synchronization: A Universal Concept in Nonlinear Sciences* (Cambridge University Press, Cambridge, 2001).
- [177] A. Arenas, A. Díaz-Guilera, J. Kurths, Y. Moreno, and C. Zhou, *Synchronization in complex networks*, Phys. Rep. **469**, 93 (2008).
- [178] A. Pimpinelli and J. Villain, *Physics of Crystal Growth* (Cambridge University Press, Cambridge, 1998).